2018

# Fluorescence imaging for nanoscale clustering and lateral diffusion of receptor for advanced glycation endproducts

Qiaochu Zhu
*Iowa State University*

# Fluorescence imaging for nanoscale clustering and lateral diffusion of receptor for advanced glycation endproducts

by

**Qiaochu Zhu**

A dissertation submitted to the graduate faculty

in partial fulfillment of the requirements for the degree of

DOCTOR OF PHILOSOPHY

Major: Analytical Chemistry

Program of Study Committee:
Emily A. Smith, Major Professor
Robert S. Houk
Young-Jin Lee
Jacob W. Petrich
Javier Vela-Becerra

The student author, whose presentation of the scholarship herein was approved by the program of study committee, is solely responsible for the content of this dissertation. The Graduate College will ensure this dissertation is globally accessible and will not permit alterations after a degree is conferred.

Iowa State University

Ames, Iowa

2018

**DEDICATION**

*This dissertation is dedicated to my family*

## TABLE OF CONTENTS

Page

## ACKNOWLEDGMENTS

I would like to express my sincere gratitude to my major professor, Prof. Emily Smith, for her guidance and support of my academic and personal life, for her creativity and immense knowledge of my research, and for her instruction and patience of writing of papers and this dissertation.

In addition, I would like to thank my POS committee membranes, Prof. Robert S. Houk, Prof. Young-Jin Lee, Prof. Jacob Petrich, and Prof. Javier Vela-Becerra, for their insightful advice and comments during my doctoral studies. I also want to thank my collaborators Prof. Jacob Petrich and Prof. Javier Vela-Becerra for providing an opportunity to work on inorganic materials. I thank all Smith group members, Aleem, Avinash, Brett, Chamari, Charles, Daniel, Deyny, Ginger, Nicole, Sadie, for all your kindness and help. Special thanks to Dr. Aleem Syed and Charles Nyamekye for working together on research projects. I would like to especially thank my friends, Long, Jingzhe, and Zhiyuan for making my life fun and enjoyable. Special thanks to Chen for enlightening me the first glance of programming in my research and personal career. In particular, I am grateful to Lin for sharing our wonderful journey and providing unending inspiration.

Finally, I would like to thank my parents, my aunt and my grandparents, whose love and support are with me in whatever I pursue.

## ABSTRACT

Receptors on the cell membrane initiate cell signaling upon stimulation with extracellular molecules; this results in signal transduction pathways. Receptors are redistributed as clusters upon extracellular stimuli with the change of receptor dynamics. The lateral diffusion of receptors plays a role in how receptors interface with other membrane proteins, extracellular ligands, intracellular proteins, and how receptors function. In this dissertation, the lateral diffusion and clusters of receptors for advanced glycation end-products (RAGE) at both a single molecule and the ensemble level are discussed. The effects of extracellular ligands, cholesterol levels, and actin polymerization on RAGE diffusion are considered.

RAGE is a member of the immunoglobulin superfamily of membrane proteins that are involved in numerous pathological conditions. Ligand binding to the extracellular domain of RAGE drives RAGE clusters and initiates the downstream signal transduction. The signal transduction also consists of the interaction between diaphanous-1 (Diaph1) with the cytoplasmic tail of RAGE. Diaph1 affects the nanoscale clustering and diffusion of RAGE as measured by super-resolution stochastic optical reconstruction microscopy (STORM) and single particle tracking (SPT). A reduced expression level of Diaph1 or a disrupted interaction between Diaph1 and RAGE results in a decreased size and number of RAGE clusters. RAGE diffusion is increased after reduced Diaph1 expression. In contrast, when the interaction site between RAGE and Diaph1 is mutated, RAGE diffusion is slowed.

The effect of the ligand on the lateral diffusion of the receptor for advanced glycation endproducts involved in numerous pathological conditions. A methylglyoxal-

modified bovine serum albumin (MGO-BSA) RAGE ligand is prepared and characterized. The effect of MGO-BSA on the lateral diffusion of RAGE is measured by SPT. Ligand incubation affects RAGE diffusion and the phosphorylation of extracellular signal-regulated kinases. However, there is no correlation between MGO-BSA ligand binding affinity and the change in RAGE diffusion. Moreover, the mechanism for the ligand-induced change in RAGE diffusion is dependent on cholesterol.

The actin cytoskeleton plays a crucial role in RAGE functions. The effect of the actin cytoskeleton on RAGE diffusion is measured by fluorescence recovery after photobleaching at the ensemble-level. When depolymerization of the actin cytoskeleton is inhibited, RAGE diffusion and mobile fraction are decreased. Also, when the actin cytoskeleton is disrupted, the phosphorylation of extracellular signal-regulated kinase is reduced.

# CHAPTER 1. GENERAL INTRODUCTION

## 1.1 Receptor Proteins Dynamics and Clustering

Albert Einstein said: "*Life is like riding a bicycle. To keep your balance, you must keep moving*". With his "*keep moving*" contribution improving the reality of small particles and their motions in 1905, the extensive studies about dynamics have emerged in both macroscopic and microscopic environment. A fluid mosaic model was proposed by S. Jonathan Singer and Garth Nicolson in 1972 to describe the general structure of a biological membrane wherein the protein can diffuse freely [1]. A receptor acts as a doorbell on the cell membrane; it provides a route for communication between the outside and inside of the cell. This process is called signal transduction. Each receptor is involved in a specific set of signal transduction events. This signal transduction set off by one particular receptor-ligand binding event, which can initiate one or several signal pathways [2-5]. Defects in signaling pathways are implicated in a large number of diseases such as cancer [6], cardiovascular disease [7], diabetes [8] and many forms of mental illnesses [9, 10]. For example, epidermal growth factor receptor overexpression has been found in cancer cells [11]; Toll-like receptor activation contributes to the development and progression of cardiac dysfunction in sepsis and congestive heart failure [12]; Alzheimer's disease and Down's syndrome are caused by aberrant catabolism of a cell-surface receptor [13].

Receptor dynamics and conformational changes contribute to transferring the signal into cells. Although the correlations between signal transduction and receptor dynamics vary from one receptor to another, a canonical principle is emerging. Receptors undergo oligomerization upon stimulation with extracellular ligands, which include hormones, drugs, and other proteins, that result in the activation of the protein-tyrosine kinase. Subsequently,

the phosphorylation of tyrosine residues transmits the signal to the intracellular protein, which leads to these receptors' mobilization on the cell membrane [14]. Many receptors redistribute into receptor clusters or conformation in conjunction with the change of receptor dynamic upon the ligand induction [15, 16]. In addition to extracellular stimuli interactions with other receptors may also affect membrane dynamics and clustering. The vital role of the actin cytoskeleton in controlling receptor compartmentalization, dynamics, and clustering have been reported [17]. Over the past decade, a larger number of analysis techniques have been developed to measure receptor dynamics and clustering. The imaging techniques are reviewed in Chapter 1.2.

## 1.2 Traditional Imaging Techniques for Receptor Dynamics and Clustering in Living Cells

In order to describe the entirety of receptor dynamics and organization, it is necessary to combine the kinetic state at a multidimensional spatiotemporal scale and the conformational state at a multidimensional energy landscape [18]. Researchers have worked relentlessly for many years to obtain this information using a variety of biophysical techniques, such as x-ray scattering [19], magnetic resonance spectroscopy [20, 21], mass spectrometry [22, 23], and vibrational spectroscopy [24, 25]. These analysis methods cover a broad range of spatial scale (from sub-angstroms to tens of angstroms) and time scale (from sub-picoseconds to seconds). Nowadays, computational techniques are aiding in providing the connection between structural information and dynamics. However, direct observation of protein dynamics by imaging can provide relevant information about cellular events that cannot be obtained by all the preceding methods. First, imaging can perform in living cells; receptor dynamics are measured in a relevant environment. Second, spectrally-resolved

fluorophores can identify the distinct cellular components with high specificity. Third, super-resolution fluorescence imaging can increase in the resolving power at a spatial scale. Thus, imaging receptors in living cells is a valuable tool to study dynamics and clustering. In the following sections, imaging techniques for measuring receptor dynamics and clustering are reviewed.

**Fluorescence recovery after photobleaching (FRAP)**

Fluorescence recovery after photobleaching, known as FRAP, is a matured, but also an ever-evolving, fluorescence technique for studying receptor dynamics [26-28]. The basic principle is shown in Figure 1.1. High intensity light illuminates a defined region of interest (ROI) where the protein under study is tagged with a fluorescent probe. In the bleaching step, the fluorophore within the ROI is irreversibly converted into a non-fluorescent species. Then the fluorescence intensity within the ROI recovers due to the diffusion of the surrounding non-bleached fluorescent probe. The speed and mode of recovery depend upon the diffusion of the biomolecule onto which the probe is attached. The fluorescence intensity in the ROI before and after the bleaching step is recorded by time lapse microscopy with low intensity light. The resulting time-intensity curve is used to obtain the mobile fraction and diffusion coefficient. The mobile fraction (R) is defined as:

$$R = \frac{F_\infty - F_0}{F_i - F_0} \qquad (1-1)$$

where $F_\infty$ is the fluorescence intensity in the ROI after full recovery the fluorescence, $F_i$ is the fluorescence intensity before the beaching, $F_0$ is the fluorescence intensity just after bleaching. The diffusion coefficient (D) is related to the diffusion time, $\tau_D$, and the radius of

the focused laser beam is (ω). Each fluorescence recovery curve is further fit with equation below [29].

$$F(t) = \frac{F_0 + F_\infty \left(\frac{t}{\tau}\right)^\alpha}{1 + \left(\frac{t}{\tau}\right)^\alpha} \qquad (1-2)$$

where the $\alpha$ value after fitting represents the diffusion mode. The diffusion coefficient is calculated from:

$$D = \frac{\omega^2}{4\tau^\alpha t^{\alpha-1}} \qquad (1-3)$$

There are several photobleaching techniques similar to FRAP such as fluorescence loss in photobleaching [30, 31], inverse FRAP [32, 33], fluorescence loss after photo-activation [34], and fluorescence localization after photobleaching [35]. These techniques rely on controlling light illumination on fluorescent proteins or organic dyes. Fluorescent proteins such as green, yellow, and red fluorescent protein are ideal in FRAP studies because they can be bleached without detectable damage to the cell [36]. Recently, a multi-photon FRAP technique was developed for quantitative three-dimensional diffusion measurements [37, 38]. Sandra et al. have developed a dual-color FRAP with monomeric and covalent dimeric model proteins to identify the dimerization and high-order complexation of receptor proteins [39]. FRAP not only provides information about the lateral diffusion of receptors within the membrane and dimerization or oligomerization of receptors.

**Fluorescence correlation spectroscopy (FCS)**

Fluorescence correlation spectroscopy, known as FCS, is another popular technique to measure the dynamics of molecules on the living cell [40, 41]. FCS is based on the statistical analysis of time-dependent intensity fluctuations due to molecules diffusing

through a small volume defined by a focused laser illumination and a confocal aperture [42]. The basic principle is shown in Figure 1.2. A focal volume is generated by focusing a laser to a diffraction-limited spot and confining the spatial scale with a pinhole in the emission path. The fluorescence intensity is detected by photon counting devices such as an avalanche photodiode [43]. The autocorrelation function, G($\tau$), is plotted over the lag time $\tau$. The fluorophores are confined into either two-dimensional (2D) or three-dimensional (3D) planes, and the correlation functions for freely diffusing molecules are:

$$G_{2D}(\tau) = \frac{1}{N}\left(1 + \frac{4D\tau}{S^2}\right)^{-1} \qquad (1-4)$$

$$G_{3D}(\tau) = \frac{1}{N}\left(1 + \frac{4D\tau}{S^2}\right)^{-1}\left(1 + \frac{4D\tau}{u^2}\right)^{-\frac{1}{2}} \qquad (1-5)$$

where N is the average number of fluorophores in the detected volume; the radius S and half-length u refer to distances at which the detection profile decreases to $e^{-2}$ of its maximal intensity value; D is the diffusion coefficient. Recently, a high-throughput FCS was reported that reduces the manual, labor-intensive workflow of image optimization, the image acquisition, and the correlation analysis [44]. Due to the extreme sensitivity of FCS measurement, the magnitude of the diffusional autocorrelation function can measure the change of molecular size to large fluorescence spikes and its temporal decay. Tjernberg et al. has demonstrated that the formation of amyloid β-protein oligomers precedes the formation of fibrils via FCS [45].

FCS and FRAP are commonly used to measure the diffusion of receptors tagged with fluorophores in live cells, and provide similar and often complementary information. Traditional FCS methods monitor the intensity fluctuations in a small confocal volume and has the benefit of being extremely sensitive to the mobile fluorophores but are not able to

detect the immobile ones. On the other hand, FRAP can measure the immobile fraction of fluorescent molecules [46]. The motion of receptors on the cell membrane is not synchronized across the measured region, and the cell membrane is heterogeneous; it is essential to measure diffusion one receptor at a time to capture the diffusion heterogeneity. Although FRAP and FCS provide millisecond temporal resolutions, the spatial resolutions are still not well improved in FRAP and FCS. In Chapter 1.3, the imaging techniques for measuring the receptor dynamics and clustering at the single-protein level and super-resolution imaging are reviewed.

## 1.3 Single-molecule Imaging Techniques for Receptor Dynamics and Clustering in Living Cells

Single-molecule imaging has been extensively used to study fundamental protein dynamics [47-50]. Single molecule imaging can provide complementary information with FCS and FRAP on the diffusion properties of receptors in cell membranes [50]. With modern super-resolution advances, single molecule imaging can achieve tens of microseconds temporal resolution with down to 1-nm spatial resolution to monitor receptor dynamics and membrane organization [51].

**Traditional single particle tracking**

Single particle tracking (SPT) plays a dominant role in many of the advances in single-molecule imaging. The proteins of interest are tagged with fluorescent probes such as organic dyes [52], fluorescent proteins [53, 54] and quantum dots [55, 56]. Quantum dots (Qds) are desirable fluorophores for measuring receptor dynamics because of their high quantum efficiency and brightness, which correlate with short acquisition times that lead to the fast temporal resolution. The stability of Qds also provides the capability of long analysis

durations. Several receptor labeling methods have been reported for SPT measurements. The receptors are labeled using either its ligand or antibody [57], which are conjugated with fluorophores, or by inserting genes encoding labeling tags such as His-tag [58], Flag-tag [59], or Snap-tag [60]. Specific binding is measured to evaluate the efficiency of the labeling method.

After specific labelling has been achieved, the SPT experiments are performed with high speed cameras as shown in Figure 1.3. A series of frames showing Qds-labeled protein are acquired over time. There are several data analysis options available. For example, a 2D/3D single-particle tracking plug-in (MosaicSuite) for ImageJ can be used to localize and track single particles in each frame over time to generate trajectories of x-y location [61]. The achieved localization uncertainty may be as low as a few nanometers and depends on the signal-to-noise ratio. The algorithm used for the SPT experiments described in this thesis is based on the cumulative probability distribution (CPD). CPD is defined as the probability that a particle remains within a circle with a radius r. This algorithm has been extensively used to quantify the diffusion coefficient and fractional populations in multiple systems [62-65]. The extracted trajectories are subsequently analyzed using TrackArt, which is a MATLAB application based on a previously described algorithm [66, 67]. When the CPD reveals there are two or more diffusing populations, the fraction (f) of each population can be separately estimated. A single population exhibiting Brownian motion yields a single exponential model (1p model) and can be fit by:

$$CPD(r^2, t) = 1 - \exp\left(-\frac{r^2}{4Dt}\right) \qquad (1-6)$$

where D is the diffusion coefficient. The goodness-of-fit is determined by calculating the residual sum of squares. If a single exponential model fails to accurately fit the data, then a

double exponential model (2p model) is used:

$$CPD(r^2,t) = 1 - \langle f \exp\left(-\frac{r^2}{4D_f t}\right) + (1-f)\exp\left(-\frac{r^2}{4D_s t}\right)\rangle \qquad (1-7)$$

The 2p model produces two diffusion coefficients: $D_f$ for the fast population and $D_s$ for the slow population. The results also provide the relative fractions f and 1 – f for the fast population and slow population, respectively [68]. An algorithm developed by Simson and Menchon [69, 70] was used to detect confined motion within each trajectory. Confined motion is defined as a diffusive motion that is restricted by boundaries that cannot be crossed [71]. The trajectory is analyzed over a specific timeframe and the probability (ψ) of a protein diffusing by Brownian motion in the selected time frame is given by

$$log(\psi) = 0.2048 - 2.5117 \times \frac{D_t}{R^2} \qquad (1-8)$$

where $D_t$ is the diffusion coefficient, R is the radius of given region. The probability (ψ) is then defined as a confinement index (L) by a relation

$$L = \begin{cases} -\log(\psi) - 1 & \psi \leq 0.1 \\ 0 & \psi > 0.1 \end{cases} \qquad (1-9)$$

The confinement index is able to identify the confined domains in the given trajectory. The critical confinement index and critical confinement time are obtained from simulated Brownian trajectories for a range of diffusion coefficients as previously described [58]. If a trajectory exhibits confined motion, the diffusion coefficient inside confined domains, the size of the confined domain, and the time in the confined domain are calculated.

**Super-resolution imaging**

In 2014, the Noble Prize in Chemistry was awarded to three individuals, *Eric Betzig, Stefan W. Hell and William E. Moerner,* who led the super-resolution revolution by breaking the diffraction limitation in optical imaging [72]. Super-resolution microscopy techniques are

separated into two categories. The first category aims to improve optics and the laser module with image processing algorithms and can include the following techniques: structured illumination microscopy [73], stimulated emission depletion microscopy (STED) [74], and STED derivatives (reversible saturable or switchable optical fluorescence transitions [75, 76], and ground state depletion [77]). The second category aims to break the diffraction limit of light with stochastic function techniques that control single molecule on-off switching and some examples include the following techniques: stochastic optical fluctuation imaging [78], stochastic optical reconstruction microscopy (STORM) [79, 80], and photoactivated localization microscopy [81-83]. In this dissertation, the results of STORM experiments are reported to measure receptor nanoscale organization.

STORM has been developed as a high-resolution fluorescence microscopy method achieved by transferring the number of fluorophores to a reversible dark state and then by stochastically activating some certain number of individual fluorophores [84, 85]. The basic principle of STORM is shown in Figure 1.4. Photoswitchable fluorophores are used for labeling the biomolecule of interest. The fluorophores are switched off upon illumination with the appropriate wavelength and intensity of light. Then, a certain number of fluorophores are re-activated using another laser wavelength. Usually, 0.1-1.0 fluorophores are simultaneously activated per $\mu m^2$ in order to obtain conditions are suitable for precise localization of every fluorophore. Repetitive activation, localization and deactivation lead to resolved nanoscale structures in the reconstructed image. The photoswitchable dyes are a key element in STORM experiments. Traditionally, organic dyes (such as Alexa Fluor or ATTO) require a reducing agent with thiol groups to selectively quench the triplet state [86]. A reversible photoswitching process is described as followed. Firstly, fluorophores are excited

to a singlet excited state; the excited energy is released to a triplet state; the triplet state energy is reduced by thiolate to form radical anions, which are further reoxidized by oxygen or through thermal relaxation. These radical anions exhibit a lifetime of several hundred milliseconds, which leads to dark events. Recently, our group developed a versatile probe by attached paclitaxel to the photoactivatable BODIPY for imaging of microtubules [87].

Receptors have been reported to form clusters during signal transduction based on STORM measurements. For example, Jin et al. have demonstrated that clusters of epidermal growth factor receptor measured by STORM exhibit a moderate clustering state with a homogeneous distribution on the cell surface of COS-7 cells [88]. Ying et al. have proved the multiscale reorganization of T-cell receptors in the immune response by STORM [89]. Sarah et al. have discovered two distinct stages of immunoglobulin E receptor clustering in response to antigen binding [90]. InChapter 2, STORM data is reported to measure the clustering of a receptor for advanced glycation endproducts.

### 1.4 Receptor for Advanced Glycation Endproducts

The receptor for advanced glycation endproducts (RAGE) is a member of the immunoglobulin superfamily of membrane proteins. It was initially found to be an advanced glycation endproducts (AGE)-binding protein [91]. RAGE, as shown in Figure 1.5, contains three extracellular immunoglobulin-like domains, a single transmembrane helix domain and a cytosolic domain as a tail. The extracellular domain is composed of a V-type and two C-type domains (C1 and C2). A tandem V-type and C1-type structure (VC1) contributes to ligand binding [92]. The short cytosolic tail plays an essential role in signal transduction [93]. Many studies indicated that RAGE was thought to be related to a series of chronic disease

such as cancer, neurodegeneration, Alzheimer's, inflammatory response, atherosclerosis and diabetes [94-98].

RAGE, as a pattern recognition receptor, is now prominently characterized as a multi-ligand receptor that interacts with ligands in addition to advanced glycation endproducts including: S100/calgranulins, high mobility group protein box-1 and β-amyloid [99-105]. RAGE surface charges show that the VC1 domain displays a positively charged electrostatic pocket that attracts the negative character of diverse RAGE ligands by charge-charge interactions [106]. RAGE-ligand interactions play an important role in molecular function.

RAGE oligomerization has been studied by recent fluorescence resonance energy transfer, bis(sulfosuccinmidyl) substrate cross-link and X-ray crystallography studies [107, 108]. The results showed that RAGE forms a hexamer containing a trimer of dimers in response to the binding of various ligands [109]. Also, RAGE interacts with intracellular protein to perform signal transduction. RAGE signal transduction is a consequence of the interaction between the formin homology 1 (FH1) domain of diaphanous-1 (Diaph1) with the RAGE cytoplasmic tail [93, 110, 111]. In this dissertation, the effects of extracellular ligands, cholesterol levels, and actin polymerization on RAGE diffusion and membrane organization are measured *via* FRAP, SPT and STORM.

This dissertation is categorized into five chapters. In Chapter 1, a general introduction presents a review of the role of receptor dynamics and organization in receptor function as well as imaging techniques that can measure receptor diffusion and clusters. The work discussed in Chapter 2 describes how Diaph1 affects the nanoscale clustering and lateral diffusion of RAGE using SPT and STORM. In Chapter 3, ligand binding affinity and changes in the lateral diffusion of RAGE are described at the single receptor level using SPT.

The changes in RAGE lateral diffusion and phosphorylation of extracellular signal-regulated kinase are described in both native and actin filament altered cells using fluorescence recovery after photobleaching in Chapter 4. General conclusions and future insights are presented in Chapter 5.

## 1.5 References

[1] S.J. Singer, G.L. Nicolson, The Fluid Mosaic Model of the Structure of Cell Membranes, *Science*, 175 (1972) 720-731.

[2] A.G. Gilman, G-Proteins - Transducers of Receptor-Generated Signals, *Annu Rev Biochem*, 56 (1987) 615-649.

[3] T.M. Lincoln, T.L. Cornwell, Intracellular cyclic GMP receptor proteins, *FASEB J*, 7 (1993) 328-338.

[4] D.J. Mangelsdorf, C. Thummel, M. Beato, P. Herrlich, G. Schutz, K. Umesono, B. Blumberg, P. Kastner, M. Mark, P. Chambon, R.M. Evans, The nuclear receptor superfamily: the second decade, *Cell*, 83 (1995) 835-839.

[5] R.S. Herbst, Review of epidermal growth factor receptor biology, *Int J Radiat Oncol Biol Phys*, 59 (2004) 21-26.

[6] R. Roskoski, Jr., The ErbB/HER receptor protein-tyrosine kinases and cancer, *Biochem Biophys Res Commun*, 319 (2004) 1-11.

[7] C. Fernandez-Patron, J.G. Filep, GPCRs in cardiovascular pathologies, *Drug Discov Today Dis Mech*, 9 (2012) e75-e78.

[8] M.E. Cooper, D. Vranes, S. Youssef, S.A. Stacker, A.J. Cox, B. Rizkalla, D.J. Casley, L.A. Bach, D.J. Kelly, R.E. Gilbert, Increased renal expression of vascular endothelial growth factor (VEGF) and its receptor VEGFR-2 in experimental diabetes, *Diabetes*, 48 (1999) 2229-2239.

[9] D. Stclair, D. Blackwood, W. Muir, A. Carothers, M. Walker, G. Spowart, C. Gosden, H.J. Evans, Association within a Family of a Balanced Autosomal Translocation with Major Mental-Illness, *Lancet*, 336 (1990) 13-16.

[10] H. Yamamoto, Y. Hagino, S. Kasai, K. Ikeda, Specific Roles of NMDA Receptor Subunits in Mental Disorders, *Curr Mol Med*, 15 (2015) 193-205.

[11] S.V. Sharma, D.W. Bell, J. Settleman, D.A. Haber, Epidermal growth factor receptor mutations in lung cancer, *Nat Rev Cancer*, 7 (2007) 169-181.

[12] S. Frantz, G. Ertl, J. Bauersachs, Mechanisms of disease: Toll-like receptors in cardiovascular disease, *Nat Clin Pract Cardiovasc Med*, 4 (2007) 444-454.

[13] J. Kang, H.G. Lemaire, A. Unterbeck, J.M. Salbaum, C.L. Masters, K.H. Grzeschik, G. Multhaup, K. Beyreuther, B. Muller-Hill, The precursor of Alzheimer's disease amyloid A4 protein resembles a cell-surface receptor, *Nature*, 325 (1987) 733-736.

[14] J. Schlessinger, Cell signaling by receptor tyrosine kinases, *Cell*, 103 (2000) 211-225.

[15] H. Metzger, Transmembrane Signaling - the Joy of Aggregation, *J Immunol*, 149 (1992) 1477-1487.

[16] N.R. Latorraca, A.J. Venkatakrishnan, R.O. Dror, GPCR Dynamics: Structures in Motion, *Chem Rev*, 117 (2017) 139-155.

[17] P.K. Mattila, F.D. Batista, B. Treanor, Dynamics of the actin cytoskeleton mediates receptor cross talk: An emerging concept in tuning receptor signaling, *J Cell Biol*, 212 (2016) 267-280.

[18] K. Henzler-Wildman, D. Kern, Dynamic personalities of proteins, *Nature*, 450 (2007) 964-972.

[19] S.P. Meisburger, W.C. Thomas, M.B. Watkins, N. Ando, X-ray Scattering Studies of Protein Structural Dynamics, *Chem Rev*, 117 (2017) 7615-7672.

[20] P.R.L. Markwick, T. Malliavin, M. Nilges, Structural Biology by NMR: Structure, Dynamics, and Interactions, *Plos Computational Biology*, 4 (2008).

[21] H.S. Mchaourab, M.A. Lietzow, K. Hideg, W.L. Hubbell, Motion of spin-labeled side chains in T4 lysozyme, correlation with protein structure and dynamics, *Biochemistry*, 35 (1996) 7692-7704.

[22] T.E. Wales, J.R. Engen, Hydrogen exchange mass spectrometry for the analysis of protein dynamics, *Mass Spectrom Rev*, 25 (2006) 158-170.

[23] L. Konermann, J.X. Pan, Y.H. Liu, Hydrogen exchange mass spectrometry for studying protein structure and dynamics, *Chemical Society Reviews*, 40 (2011) 1224-1234.

[24] M.C. Thielges, J.Y. Axup, D. Wong, H.S. Lee, J.K. Chung, P.G. Schultz, M.D. Fayer, Two-Dimensional IR Spectroscopy of Protein Dynamics Using Two Vibrational Labels: A Site-Specific Genetically Encoded Unnatural Amino Acid and an Active Site Ligand, *Journal of Physical Chemistry B*, 115 (2011) 11294-11304.

[25] I. Lopez-Pena, B.S. Leigh, D.E. Schlamadinger, J.E. Kim, Insights into Protein Structure and Dynamics by Ultraviolet and Visible Resonance Raman Spectroscopy, *Biochemistry*, 54 (2015) 4770-4783.

[26] N.N. Giakoumakis, M.A. Rapsomaniki, Z. Lygerou, Analysis of Protein Kinetics Using Fluorescence Recovery After Photobleaching (FRAP), *Methods Mol Biol*, 1563 (2017) 243-267.

[27] F. Mueller, D. Mazza, T.J. Stasevich, J.G. McNally, FRAP and kinetic modeling in the analysis of nuclear protein dynamics: what do we really know?, *Current Opinion in Cell Biology*, 22 (2010) 403-411.

[28] E.A.J. Reits, J.J. Neefjes, From fixed to FRAP: measuring protein mobility and activity in living cells, *Nat Cell Biol*, 3 (2001) E145-E147.

[29] T.J. Feder, I. BrustMascher, J.P. Slattery, B. Baird, W.W. Webb, Constrained diffusion or immobile fraction on cell surfaces: A new interpretation, *Biophysical Journal*, 70 (1996) 2767-2773.

[30] J. Ellenberg, E.D. Siggia, J.E. Moreira, C.L. Smith, J.F. Presley, H.J. Worman, J. LippincottSchwartz, Nuclear membrane dynamics and reassembly in living cells: Targeting of an inner nuclear membrane protein in interphase and mitosis, *Journal of Cell Biology*, 138 (1997) 1193-1206.

[31] N.B. Cole, C.L. Smith, N. Sciaky, M. Terasaki, M. Edidin, J. LippincottSchwartz, Diffusional mobility of Golgi proteins in membranes of living cells, *Science*, 273 (1996) 797-801.

[32] M. Dundr, U. Hoffmann-Rohrer, Q.Y. Hu, I. Grummt, L.I. Rothblum, R.D. Phair, T. Misteli, A kinetic framework for a mammalian RNA polymerase in vivo, *Science*, 298 (2002) 1623-1626.

[33] Y. Ishihama, H. Tadakuma, T. Tani, T. Funatsu, The dynamics of pre-mRNAs and poly(A)(+) RNA at speckles in living cells revealed by iFRAP studies, *Experimental Cell Research*, 314 (2008) 748-762.

[34] A.J. Ehrlicher, F. Nakamura, J.H. Hartwig, D.A. Weitz, T.P. Stossel, Mechanical strain in actin networks regulates FilGAP and integrin binding to filamin A, *Nature*, 478 (2011) 260-U154.

[35] G.A. Dunn, I.M. Dobbie, J. Monypenny, M.R. Holt, D. Zicha, Fluorescence localization after photobleaching (FLAP): a new method for studying protein dynamics in living cells, *J Microsc-Oxford*, 205 (2002) 109-112.

[36] J. Lippincott-Schwartz, J.F. Presley, K.J. Zaal, K. Hirschberg, C.D. Miller, J. Ellenberg, Monitoring the dynamics and mobility of membrane proteins tagged with green fluorescent protein, *Methods Cell Biol*, 58 (1999) 261-281.

[37] K.D. Sullivan, E.B. Brown, Multiphoton fluorescence recovery after photobleaching in bounded systems, *Phys Rev E Stat Nonlin Soft Matter Phys*, 83 (2011) 051916.

[38] K.D. Sullivan, W.H. Sipprell, 3rd, E.B. Brown, Jr., E.B. Brown, 3rd, Improved model of fluorescence recovery expands the application of multiphoton fluorescence recovery after photobleaching in vivo, *Biophys J*, 96 (2009) 5082-5094.

[39] S. Dorsch, K.N. Klotz, S. Engelhardt, M.J. Lohse, M. Bunemann, Analysis of receptor oligomerization by FRAP microscopy, *Nature Methods*, 6 (2009) 225-230.

[40] S.T. Hess, S.H. Huang, A.A. Heikal, W.W. Webb, Biological and chemical applications of fluorescence correlation spectroscopy: A review, *Biochemistry*, 41 (2002) 697-705.

[41] L.C. Hwang, T. Wohland, Recent advances in fluorescence cross-correlation spectroscopy, *Cell Biochemistry and Biophysics*, 49 (2007) 1-13.

[42] J. Ries, P. Schwille, Fluorescence correlation spectroscopy, *Bioessays*, 34 (2012) 361-368.

[43] E.L. Elson, Fluorescence Correlation Spectroscopy: Past, Present, Future, *Biophysical Journal*, 101 (2011) 2855-2870.

[44] M. Wachsmuth, C. Conrad, J. Bulkescher, B. Koch, R. Mahen, M. Isokane, R. Pepperkok, J. Ellenberg, High-throughput fluorescence correlation spectroscopy enables analysis of proteome dynamics in living cells, *Nat Biotechnol*, 33 (2015) 384-U391.

[45] L.O. Tjernberg, A. Pramanik, S. Bjorling, P. Thyberg, J. Thyberg, C. Nordstedt, K.D. Berndt, L. Terenius, R. Rigler, Amyloid beta-peptide polymerization studied using fluorescence correlation spectroscopy, *Chem Biol*, 6 (1999) 53-62.

[46] R. Machan, Y.H. Foo, T. Wohland, On the Equivalence of FCS and FRAP: Simultaneous Lipid Membrane Measurements, *Biophysical Journal*, 111 (2016) 152-161.

[47] S. Basu, L.M. Needham, D. Lando, E.J.R. Taylor, K.J. Wohlfahrt, D. Shah, W. Boucher, Y.L. Tan, L.E. Bates, O. Tkachenko, J. Cramard, B.C. Lagerholm, C. Eggeling, B. Hendrich, D. Klenerman, S.F. Lee, E.D. Laue, FRET-enhanced photostability allows improved single-molecule tracking of proteins and protein complexes in live mammalian cells, *Nat Commun*, 9 (2018).

[48] M.L. Zhang, Z. Zhang, K.M. He, J.M. Wu, N. Li, R. Zhao, J.H. Yuan, H. Xiao, Y.Y. Zhang, X.H. Fang, Quantitative Characterization of the Membrane Dynamics of Newly Delivered TGF-beta Receptors by Single-Molecule Imaging, *Analytical Chemistry*, 90 (2018) 4282-4287.

[49] R. Iino, T. Iida, A. Nakamura, E. Saita, H.J. You, Y. Sako, Single-molecule imaging and manipulation of biomolecular machines and systems, *Bba-Gen Subjects*, 1862 (2018) 241-252.

[50] M.L.I.E. Harwardt, M.S. Dietz, M. Heilemann, T. Wohland, SPT and Imaging FCS Provide Complementary Information on the Dynamics of Plasma Membrane Molecules, *Biophysical Journal*, 114 (2018) 2432-2443.

[51] K. Welsher, H. Yang, Imaging the behavior of molecules in biological systems: breaking the 3D speed barrier with 3D multi-resolution microscopy, *Faraday Discuss*, 184 (2015) 359-379.

[52] T. Funatsu, Y. Harada, M. Tokunaga, K. Saito, T. Yanagida, Imaging of Single Fluorescent Molecules and Individual Atp Turnovers by Single Myosin Molecules in Aqueous-Solution, *Nature*, 374 (1995) 555-559.

[53] M.J. Saxton, K. Jacobson, Single-particle tracking: Applications to membrane dynamics, *Annu Rev Bioph Biom*, 26 (1997) 373-399.

[54] A. Kusumi, T.A. Tsunoyama, K.M. Hirosawa, R.S. Kasai, T.K. Fujiwara, Tracking single molecules at work in living cells, *Nat Chem Biol*, 10 (2014) 524-532.

[55] Y.P. Chang, F. Pinaud, J. Antelman, S. Weiss, Tracking bio-molecules in live cells using quantum dots, *Journal of Biophotonics*, 1 (2008) 287-298.

[56] E. Petryayeva, W.R. Algar, I.L. Medintz, Quantum Dots in Bioanalysis: A Review of Applications Across Various Platforms for Fluorescence Spectroscopy and Imaging, *Applied Spectroscopy*, 67 (2013) 215-252.

[57] K. Spendier, K.A. Lidke, D.S. Lidke, J.L. Thomas, Single-particle tracking of immunoglobulin E receptors (FcepsilonRI) in micron-sized clusters and receptor patches, *FEBS Lett*, 586 (2012) 416-421.

[58] A. Syed, Q. Zhu, E.A. Smith, Ligand binding affinity and changes in the lateral diffusion of receptor for advanced glycation endproducts (RAGE), *Biochim Biophys Acta*, 1858 (2016) 3141-3149.

[59] H. Liu, P. Dong, M.S. Ioannou, L. Li, J. Shea, H.A. Pasolli, J.B. Grimm, P.K. Rivlin, L.D. Lavis, M. Koyama, Z. Liu, Visualizing long-term single-molecule dynamics in vivo by stochastic protein labeling, *Proc Natl Acad Sci U S A*, 115 (2018) 343-348.

[60] D. Calebiro, F. Rieken, J. Wagner, T. Sungkaworn, U. Zabel, A. Borzi, E. Cocucci, A. Zurn, M.J. Lohse, Single-molecule analysis of fluorescently labeled G-protein-coupled receptors reveals complexes with distinct dynamics and organization, *P Natl Acad Sci USA*, 110 (2013) 743-748.

[61] I.F. Sbalzarini, P. Koumoutsakos, Feature point tracking and trajectory analysis for video imaging in cell biology, *J Struct Biol*, 151 (2005) 182-195.

[62] L. Niu, J. Yu, Investigating intracellular dynamics of FtsZ cytoskeleton with photoactivation single-molecule tracking, *Biophys J*, 95 (2008) 2009-2016.

[63] T.Y. Chen, A.G. Santiago, W. Jung, L. Krzeminski, F. Yang, D.J. Martell, J.D. Helmann, P. Chen, Concentration- and chromosome-organization-dependent regulator unbinding from DNA for transcription regulation in living cells, *Nat Commun*, 6 (2015) 7445.

[64] J.C. Gebhardt, D.M. Suter, R. Roy, Z.W. Zhao, A.R. Chapman, S. Basu, T. Maniatis, X.S. Xie, Single-molecule imaging of transcription factor binding to DNA in live mammalian cells, *Nat Methods*, 10 (2013) 421-426.

[65] S. Uphoff, R. Reyes-Lamothe, F. Garza de Leon, D.J. Sherratt, A.N. Kapanidis, Single-molecule DNA repair in live bacteria, *Proc Natl Acad Sci U S A*, 110 (2013) 8063-8068.

[66] G.J. Schutz, H. Schindler, T. Schmidt, Single-molecule microscopy on model membranes reveals anomalous diffusion, *Biophys J*, 73 (1997) 1073-1080.

[67] A. Matysik, R.S. Kraut, TrackArt: the user friendly interface for single molecule tracking data analysis and simulation applied to complex diffusion in mica supported lipid bilayers, *BMC Res Notes*, 7 (2014) 274.

[68] M.A. Deverall, E. Gindl, E.K. Sinner, H. Besir, J. Ruehe, M.J. Saxton, C.A. Naumann, Membrane lateral mobility obstructed by polymer-tethered lipids studied at the single molecule level, *Biophys J*, 88 (2005) 1875-1886.

[69] R. Simson, E.D. Sheets, K. Jacobson, Detection of Temporary Lateral Confinement of Membrane-Proteins Using Single-Particle Tracking Analysis, *Biophysical Journal*, 69 (1995) 989-993.

[70] S.A. Menchon, M.G. Martin, C.G. Dotti, APM_GUI: analyzing particle movement on the cell membrane and determining confinement, *Bmc Biophysics*, 5 (2012).

[71] P.J. Bosch, J.S. Kanger, V. Subramaniam, Classification of dynamical diffusion states in single molecule tracking microscopy, *Biophys J*, 107 (2014) 588-598.

[72] P.S. Weiss, Nobel prizes for super-resolution imaging, *ACS Nano*, 8 (2014) 9689-9690.

[73] R. Heintzmann, T. Huser, Super-Resolution Structured Illumination Microscopy, *Chemical Reviews*, 117 (2017) 13890-13908.

[74] H. Blom, J. Widengren, Stimulated Emission Depletion Microscopy, *Chemical Reviews*, 117 (2017) 7377-7427.

[75] M. Hofmann, C. Eggeling, S. Jakobs, S.W. Hell, Breaking the diffraction barrier in fluorescence microscopy at low light intensities by using reversibly photoswitchable proteins, *P Natl Acad Sci USA*, 102 (2005) 17565-17569.

[76] M. Bossi, J. Folling, M. Dyba, V. Westphal, S.W. Hell, Breaking the diffraction resolution barrier in far-field microscopy by molecular optical bistability, *New J Phys*, 8 (2006).

[77] S.W. Hell, M. Kroug, Ground-State-Depletion Fluorescence Microscopy - a Concept for Breaking the Diffraction Resolution Limit, *Appl Phys B-Lasers O*, 60 (1995) 495-497.

[78] T. Dertinger, R. Colyer, G. Iyer, S. Weiss, J. Enderlein, Fast, background-free, 3D super-resolution optical fluctuation imaging (SOFI), *P Natl Acad Sci USA*, 106 (2009) 22287-22292.

[79] M. Bates, M.J. Rust, B. Huang, X.W. Zhuang, Sub-diffraction-limit imaging by stochastic optical reconstruction microscopy, *Biophysical Journal*, (2007) 196a-196a.

[80] M. Bates, B. Huang, G.T. Dempsey, X.W. Zhuang, Multicolor super-resolution imaging with photo-switchable fluorescent probes, *Science*, 317 (2007) 1749-1753.

[81] S.T. Hess, T.P.K. Girirajan, M.D. Mason, Ultra-high resolution imaging by fluorescence photoactivation localization microscopy, *Biophysical Journal*, 91 (2006) 4258-4272.

[82] E. Betzig, G.H. Patterson, R. Sougrat, O.W. Lindwasser, S. Olenych, J.S. Bonifacino, M.W. Davidson, J. Lippincott-Schwartz, H.F. Hess, Imaging intracellular fluorescent proteins at nanometer resolution, *Science*, 313 (2006) 1642-1645.

[83] D.T. Burnette, P. Sengupta, Y.H. Dai, J. Lippincott-Schwartz, B. Kachar, Bleaching/blinking assisted localization microscopy for superresolution imaging using standard fluorescent molecules, *P Natl Acad Sci USA*, 108 (2011) 21081-21086.

[84] B. Huang, W.Q. Wang, M. Bates, X.W. Zhuang, Three-dimensional super-resolution imaging by stochastic optical reconstruction microscopy, *Science*, 319 (2008) 810-813.

[85] S. van de Linde, A. Loschberger, T. Klein, M. Heidbreder, S. Wolter, M. Heilemann, M. Sauer, Direct stochastic optical reconstruction microscopy with standard fluorescent probes, *Nat Protoc*, 6 (2011) 991-1009.

[86] M. Heilemann, S. van de Linde, A. Mukherjee, M. Sauer, Super-Resolution Imaging with Small Organic Fluorophores, *Angewandte Chemie-International Edition*, 48 (2009) 6903-6908.

[87] C.S. Wijesooriya, J.A. Peterson, P. Shrestha, E.J. Gehrmann, A.H. Winter, E.A. Smith, A Photoactivatable BODIPY Probe for Localization-Based Super-Resolution Cellular Imaging, *Angewandte Chemie International Edition*, 0 (2018).

[88] J. Gao, Y. Wang, M.J. Cai, Y.G. Pan, H.J. Xu, J.G. Jiang, H.B. Ji, H.D. Wang, Mechanistic insights into EGFR membrane clustering revealed by super-resolution imaging, *Nanoscale*, 7 (2015) 2511-2519.

[89] Y.S. Hu, H. Cang, B.F. Lillemeier, Superresolution imaging reveals nanometer- and micrometer-scale spatial distributions of T-cell receptors in lymph nodes, *Proc Natl Acad Sci U S A*, 113 (2016) 7201-7206.

[90] S.A. Shelby, D. Holowka, B. Baird, S.L. Veatch, Distinct Stages of Stimulated Fc epsilon RI Receptor Clustering and Immobilization Are Identified through Superresolution Imaging, *Biophysical Journal*, 105 (2013) 2343-2354.

[91] M. Neeper, A.M. Schmidt, J. Brett, S.D. Yan, F. Wang, Y.C. Pan, K. Elliston, D. Stern, A. Shaw, Cloning and expression of a cell surface receptor for advanced glycosylation end products of proteins, *J Biol Chem*, 267 (1992) 14998-15004.

[92] L. Yatime, G.R. Andersen, Structural insights into the oligomerization mode of the human receptor for advanced glycation end-products, *Febs J*, 280 (2013) 6556-6568.

[93] B.I. Hudson, A.Z. Kalea, M.D. Arriero, E. Harja, E. Boulanger, V. D'Agati, A.M. Schmidt, Interaction of the RAGE Cytoplasmic Domain with Diaphanous-1 Is Required for Ligand-stimulated Cellular Migration through Activation of Rac1 and Cdc42, *Journal of Biological Chemistry*, 283 (2008) 34457-34468.

[94] L.G. Bucciarelli, T. Wendt, L. Rong, E. Lalla, M.A. Hofmann, M.T. Goova, A. Taguchi, S.F. Yan, S.D. Yan, D.M. Stern, A.M. Schmidt, RAGE is a multiligand receptor of the immunoglobulin superfamily: implications for homeostasis and chronic disease, *Cell Mol Life Sci*, 59 (2002) 1117-1128.

[95] E. Leclerc, S.W. Vetter, The role of S100 proteins and their receptor RAGE in pancreatic cancer, *Biochim Biophys Acta*, 1852 (2015) 2706-2711.

[96] T. Ali, H. Badshah, T.H. Kim, M.O. Kim, Melatonin attenuates D-galactose-induced memory impairment, neuroinflammation and neurodegeneration via RAGE/NF-K B/JNK signaling pathway in aging mouse model, *J Pineal Res*, 58 (2015) 71-85.

[97] Z. Cai, N. Liu, C. Wang, B. Qin, Y. Zhou, M. Xiao, L. Chang, L.J. Yan, B. Zhao, Role of RAGE in Alzheimer's Disease, *Cell Mol Neurobiol*, (2015).

[98] F. Song, C. Hurtado del Pozo, R. Rosario, Y.S. Zou, R. Ananthakrishnan, X. Xu, P.R. Patel, V.M. Benoit, S.F. Yan, H. Li, R.A. Friedman, J.K. Kim, R. Ramasamy, A.W. Ferrante, Jr., A.M. Schmidt, RAGE regulates the metabolic and inflammatory response to high-fat feeding in mice, *Diabetes*, 63 (2014) 1948-1965.

[99] M.E. Bianchi, A.A. Manfredi, High-mobility group box 1 (HMGB1) protein at the crossroads between innate and adaptive immunity, *Immunol Rev*, 220 (2007) 35-46.

[100] T. Chavakis, A. Bierhaus, N. Al-Fakhri, D. Schneider, S. Witte, T. Linn, M. Nagashima, J. Morser, B. Arnold, K.T. Preissner, P.P. Nawroth, The pattern recognition receptor (RAGE) is a counterreceptor for leukocyte integrins: A novel pathway for inflammatory cell recruitment, *J Exp Med*, 198 (2003) 1507-1515.

[101] T. Chavakis, E.Y. Choi, C.P. Xie, E. Chavakis, C. Gahmberg, M. Bianchi, P. Nawroth, V. Orlova, A novel pathway of HMGB1-mediated inflammatory cell recruitment that requires Mac-1-integrin, *Faseb J*, 21 (2007) A126-A126.

[102] C. Haupt, M. Bereza, S.T. Kumar, B. Kieninger, I. Morgado, P. Hortschansky, G. Fritz, C. Rocken, U. Horn, M. Fandrich, Pattern recognition with a fibril-specific antibody fragment reveals the surface variability of natural amyloid fibrils, *J Mol Biol*, 408 (2011) 529-540.

[103] I. Marenholz, C.W. Heizmann, G. Fritz, S100 proteins in mouse and man: from evolution to function and pathology (including an update of the nomenclature), *Biochem Biophys Res Commun*, 322 (2004) 1111-1122.

[104] S.D. Yan, D. Stern, M.D. Kane, Y.M. Kuo, H.C. Lampert, A.E. Roher, RAGE-Abeta interactions in the pathophysiology of Alzheimer's disease, *Restor Neurol Neurosci*, 12 (1998) 167-173.

[105] S.J. Kim, J.W. Ahn, H. Kim, H.J. Ha, S.W. Lee, H.K. Kim, S. Lee, H.S. Hong, Y.H. Kim, C.Y. Choi, Two beta-strands of RAGE participate in the recognition and transport of amyloid-beta peptide across the blood brain barrier, *Biochem Biophys Res Commun*, 439 (2013) 252-257.

[106] J. Xue, V. Rai, D. Singer, S. Chabierski, J.J. Xie, S. Reverdatto, D.S. Burz, A.M. Schmidt, R. Hoffmann, A. Shekhtman, Advanced Glycation End Product Recognition by the Receptor for AGEs, *Structure*, 19 (2011) 722-732.

[107] J. Xie, S. Reverdatto, A. Frolov, R. Hoffmann, D.S. Burz, A. Shekhtman, Structural basis for pattern recognition by the receptor for advanced glycation end products (RAGE), *J Biol Chem*, 283 (2008) 27255-27269.

[108] H.L. Zong, A. Madden, M. Ward, M.H. Mooney, C.T. Elliott, A.W. Stitt, Homodimerization Is Essential for the Receptor for Advanced Glycation End Products (RAGE)-mediated Signal Transduction, *Journal of Biological Chemistry*, 285 (2010) 23135-23144.

[109] D. Xu, J.H. Young, J.M. Krahn, D. Song, K.D. Corbett, W.J. Chazin, L.C. Pedersen, J.D. Esko, Stable RAGE-heparan sulfate complexes are essential for signal transduction, *ACS Chem Biol*, 8 (2013) 1611-1620.

[110] Y. Xu, F. Toure, W. Qu, L. Lin, F. Song, X. Shen, R. Rosario, J. Garcia, A.M. Schmidt, S.F. Yan, Advanced glycation end product (AGE)-receptor for AGE (RAGE) signaling and up-regulation of Egr-1 in hypoxic macrophages, *J Biol Chem*, 285 (2010) 23233-23240.

[111] A. Shekhtman, R. Ramasamy, A.M. Schmidt, Glycation & the RAGE axis: targeting signal transduction through DIAPH1, *Expert Review of Proteomics*, 14 (2017) 147-156.

## 1.6 Figures and Tables

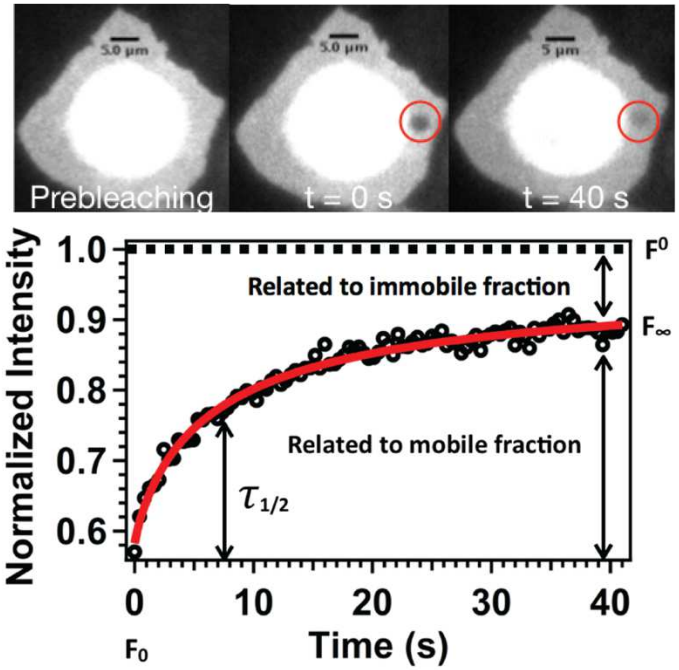


**Figure 1.1.** FRAP images of a Drosophila S2 cells tagged with yellow fluorescence protein. Top panel: images from left to right represent pre-bleach, bleach, and recovery after bleaching events. Bottom panel: recovery curve measured from the bleach region (red circle on the top panel). The red curve is fit using equation (1-2).

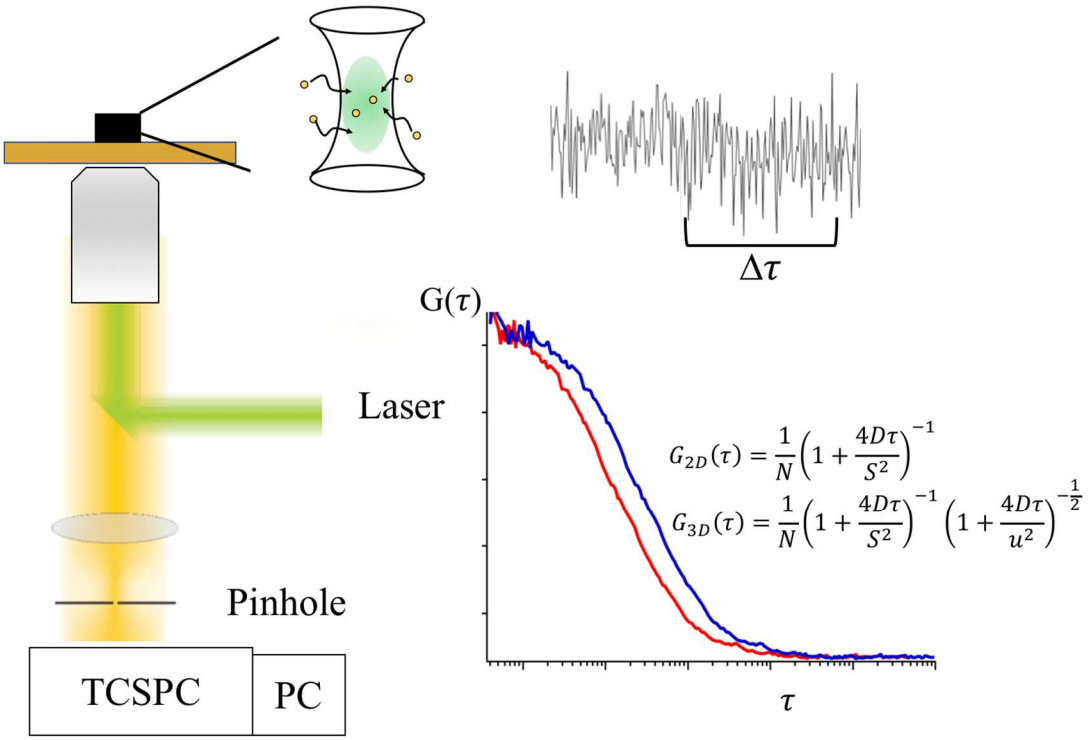


**Figure 1.2.** Schematic showing the principle of fluorescence correlation spectroscopy. Fluorescent molecules diffusing in and out of a confocal volume result in the intensity fluctuations over time $\Delta\tau$. The autocorrelation curve (plot of autocorrelation function $G(\tau)$ versus lag time $\tau$) is calculated as the autocorrelation of the intensity fluctuations and measures the self-similarity of the signal.

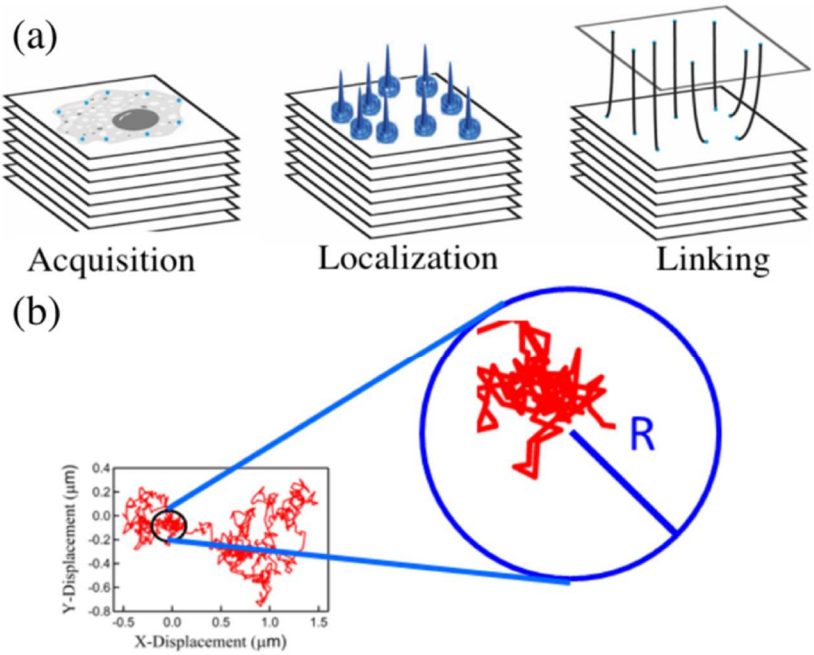


**Figure 1.3.** Schematic showing the steps in a single particle tracking experiments. (a) A series of images of quantum dot-labeled protein of interest is required. The single particles are localized in each frame and all the same particles are linked. (b) The trajectory of a single particle is plotted in the x-y dimension. An algorithm is applied to detect confined motion in a circle with radius R.

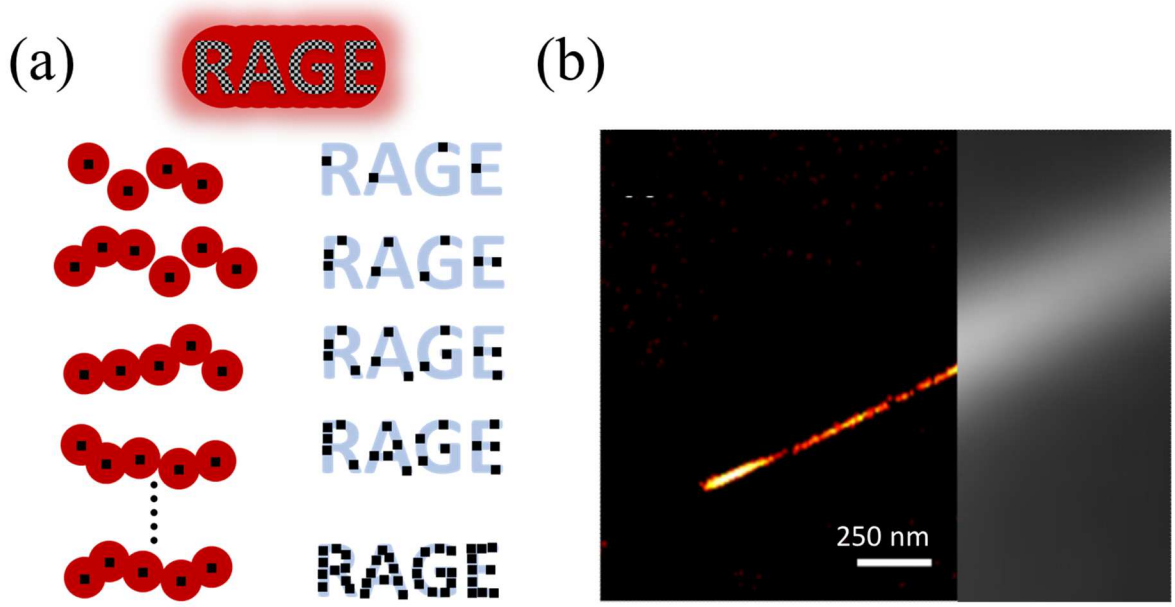


**Figure 1.4.** Schematic showing the principle of stochastic optical microscopy. (a) Individual receptor is labeled with a fluorophore. All fluorophores are switched to the off state with an appropriate wavelength and intensity of laser. A subset of fluorophores is reactivated with a lower-power light source. The activated fluorophores are statistically random, and under ideal conditions are separated by a distance greater than the diffraction limit of light so that the precise position of each fluorophore can be determined. Repeated cycles of activation, localization and deactivation are recorded to reconstruct an image. (b) Images of microtubules stained in vitro. The left color scale images are generated by single molecule localization microscopy. The right gray images are diffraction-limited images generated by summing all the frames without localization (Data collected by Chamari Wijesooriya).

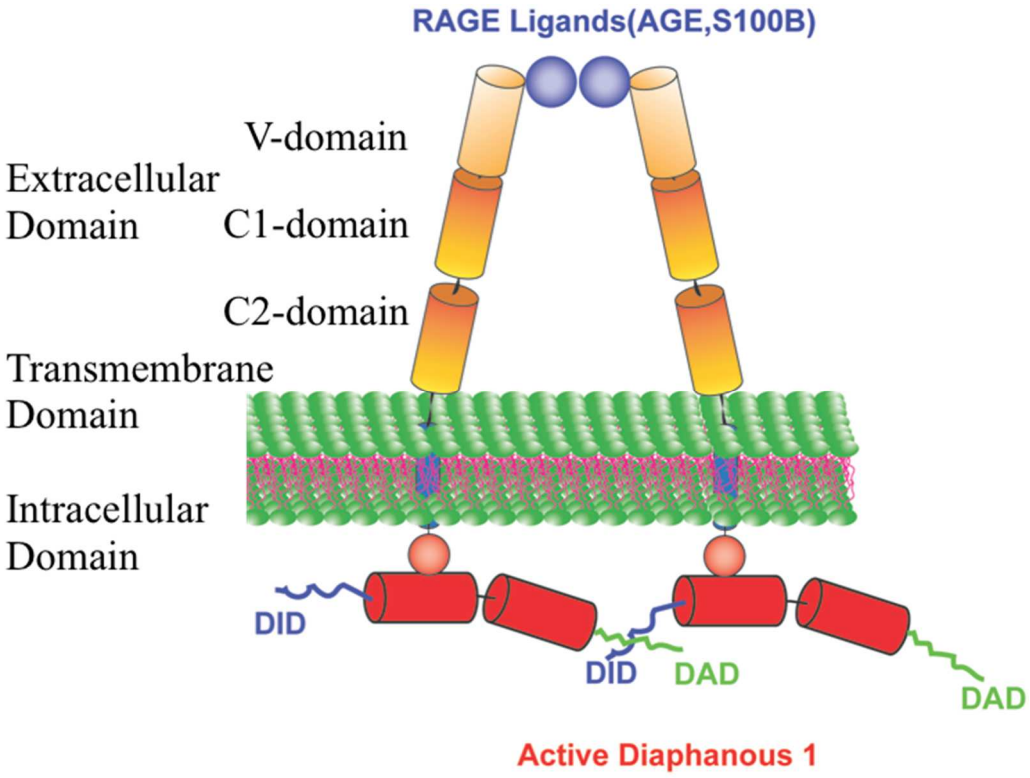


**Figure 1.5.** Domain structure of receptor for advanced glycation endproducts (RAGE) in the cell membrane with ligands and Diaphanous1 (Diaph1). DID and DAD are the Diaph1 autoregulatory domain and the Diaph1 inhibitory domain, respectively.

# CHAPTER 2. DIAPHANOUS-1 AFFECTS THE NANOSCALE CLUSTERING AND LATERAL DIFFUSION OF RECEPTOR FOR ADVANCED GLYCATION ENDPRODUCTS (RAGE)

Modified from a publication on the *BBA Biomembranes*

Qiaochu Zhu,[1] Emily A. Smith[1*]

[1]Department of Chemistry, Iowa State University, Ames, IA 50011, United States

## 2.1 Abstract

The interactions between the cytoplasmic protein diaphanous-1 (Diaph1) and the receptor for advanced glycation endproducts (RAGE) drive the negative consequences of RAGE signaling in several disease processes. Reported in this work is how Diaph1 affects the nanoscale clustering and diffusion of RAGE measured using super-resolution stochastic optical reconstruction microscopy (STORM) and single particle tracking (SPT). Altering the Diaph1 binding site has a different impact on RAGE diffusion compared to when Diaph1 expression is reduced in HEK 293 cells. In cells with reduced Diaph1 expression (RAGE-Diaph1$^{-/-}$), the average RAGE diffusion coefficient is increased by 35 %. RAGE diffusion is known to be influenced by the dynamics of the actin cytoskeleton. Actin labeling shows that reduced Diaph1 expression lead to the cells with reduced filopodia density and length. In contrast, when two RAGE amino acids that interact with Diaph1 are mutated ($RAGE_{RQ/AA}$), the average RAGE diffusion coefficient is decreased by 16 %. Since RAGE diffusion is slowed when the interaction between Diaph1 and RAGE is disrupted, the interaction of the two proteins results in faster RAGE diffusion. In both $RAGE_{RQ/AA}$ and RAGE-Diaph1$^{-/-}$ cells the number and size of RAGE clusters are decreased compared to cells expressing RAGE

and native concentrations of Diaph1. This work shows that Diaph1 has a role in affecting RAGE clusters and diffusion.

## 2.2 Introduction

The receptor for advanced glycation endproducts (RAGE) is a member of the immunoglobulin superfamily of cell surface proteins [1, 2], and has been implicated in the negative consequences of numerous chronic diseases based on evidence from human and animal studies [3-5]. RAGE exhibits promiscuous binding with multiple ligands, including S100/calgranulins [4, 6], advanced glycation endproducts [3], high mobility group box 1 [7], amyloid A or β peptide [8, 9], and Mac-1/β2 integrin [10]. Interactions between RAGE and its ligands are abnormally regulated in Alzheimer's disease, Parkinson's disease, diabetic neuropathy, inflammatory disease, and cardiovascular disease [11]. In addition, the elevated levels of RAGE ligands that may be present as a consequence of these diseases results in RAGE upregulation [12]. RAGE may be a good biomarker for many human diseases, and is also a potential therapeutic target [13]. There are, however, many missing details about the mechanisms that govern the biophysical properties of this important receptor.

RAGE consists of three extracellular domains, a transmembrane helix, and a short cytoplasmic tail. The V-type and C1-type extracellular domains are involved in ligand binding, while the C2 extracellular domain supports the rigid V-type/C1-type tandem domain. Ligand binding to the extracellular domain of RAGE initiates signal transduction [14, 15]. Downstream signaling includes phosphorylation of mitogen-activated protein kinase (MAPK), phosphatidylinositol 3-kinase (PI3K/Akt), Rho GTPases (Rac-1 and Cdc42) and activation of nuclear factor kappa B (NF- $\kappa$B) [16-18]. Several of the RAGE ligands are multivalent, including the S100/calgranulins (S100B, S100A12). The multivalent binding

drives RAGE clusters on the cell surface [6], which is an important aspect of downstream signal transduction [15, 16, 19, 20]. Changes in the size of RAGE clusters may affect the recruitment of Diaph1 and subsequent signal transduction pathways [21]. Based on data for a soluble variant of RAGE, Xie et al. proposed that full-length RAGE on the plasma membrane of HEK293T cells may form homooligomers, which would be nanoscale in size (i.e., below the diffraction limit of an optical microscope) [14].

RAGE signal transduction is a consequence of the interaction between the formin homology 1 (FH1) domain of diaphanous-1 (Diaph1) with the RAGE cytoplasmic tail [22-24]. Two amino acids, Arginine-5 (R5) and Glutamine-6 (Q6), of the RAGE cytoplasmic tail are essential for interactions with Diaph1 based on the lack of binding for a R5A/Q6A RAGE mutant [25]. When Diaph1 expression is reduced via RNA interference, RAGE singling through Akt is blocked and the migration of SMC cells is suppressed [22, 26]. Diaph1 plays an essential role in regulating a variety of cytoskeleton-dependent cellular processes under stimulation including actin and microtubule polymerization as well as the formation of filopodia for vesicle trafficking [27-31] Under non-stimulating conditions, Diaph1 controls cellular adhesion by stabilizing microtubules for localized clustering of integrin-β1 at the plasma membrane [32].

Although the cytoplasmic interactions between RAGE with Diaph1and the resulting signaling pathways have been studied, the effect of Diaph1 on RAGE diffusion and nanoscale clusters remains unknown. These properties can affect biomolecular interactions, signal transduction and overall cellular function [33-35]. In order to provide this missing information, single particle tracking (SPT) is used to individually track the diffusion of a subset of diffusely-labeled receptors and to test the role of Diaph1 in affecting RAGE

diffusion. In addition, the size of RAGE nanoscale clusters is measured using super-resolution stochastic optical reconstruction microscopy (STORM). Disrupting the interaction between RAGE and Diaph1 through protein mutation results in different RAGE clustering and diffusion properties compared to when Diaph1 expression is reduced altogether. The latter may be the result of disrupting the actin cytoskeleton when Diaph1 expression is reduced. This conclusion is supported by previous reports where we show that RAGE diffusion is altered by compounds that inhibit actin depolymerization [36].

## 2.3 Materials and Methods

### Cell culture, actin staining, and filopodia quantification

Details of RAGE plasmid construction, down-regulation of Diaph1, Western blotting and RT-PCR methods are provided in the supplementary material. Cells were plated onto an 8-well Nunc™ Lab-Tek™ chambered glass slide. For intracellular actin staining in HEK293 cells, cells were fixed with 4% paraformaldehyde (Sigma Aldrich) in PBS for 30 min at room temperature after rinsing cells with phosphate buffered saline (PBS) three times. Cells were washed twice with 1 mg/mL sodium borohydride (Fisher Chemical) in PBS for 5 min to quench cellular autofluorescence. The cells were permeabilized with 0.1% Triton-X100 (Thermo Scientific) in PBS for 5 min, and the actin filaments were stained using Alexa Fluor 488 phalloidin (1:100) (Invitrogen™) in PBS for 30 min. After rinsing the cells with PBS, they were imaged by using a Leica TCS SP5 confocal microscope with a 100×-magnification 1.4-NA oil-immersion objective. Images were collected with a frame rate of 200 Hz and 400 nm z-step size. The ImageJ plugin FiloQuant was used to quantify the filopodia length and density [37, 38]. The filopodia density is defined as the ratio of the number of filopodia per a given length of the cell edge.

**STORM and clusters analysis**

An 8-well Nunc™ Lab-Tek™ chambered glass slide was sonicated in 1M KOH for 15 min then rinsed with deionized water. The glass slide was coated with 0.01% poly-l-lysine solution then washed with deionized water and dried under ultraviolet radiation. Cells were subcultured onto the glass slide until 60% confluence was achieved. The cells were washed with PBS twice then fixed with 1% paraformaldehyde for 10 min at room temperature. After three PBS washes, the cells were incubated with anti-RAGE antibody (1:100) in incubation buffer (5% normal goat serum (Invitrogen™) and 1% BSA prepared in PBS solution) for 1h at room temperature. The RAGE primary antibody interacts with the extracellular domain of RAGE. The cells were washed with incubation buffer three times and then incubated with Alexa Fluor 647 F(ab')2-Goat anti-rabbit (A21246, Invitrogen™) (1:1000) for 30 min at room temperature. After three PBS washes, 800 µL of imaging buffer (50 mM NaCl, 10% glucose, 0.5 mg/mL glucose oxidase, 40 µg/mL catalase, and 50 mM cysteamine in 10 mM Tris, pH = 8.0) were added into each well then covered by a glass coverslip. The labeling conditions used in this study ensure that the signal is coming only from receptor in the membrane. No detectable labeling was measured for HEK293 cells that lack the expression of exogenous RAGE. For STORM experiments, a Nikon TE2000U epifluorescence/TIRF microscope equipped with a 100× 1.49 NA oil immersion objective and a 635-nm excitation laser (LQC635, CW laser diode, Newport) with a power density of 1.5 KW/cm$^2$ were used. Movies were collected with 15,000 frames, a 40 ms exposure time, and a 64×64 frame size using a EMCCD (Andor iXon$^{EM}$+ DU-897). The ImageJ plugin ThunderSTORM was used to localize single molecules in each frame of the movie and to construction super resolution images [39]. Briefly, the size of each pixel (0.16 µm/pixel), photoelectrons per A/D count EM gain (600), exposure time (40 ms) were used as inputs for the camera settings. Single

molecules were localized using weighted least-squares fitting of an integrated Gaussian PSF enabled to detect up to two single molecules within a diffraction-limited area. The localization precision and Ripley's K analysis were performed using LocAlization Microscopy Analyzer (LAMA) [40].

**Single particle tracking**

Cells were subcultured onto 8-well Nunc™ Lab-Tek™ chambered glass slides that were coated with 0.01% poly-L-lysine solution (P4704, Sigma Aldrich) for 48 h. The medium was changed to 3% BSA in DMEM for 18 h to coat any remaining glass surface. The anti-HA labeled QDs (AHA-QDs) were prepared as previously published [41]. After 100 pM AHA-QDs were diluted in imaging buffer (20 μM HEPES, 6 μM D-glucose, 0.3 μM $Na_2HPO_4$, 138 μM NaCl, 4 μM $NaHCO_3$, 0.4 μM $KH_2PO_4$, 5 μM KCl, 0.4 μM $MgSO_4 \cdot 7H_2O$, 0.5 μM $MgCl_2 \cdot 6H_2O$, 1 μM $CaCl_2$) with 0.1% BSA, cells were incubated with AHA-QDs for 15 min at 37 °C. This labeling method is highly specific to cells expressing RAGE. In Figure S2.1, there is an average of 2 ± 1 QDs per wild-type HEK293 cell that does not have detectable levels of RAGE as measured by Western blot analysis. The QDs measured in wild-type HEK293 cells exhibit no movement within the uncertainty of the localization measurement, and have an average diffusion coefficient less than 0.0018 $\mu m^2/s$. In cells expressing transgenic RAGE, an average of 20 ± 10 QDs per cell is bound to the cell (Figure S2.1). In order prevent skewing the SPT results with signals that may correspond to QDs not bound to RAGE (nonspecific binding), only trajectories that result in a RAGE diffusion coefficient larger than 0.0018 μm/s were considered.

Cells were washed with imaging buffer before performing microscopy experiments. SPT experiments were performed at 37 °C with an Eclipse Nikon (TE2000U) microscope in

wide-field, epi-mode with a 100× 1.4 NA oil-immersion objective. The light from a mercury lamp was passed through a filter set (excitation: 425/25 nm; emission: 605/20 nm; Omega Optical. The signal was collected by an Andor iXon$^{EM}$+ DU-897 back-illuminated electron-multiplying charge coupled device (EMCCD) with a 40 ms acquisition time and 700 frames were collected. A 2D/3D single-particle tracking plug-in (MosaicSuite) for ImageJ was used to track single particles in each frame over time to generate trajectories of x-y location [41-43].

More than 150 single particle trajectories from at least 20 cells were collected for each cell line, and were subsequently analyzed using TrackArt, which is a MATLAB application based on a previously described algorithm [44, 45]. To quantify RAGE diffusion on the ensemble level, the mean square displacement (MSD, $r^2$) was determined by the cumulative probability distribution (CPD) of the square displacement over consecutive time lags (4s). This method has been extensively used to quantify the diffusion coefficient and fractional populations in multiple system [46-49]. CPD is defined as the probability that a particle remains within a circle with a radius r. The fraction (f) of each population can be separately estimated. A single population exhibiting Brownian motion yields a single exponential model (1p model) and can be fit by:

$$CPD(r^2, t) = 1 - \exp(-\frac{r^2}{4Dt})$$

where D is the diffusion coefficient. The goodness-of-fit was determined by calculating the residual sum of squares. If a single exponential model failed to accurately fit the data, then a double exponential model (2p model) was used:

$$CPD(r^2, t) = 1 - \langle f \exp\left(-\frac{r^2}{4D_f t}\right) + (1 - f) \exp\left(-\frac{r^2}{4D_s t}\right)\rangle$$

The 2p model produces two diffusion coefficients: $D_f$ for the fast population and $D_s$ for the slow population. The fit results also provide the relative fractions f and 1 – f for the fast population and slow population, respectively [50].

The MATLAB APM_GUI based on an algorithm developed by Simson and Menchon [51, 52] was used to detect confined motion within each trajectory. Confined motion is defined as diffusive motion that is restricted by boundaries that cannot be crossed [53]. Within the confinement boundaries, Brownian diffusion may occur. Briefly, all trajectories were categorized as either Brownian motion or non-random (i.e., confined) motion based on the probability (L) of staying within a region of radius R. The critical confinement index ($L_c$) and critical confinement time ($t_c$) were obtained from simulated Brownian trajectories for a range of diffusion coefficients as previously described [41]. A trajectory with $L_c > 3.16$ and $t_c > 1.95$ is categorized as confined motion. If a trajectory exhibits confined motion, the diffusion coefficient inside confined domains ($D_{in}$), the size of the confined domain (R), and the time in the confined domain (t) were calculated.

**Statistical analysis**

The reported data was determined to exhibit a parametric distribution or non-parametric distribution using the Shapiro-Wilk Test for normality. The statistical significance of all parametric distributions was calculated using the F-test at the 95% confidence level and then a paired/unpaired (as determined by the F-test) Student's t-test with a two-tailed distribution. The statistical significance of all non-parametric distributions was calculated using the Mann-Whitney test with a two-tailed distribution. All resulting p-values below 0.05 are reported in the figures. If a p-value was not reported, its value was greater than 0.05 unless otherwise noted in the figure legend.

## 2.4 Results and Discussion

### RAGE forms nanoscale clusters that are altered when Diaph1 expression is reduced or when the interaction between Diaph1 and RAGE is altered

To measure RAGE clusters and diffusion under conditions of altered interaction with Diaph1, stably transfected HEK 293 cells were developed that expressed RAGE or RAGE with a R5A/Q6A mutation on the cytoplasmic tail ($RAGE_{RQ/AA}$). The amino acid sequence in the transmembrane domain and intracellular domain of RAGE and $RAGE_{RQ/AA}$ are shown in Figure S2.2a. An HA epitope was added to the extracellular domain of all RAGE sequences to facilitate specific labeling with an HA antibody. It has been shown that the cell signaling measured by phosphorylation of ERK is not altered in cells expressing RAGE with and without the HA epitope [41].

Diffraction-limited wide-field fluorescence images show a fairly uniform RAGE distribution throughout the cell membrane with a higher signal around the periphery of the cell (Figure 2.1a). STORM allows the RAGE distribution to be measured with 21-nm localization precision as determined by nearest-neighbor-based analysis. In Fig.1b and Fig.1c, RAGE clusters of varying size are observed; clusters are also measured for cells expressing $RAGE_{RQ/AA}$ (Figure S2.3). The amount and size of the clusters is quantified using Ripley's K-function analysis (Figure 2.1d). The integrated areas of the Ripley's K-function curves indicate there are more RAGE clusters compared to $RAGE_{RQ/AA}$ clusters. In addition, RAGE has clusters as large as 760 nm, however, $RAGE_{RQ/AA}$ does not exhibit clusters larger than 610 nm (i.e., there is a random distribution over a longer length scale). This shows that altering the interaction between RAGE and Diaph1 also alters the amount and size of RAGE clusters in HEK 293 cells. A previously reported NMR structural analysis showed that increasing the molecular dimension of RAGE resulted in recruiting Diaph1 and initiating

signal transduction [21]. When Diaph1 is not recruited due to altering the interaction between Diaph1 and RAGE, both RAGE clustering and its associated signal transduction pathways may be altered.

The influence of Diaph1 on RAGE clusters was further analyzed in a cell line with reduced Diaph1 expression (RAGE-Diaph1$^{-/-}$). The concentration of Diaph1 is reduced, but not eliminated in these experiments, as shown in Figure S2.2c and Figure S2.2d. Diaph1 is a formin family protein, and is known to affect the formation of actin filaments [28]. In order to confirm the reduced levels of Diaph1 achieved in this study had a similar effect on the actin cytoskeleton as previously reported, phalloidin staining of the actin cytoskeleton was measured (Figure 2.2a). As shown in Figure 2.2b-2.2c, the filopodia density ($0.24 \pm 0.05$ $\mu m^{-1}$) and length ($2.1 \pm 0.2$ $\mu m$) increase in cells expressing RAGE when compared to wild-type HEK 293 cells that do not express exogenous RAGE. This is consistent with previous reports [54]. The filopodia density and length decrease by 61% and 37%, respectively, in RAGE-Diaph1$^{-/-}$ cells compared with cells expressing both RAGE and Diaph1. After Diaph1 expression is reduced, the values are statistically the same as those measured for cells that do not express transgenic RAGE, indicating that the increased filopodia length and density resulting from RAGE expression can be eliminated by reducing the expression of Diaph1. In $RAGE_{RQ/AA}$ cells, the filopodia density and the filopodia length are decreased compared to cells expressing RAGE. This indicates that alterations to the actin cytoskeleton also occur in the cell line where the interaction between Diaph1 and RAGE is blocked, although the alterations are not as pronounced as when Diaph1 expression is reduced.

Fewer RAGE clusters are measured in the RAGE-Diaph1$^{-/-}$ cell line compared to cells expressing native Diaph1 levels (Figure 2.1d), which is consistent with the data for cells expressing $RAGE_{RQ/AA}$. The RAGE-Diaph1$^{-/-}$ cell line, however, exhibits a larger amount of smaller clusters. Also, the largest cluster size is 510 nm in the RAGE-Diaph1$^{-/-}$ cell line, which is smaller than the value for $RAGE_{RQ/AA}$. Reducing the concentration of Diaph1 and disrupting its interaction with RAGE produce both fewer and smaller RAGE clusters compared to the control cell line, but there may be distinct mechanisms for how the RAGE clusters are altered in these cell lines.

**RAGE diffusion in HEK 293 cells is altered differently when Diaph1 expression is reduced compared to when the Diaph1 binding site is altered**

RAGE diffusion was measured in HEK 293 cells using SPT. First a cumulative probability distribution (CPD) analysis of the trajectories was performed to determine the number of diffusing populations that could be measured as well as the diffusion coefficient of each population. Next the properties of transient confinement within each trajectory were measured to obtain the diffusion coefficient and residence time in confined domains as well as the sized of the confined domains.

As shown in Figure 2.3a-2.3b, RAGE diffusion (i.e., mean square displacement versus probability plot) is better fit by a model with two populations (2p model) than a model with one population (1p model). The two populations will be referred to as the fast fraction and slow fraction. The diffusion coefficient for each population can be obtained from a fit to the MSD versus time plot (Figure 2.3d-2.3e). There is no statistically significant difference between the fit for Brownian diffusion and anomalous motion for either the fast or the slow population, thus the simpler Brownian fit was used to quantify the diffusion coefficients. The RAGE diffusion coefficients for the fast ($D_f$) and slow ($D_s$) population are 0.107 $\mu m^2/s$ and

0.0149 $\mu m^2/s$, respectively. A 72% majority of the RAGE exhibits fast diffusion (Figure 2.3c).

The cumulative probability distribution curve for $RAGE_{RQ/AA}$ and RAGE-Diaph1$^{-/-}$ are also best described using a 2 population model (Figure S2.4a-2.4b, Figure S2.5a-2.5b). All fit results are summarized in Figure 2.4. Both the fast and slow diffusion coefficient for $RAGE_{RQ/AA}$ show a statistically significant decrease to 0.094 $\mu m^2/s$ and 0.011$\mu m^2/s$, respectively, compared with the diffusion coefficients for RAGE (Figure 2.4b-Figure 2.4c). The interaction between RAGE and Diaph1 increases RAGE diffusion, which is slower when the RAGE/Diaph1 interaction is blocked at the known binding site on RAGE.

When Diaph1 expression is reduced, there is an increase in the fast diffusion coefficient for RAGE to 0.162 $\mu m^2/s$ (Figure 2.4b), which may be the result of disrupting the protein interaction (or possibly a protein complex) or it may be the result of the altered cytoskeleton (Figure 2.2). In a previous study, we showed the RAGE diffusion coefficient decreased by 37 % when actin filament depolymerization is inhibited by treatment with jasplakinolide in GM07373 cells [36]. Considering this previous finding, it is not surprising to measure a 35 % increase in the average RAGE diffusion coefficient when actin polymerization is reduced by the lower expression levels of Diaph1. It is proposed that the population of RAGE with a faster diffusion coefficient is impacted by the structure of the actin cytoskeleton, which is why this population has a faster diffusion coefficient when Diaph1 expression is reduced.

RAGE diffusion exhibits transient events that represent diffusion within confined domains (Figure S2.6). Additional information about RAGE diffusion within confined domains can be obtained from analyzing the local displacement of segments of each

trajectory. The average diffusion coefficient of RAGE in confined domains ($D_{in}$) is 0.018 $\mu m^2/s$ (Figure 2.5a). The average diffusion coefficient of $RAGE_{RQ/AA}$ within confined domains is statistically lower (0.013 $\mu m^2/s$). Both the magnitude of the diffusion coefficient as well as the relative decrease when comparing the diffusion coefficients for RAGE and $RAGE_{RQ/AA}$ suggest that the slow population from the CPD analysis may represent those receptors that are diffusing within confined domains. Coincident with the decrease in the diffusion coefficient for $RAGE_{RQ/AA}$ in confined domains, there is also a decrease in the size of the confined domains (0.18 μm) compared to RAGE (0.23 μm) (Figure 2.5b). For all other cellular conditions, the differences in the diffusion coefficient and size of confined domains were not statistically significant ($p > 0.02$). (Figure 2.5c).

## 2.5 Conclusions and Future Insights

Diaph1 affects RAGE clusters and RAGE's diffusion properties. Reducing the expression of Diaph1 and eliminating the binding site to RAGE have similar effects on reducing the size and number of RAGE clusters, but do not have the same effects on RAGE diffusion. Decreased RAGE diffusion is only measured when the known site of interaction with Diaph1 is altered on the RAGE cytoplasmic tail. Both the fast and slow populations are affected, and the changes to the slow population may correlate with alterations to properties of confined domains in the membrane. Reducing the expression of Diaph1 increases RAGE diffusion; the mechanism is proposed to involve the concomitant changes to actin polymerization. This shows that Diaph1 can affect RAGE diffusion and clusters, and that these properties are influenced by the intracellular environment.

**Author contributions**

Q.Z. and E.A.S. designed the research, analyzed the results, and wrote the manuscript. Q.Z. developed the cell lines used in this study and performed the experiments.

**Acknowledgements**

This work was initiated with funding from NSF grant CHE-1412084 and was continued with funding from NSF grant CHE-1709099. The authors thank Dr. Aleem Syed for useful discussion and help with protein cloning.

## 2.6 References

[1] M. Neeper, A.M. Schmidt, J. Brett, S.D. Yan, F. Wang, Y.C. Pan, K. Elliston, D. Stern, A. Shaw, Cloning and expression of a cell surface receptor for advanced glycosylation end products of proteins, *J Biol Chem*, 267 (1992) 14998-15004.

[2] A.M. Schmidt, M. Vianna, M. Gerlach, J. Brett, J. Ryan, J. Kao, C. Esposito, H. Hegarty, W. Hurley, M. Clauss, et al., Isolation and characterization of two binding proteins for advanced glycosylation end products from bovine lung which are present on the endothelial cell surface, *J Biol Chem*, 267 (1992) 14987-14997.

[3] A.M. Schmidt, M. Hasu, D. Popov, J.H. Zhang, J.X. Chen, S.D. Yan, J. Brett, R. Cao, K. Kuwabara, G. Costache, N. Simionescu, M. Simionescu, D. Stern, Receptor for Advanced Glycation End-Products (Ages) Has a Central Role in-Vessel Wall Interactions and Gene Activation in Response to Circulating Age Proteins, *P Natl Acad Sci USA*, 91 (1994) 8807-8811.

[4] M.A. Hofmann, S. Drury, C. Fu, W. Qu, A. Taguchi, Y. Lu, C. Avila, N. Kambham, A. Bierhaus, P. Nawroth, M.F. Neurath, T. Slattery, D. Beach, J. McClary, M. Nagashima, J. Morser, D. Stern, A.M. Schmidt, RAGE mediates a novel proinflammatory axis: a central cell surface receptor for S100/calgranulin polypeptides, *Cell*, 97 (1999) 889-901.

[5] J.K. Juranek, G.K. Daffu, J. Wojtkiewicz, D. Lacomis, J. Kofler, A.M. Schmidt, Receptor for Advanced Glycation End Products and its Inflammatory Ligands are Upregulated in Amyotrophic Lateral Sclerosis, *Front Cell Neurosci*, 9 (2015) 485.

[6] T. Ostendorp, E. Leclerc, A. Galichet, M. Koch, N. Demling, B. Weigle, C.W. Heizmann, P.M.H. Kroneck, G. Fritz, Structural and functional insights into RAGE activation by multimeric S100B, *Embo Journal*, 26 (2007) 3868-3878.

[7] J.R. Klune, R. Dhupar, J. Cardinal, T.R. Billiar, A. Tsung, HMGB1: endogenous danger signaling, *Mol Med*, 14 (2008) 476-484.

[8] S.D. Yan, H. Zhu, A. Zhu, A. Golabek, H. Du, A. Roher, J. Yu, C. Soto, A.M. Schmidt, D. Stern, M. Kindy, Receptor-dependent cell stress and amyloid accumulation in systemic amyloidosis, *Nat Med*, 6 (2000) 643-651.

[9] R. Deane, S. Du Yan, R.K. Submamaryan, B. LaRue, S. Jovanovic, E. Hogg, D. Welch, L. Manness, C. Lin, J. Yu, H. Zhu, J. Ghiso, B. Frangione, A. Stern, A.M. Schmidt, D.L. Armstrong, B. Arnold, B. Liliensiek, P. Nawroth, F. Hofman, M. Kindy, D. Stern, B. Zlokovic, RAGE mediates amyloid-beta peptide transport across the blood-brain barrier and accumulation in brain, *Nat Med*, 9 (2003) 907-913.

[10] T. Chavakis, A. Bierhaus, N. Al-Fakhri, D. Schneider, S. Witte, T. Linn, M. Nagashima, J. Morser, B. Arnold, K.T. Preissner, P.P. Nawroth, The pattern recognition receptor (RAGE) is a counterreceptor for leukocyte integrins: A novel pathway for inflammatory cell recruitment, *J Exp Med*, 198 (2003) 1507-1515.

[11] J. Juranek, R. Ray, M. Banach, V. Rai, Receptor for advanced glycation end-products in neurodegenerative diseases, *Rev Neurosci*, 26 (2015) 691-698.

[12] J. Li, A.M. Schmidt, Characterization and functional analysis of the promoter of RAGE, the receptor for advanced glycation end products, *J Biol Chem*, 272 (1997) 16498-16506.

[13] E.J. Lee, J.H. Park, Receptor for Advanced Glycation Endproducts (RAGE), Its Ligands, and Soluble RAGE: Potential Biomarkers for Diagnosis and Therapeutic Targets for Human Renal Diseases, *Genomics Inform*, 11 (2013) 224-229.

[14] J. Xie, S. Reverdatto, A. Frolov, R. Hoffmann, D.S. Burz, A. Shekhtman, Structural basis for pattern recognition by the receptor for advanced glycation end products (RAGE), *J Biol Chem*, 283 (2008) 27255-27269.

[15] L. Yatime, G.R. Andersen, Structural insights into the oligomerization mode of the human receptor for advanced glycation end-products, *Febs J*, 280 (2013) 6556-6568.

[16] H.J. Huttunen, C. Fages, H. Rauvala, Receptor for advanced glycation end products (RAGE)-mediated neurite outgrowth and activation of NF-kappaB require the cytoplasmic domain of the receptor but different downstream signaling pathways, *J Biol Chem*, 274 (1999) 19919-19924.

[17] R. Bianchi, E. Kastrisianaki, I. Giambanco, R. Donato, S100B protein stimulates microglia migration via RAGE-dependent up-regulation of chemokine expression and release., *The Journal of biological chemistry*, 286 (2011) 7214-7226.

[18] A. Rouhiainen, J. Kuja-Panula, S. Tumova, H. Rauvala, RAGE-mediated cell signaling, *Methods Mol Biol*, 963 (2013) 239-263.

[19] H.L. Zong, A. Madden, M. Ward, M.H. Mooney, C.T. Elliott, A.W. Stitt, Homodimerization Is Essential for the Receptor for Advanced Glycation End Products (RAGE)-mediated Signal Transduction, *Journal of Biological Chemistry*, 285 (2010) 23135-23144.

[20] K. Ishihara, K. Tsutsumi, S. Kawane, M. Nakajima, T. Kasaoka, The receptor for advanced glycation end-products (RAGE) directly binds to ERK by a D-domain-like docking site, *FEBS Lett*, 550 (2003) 107-113.

[21] J. Xue, M. Manigrasso, M. Scalabrin, V. Rai, S. Reverdatto, D.S. Burz, D. Fabris, A.M. Schmidt, A. Shekhtman, Change in the Molecular Dimension of a RAGE-Ligand Complex Triggers RAGE Signaling, *Structure*, 24 (2016) 1509-1522.

[22] B.I. Hudson, A.Z. Kalea, M.D. Arriero, E. Harja, E. Boulanger, V. D'Agati, A.M. Schmidt, Interaction of the RAGE Cytoplasmic Domain with Diaphanous-1 Is Required for Ligand-stimulated Cellular Migration through Activation of Rac1 and Cdc42, *Journal of Biological Chemistry*, 283 (2008) 34457-34468.

[23] Y. Xu, F. Toure, W. Qu, L. Lin, F. Song, X. Shen, R. Rosario, J. Garcia, A.M. Schmidt, S.F. Yan, Advanced glycation end product (AGE)-receptor for AGE (RAGE) signaling and up-regulation of Egr-1 in hypoxic macrophages, *J Biol Chem*, 285 (2010) 23233-23240.

[24] A. Shekhtman, R. Ramasamy, A.M. Schmidt, Glycation & the RAGE axis: targeting signal transduction through DIAPH1, *Expert Review of Proteomics*, 14 (2017) 147-156.

[25] V. Rai, A.Y. Maldonado, D.S. Burz, S. Reverdatto, S.F. Yan, A.M. Schmidt, A. Shekhtman, Signal transduction in receptor for advanced glycation end products (RAGE): solution structure of C-terminal rage (ctRAGE) and its binding to mDia1, *J Biol Chem*, 287 (2012) 5133-5144.

[26] F. Toure, G. Fritz, Q. Li, V. Rai, G. Daffu, Y.S. Zou, R. Rosario, R. Ramasamy, A.S. Alberts, S.F. Yan, A.M. Schmidt, Formin mDia1 mediates vascular remodeling via integration of oxidative and signal transduction pathways, *Circ Res*, 110 (2012) 1279-1293.

[27] B.R. Acharya, S.K. Wu, Z.Z. Lieu, R.G. Parton, S.W. Grill, A.D. Bershadsky, G.A. Gomez, A.S. Yap, Mammalian Diaphanous 1 Mediates a Pathway for E-cadherin to Stabilize Epithelial Barriers through Junctional Contractility, *Cell Rep*, 18 (2017) 2854-2867.

[28] C. Higashida, T. Miyoshi, A. Fujita, F. Oceguera-Yanez, J. Monypenny, Y. Andou, S. Narumiya, N. Watanabe, Actin polymerization-driven molecular movement of mDia1 in living cells, *Science*, 303 (2004) 2007-2010.

[29] A.F. Palazzo, T.A. Cook, A.S. Alberts, G.G. Gundersen, mDia mediates Rho-regulated formation and orientation of stable microtubules, *Nat Cell Biol*, 3 (2001) 723-729.

[30] S. Narumiya, M. Tanji, T. Ishizaki, Rho signaling, ROCK and mDia1, in transformation, metastasis and invasion, *Cancer Metastasis Rev*, 28 (2009) 65-76.

[31] H. Mellor, The role of formins in filopodia formation, *Biochim Biophys Acta*, 1803 (2010) 191-200.

[32] Y.N. Lin, R. Bhuwania, K. Gromova, A.V. Failla, T. Lange, K. Riecken, S. Linder, M. Kneussel, J.R. Izbicki, S. Windhorst, Drosophila homologue of Diaphanous 1 (DIAPH1) controls the metastatic potential of colon cancer cells by regulating microtubule-dependent adhesion, *Oncotarget*, 6 (2015) 18577-18589.

[33] R.J. Cherry, Rotational and lateral diffusion of membrane proteins, *Biochim Biophys Acta*, 559 (1979) 289-327.

[34] S. Ramadurai, A. Holt, V. Krasnikov, G. van den Bogaart, J.A. Killian, B. Poolman, Lateral diffusion of membrane proteins, *J Am Chem Soc*, 131 (2009) 12650-12656.

[35] P.A. Liebman, A historical perspective on the lateral diffusion model of GTPase activation and related coupling of membrane signaling proteins, *Cell Logist*, 4 (2014) e29389.

[36] A. Syed, Q. Zhu, E.A. Smith, Lateral diffusion and signaling of receptor for advanced glycation end-products (RAGE): a receptor involved in chronic inflammation, *Eur Biophys J*, (2017).

[37] G. Jacquemet, I. Paatero, A.F. Carisey, A. Padzik, J.S. Orange, H. Hamidi, J. Ivaska, FiloQuant reveals increased filopodia density during breast cancer progression, *J Cell Biol*, 216 (2017) 3387-3403.

[38] C.A. Schneider, W.S. Rasband, K.W. Eliceiri, NIH Image to ImageJ: 25 years of image analysis, *Nat Methods*, 9 (2012) 671-675.

[39] M. Ovesny, P. Krizek, J. Borkovec, Z. Svindrych, G.M. Hagen, ThunderSTORM: a comprehensive ImageJ plug-in for PALM and STORM data analysis and super-resolution imaging, *Bioinformatics*, 30 (2014) 2389-2390.

[40] S. Malkusch, M. Heilemann, Extracting quantitative information from single-molecule super-resolution imaging data with LAMA - LocAlization Microscopy Analyzer, *Sci Rep*, 6 (2016) 34486.

[41] A. Syed, Q. Zhu, E.A. Smith, Ligand binding affinity and changes in the lateral diffusion of receptor for advanced glycation endproducts (RAGE), *Biochim Biophys Acta*, 1858 (2016) 3141-3149.

[42] D. Mainali, E.A. Smith, Select cytoplasmic and membrane proteins increase the percentage of immobile integrins but do not affect the average diffusion coefficient of mobile integrins, *Anal Bioanal Chem*, 405 (2013) 8561-8568.

[43] I.F. Sbalzarini, P. Koumoutsakos, Feature point tracking and trajectory analysis for video imaging in cell biology, *J Struct Biol*, 151 (2005) 182-195.

[44] G.J. Schutz, H. Schindler, T. Schmidt, Single-molecule microscopy on model membranes reveals anomalous diffusion, *Biophys J*, 73 (1997) 1073-1080.

[45] A. Matysik, R.S. Kraut, TrackArt: the user friendly interface for single molecule tracking data analysis and simulation applied to complex diffusion in mica supported lipid bilayers, *BMC Res Notes*, 7 (2014) 274.

[46] L. Niu, J. Yu, Investigating intracellular dynamics of FtsZ cytoskeleton with photoactivation single-molecule tracking, *Biophys J*, 95 (2008) 2009-2016.

[47] T.Y. Chen, A.G. Santiago, W. Jung, L. Krzeminski, F. Yang, D.J. Martell, J.D. Helmann, P. Chen, Concentration- and chromosome-organization-dependent regulator unbinding from DNA for transcription regulation in living cells, *Nat Commun*, 6 (2015) 7445.

[48] J.C. Gebhardt, D.M. Suter, R. Roy, Z.W. Zhao, A.R. Chapman, S. Basu, T. Maniatis, X.S. Xie, Single-molecule imaging of transcription factor binding to DNA in live mammalian cells, *Nat Methods*, 10 (2013) 421-426.

[49] S. Uphoff, R. Reyes-Lamothe, F. Garza de Leon, D.J. Sherratt, A.N. Kapanidis, Single-molecule DNA repair in live bacteria, *Proc Natl Acad Sci U S A*, 110 (2013) 8063-8068.

[50] M.A. Deverall, E. Gindl, E.K. Sinner, H. Besir, J. Ruehe, M.J. Saxton, C.A. Naumann, Membrane lateral mobility obstructed by polymer-tethered lipids studied at the single molecule level, *Biophys J*, 88 (2005) 1875-1886.

[51] R. Simson, E.D. Sheets, K. Jacobson, Detection of Temporary Lateral Confinement of Membrane-Proteins Using Single-Particle Tracking Analysis, *Biophysical Journal*, 69 (1995) 989-993.

[52] S.A. Menchon, M.G. Martin, C.G. Dotti, APM_GUI: analyzing particle movement on the cell membrane and determining confinement, *Bmc Biophysics*, 5 (2012).

[53] P.J. Bosch, J.S. Kanger, V. Subramaniam, Classification of dynamical diffusion states in single molecule tracking microscopy, *Biophys J*, 107 (2014) 588-598.

[54] F. Xiong, S. Leonov, A.C. Howard, S. Xiong, B. Zhang, L. Mei, P. McNeil, S. Simon, W.C. Xiong, Receptor for advanced glycation end products (RAGE) prevents endothelial cell membrane resealing and regulates F-actin remodeling in a beta-catenin-dependent manner, *J Biol Chem*, 286 (2011) 35061-35070.

## 2.7 Figures and Tables

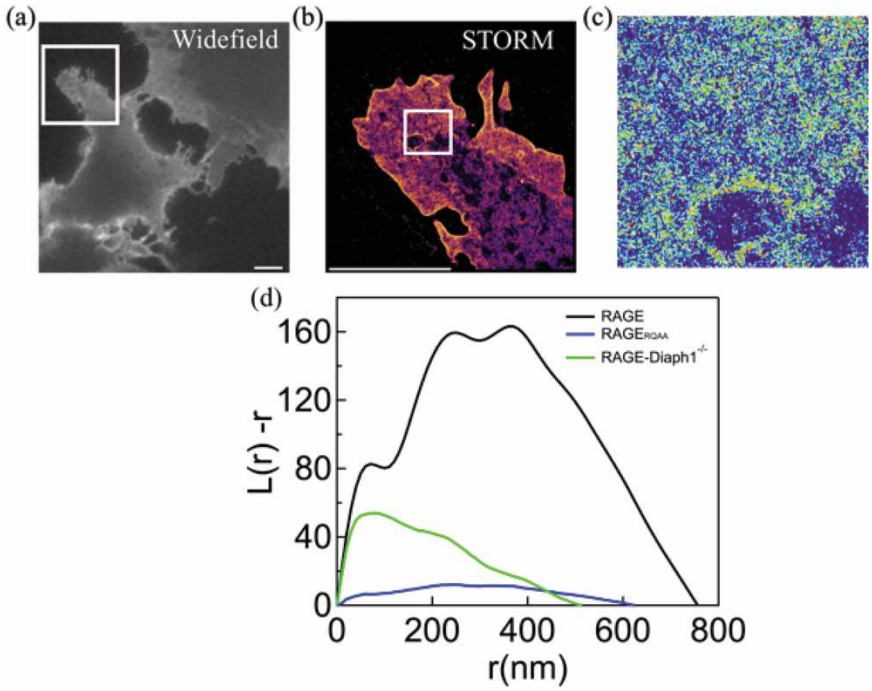


**Figure 2.1.** RAGE spatial organization in the plasma membrane of HEK 293 cells as measured by fluorescence microscopy. (a) Wide-field diffraction-limited image measured by primary anti-RAGE antibody with Alexa Fluor 647 F(ab')2-Goat anti-rabbit secondary antibody. The white box represents the region where STORM measurements were performed. The scale bar is 10 μm. (b) Reconstructed STORM image. The white box represents the region where cluster analysis was performed. Scale bar is 10 μm. (c) Heat map showing the results from cluster analysis of a (4 μm × 4 μm) region. The color indicates the degree of clustering from low (dark blue) to high (red). (d) Plots of Ripley's K-function analysis of the clustering properties of RAGE, $RAGE_{RQ/AA}$, RAGE-Diaph1$^{-/-}$ in HEK293 cells (n = 4 for each cell type). L(r)-r represents the clustering ability, and r represents the radial clustering scale.

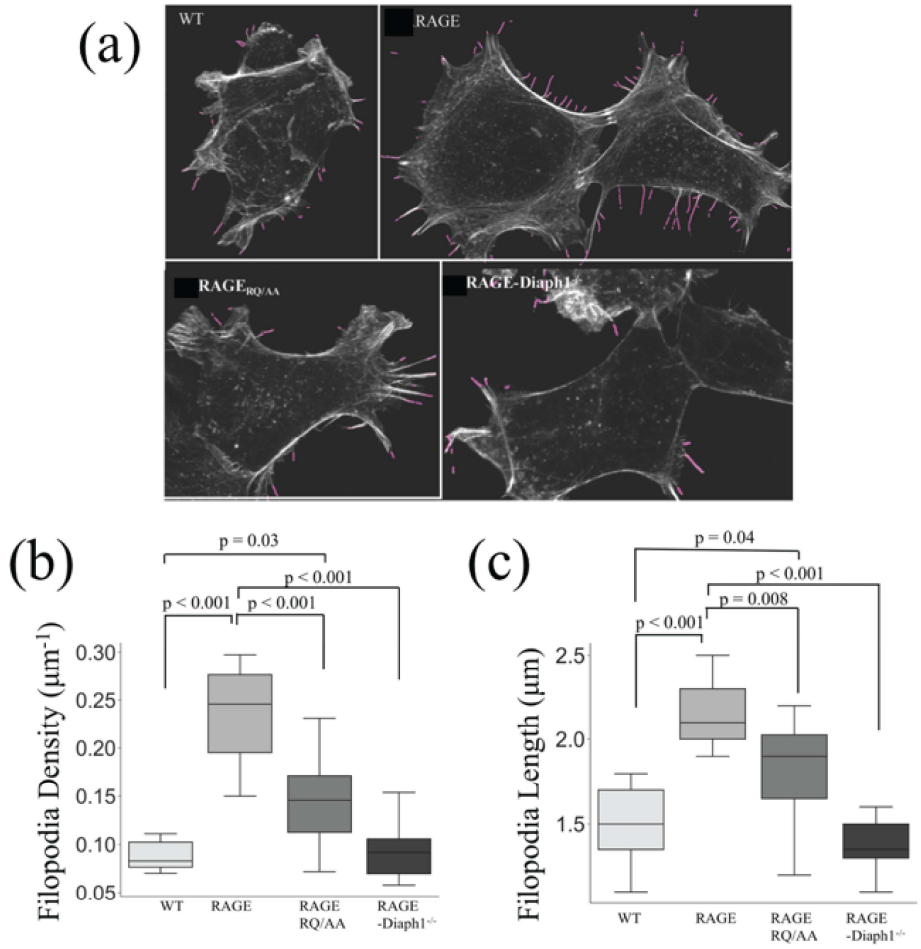


**Figure 2.2.** Filopodia density and length measured when the actin cytoskeleton is stained with Atto 647N-conjugated phalloidin in HEK 293 cells. The number of analyzed HEK293 cells are: wild-type (WT) cell line (n = 8), cells expressing RAGE (n = 10), cells expressing $RAGE_{RQ/AA}$ (n = 13), RAGE-Diaph1$^{-/-}$ cells (n = 15). (a) The filopodia detected using FiloQuant are labeled with a pink line in each image. Box plots of (b) the filopodia density and (c) filopodia length. The line inside the box represents the mean value. The box shows the twenty-fifth and seventy-fifth quartiles with the mean shown within the box. The thin line is 1.5 times the interquartile range.

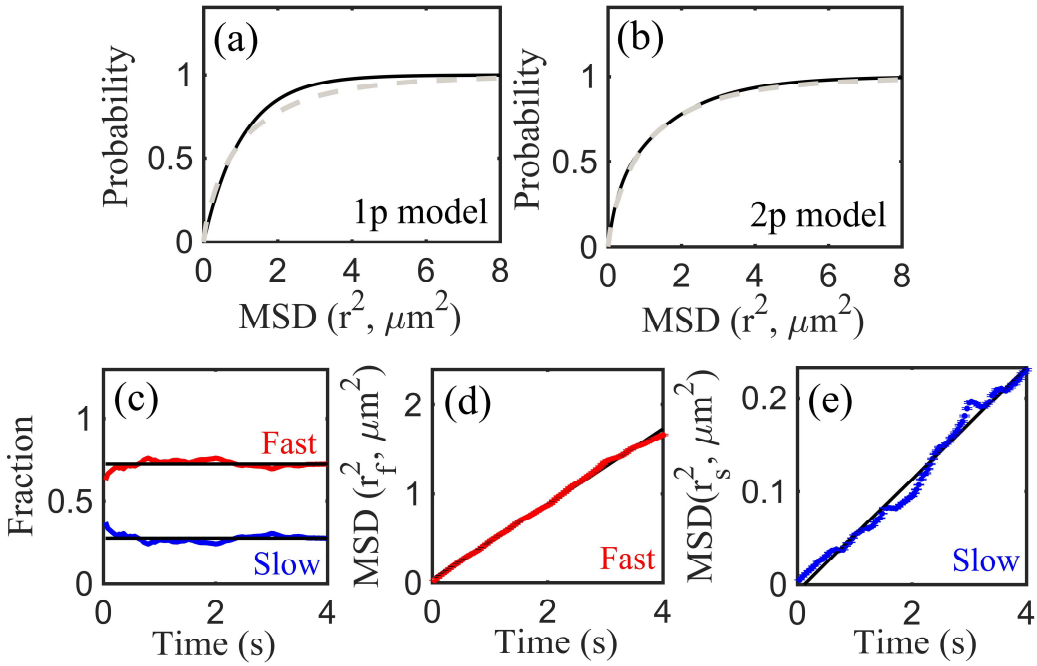


**Figure 2.3.** RAGE diffusion properties obtained from all trajectories (n = 130) measured in HEK 293 cells. The average of all trajectories' cumulative probability distribution (CPD) with a 4 sec lag time versus squared step sizes ($r^2$) are fit using (a) single population model (1p) and (b) two population model (2p). The grey dashed line represents the CPD, the solid black line represents the fit curve. (c) Fractions of the fast population and slow population calculated using the 2p model. The average MSD plots for the (d) fast and (e) slow population versus lag time. The black lines represent the fit curves.

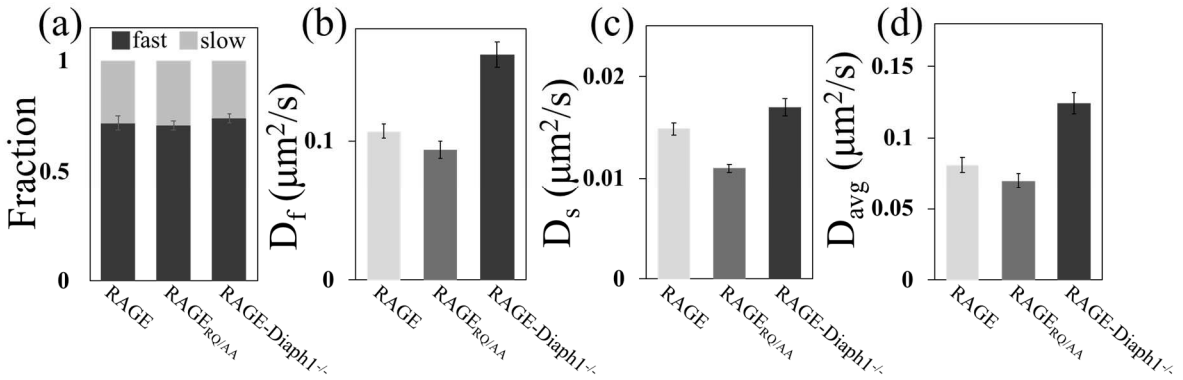


**Figure 2.4.** Average diffusion properties of RAGE (n = 145), $RAGE_{RQ/AA}$ (n = 185), RAGE-Diaph1$^{-/-}$ (n = 131) in HEK 293 cells. (a) Fraction of the total RAGE exhibiting both fast diffusion and slow diffusion, and the diffusion coefficient for (b) the fast population ($D_f$) and (c) the slow population ($D_s$) obtained from a double exponential fit to the cumulative probability distributions. (d) Average diffusion coefficient for the sum of both $D_f$ and $D_s$ multiplied by their individual fraction. The error bars represent the standard error in the fit.

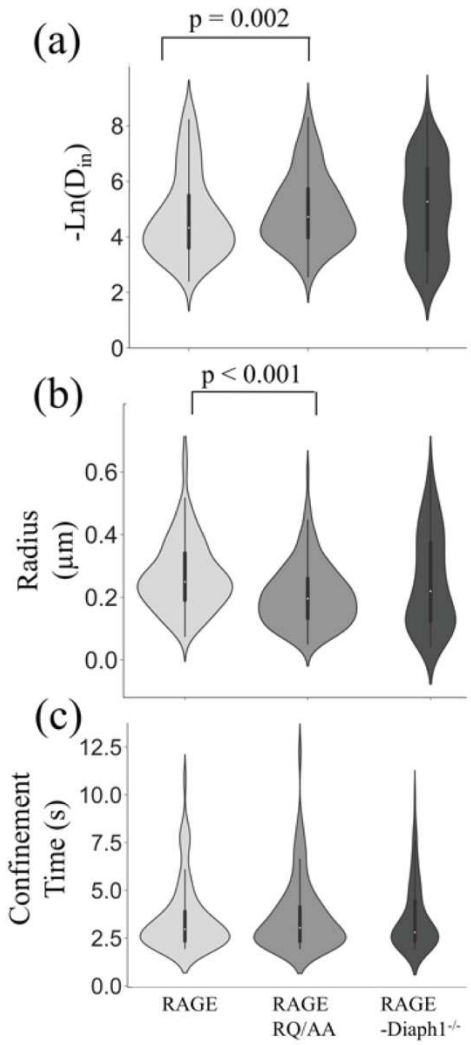


**Figure 2.5**. Analysis of all the trajectories exhibiting confined motion in HEK 293 cells. The number of analyzed confined domains are RAGE (n = 140), $RAGE_{RQ/AA}$ (n = 182), RAGE-Diaph1$^{-/-}$ (n = 91). Violin plot of the (a) negative natural log of the diffusion coefficients within confined domains, (b) size of confined domains, and (c) duration of time in confined domains. The width of the violin plot represents the data distribution. Overlapping each violin plot is a box plot showing the mean (white dot) of all values within the data set. The solid line shows the twenty-fifth and seventy-fifth quartiles. The thin line is 1.5 times the interquartile range. p-values were obtained from the Mann-Whitney test (non-parametric distribution).

## 2.8 Supporting Information

### DNA construction

The expression vector for RAGE labeled with a hemagglutinin (HA) tag (pcDNA3.HARAGE) has been previously described [1]. Briefly, the HA tag (amino acid sequence YPYDVPDYA) was inserted into the N-terminal of RAGE after the signal sequence of a previously developed pcDNA3.RAGE vector [1] using sense primer 5'-TACCCGTACGACGTGCCGGACTACGCCATCACAGCCCGGATTGGC-3' and anti-sense primer 5'-GGCGTAGTCCGGCACGTCGTAGTTTTGAGCACCTACTACTGCCC-3'. The plasmid for expressing RAGE with a R5A/Q6A cytoplasmic domain mutation (pcDNA3.HARAGE$_{RQ/AA}$) was generated by site-directed point mutagenesis using sense primer 5'-AGGGCAGCACGCCGAGGAGAGGAGAGGAAG-3' and anti-sense primer 5'-ACGCTCCTCCTCTTCCTCCTGGTTTTCTGG-3'. After PCR-amplification and Dipn1 enzyme digestion, a Gibson assembly master kit (New England Biolabs Inc.) was used to ligate all the fragments. All plasmids contained the desired sequences as confirmed by DNA sequence analysis. The resulting RAGE amino acid sequences in the transmembrane domain and intracellular domain for each of these plasmids are shown in Figure S2.2a.

### Cell culture, transfection and CRISPR/Cas9

HEK293 cells from the American Type Culture Collection (ATCC, CRL-1573) were maintained in Dulbecco's modified Eagle's medium (DMEM) (Sigma Aldrich) supplemented with 10% fetal bovine serum, 1% penicillin-streptomycin at 37 °C and 5% $CO_2$ in a humidified atmosphere. HEK293 cells were transfected with purified recombinant plasmid using Lipofectamine 3000 (Invitrogen$^{TM}$). For the generation of stable cell lines expressing RAGE or RAGE$_{RQ/AA}$, 800 µg/mL geneticin G418 (Santa Cruz Biotechnology) was used to initiate selectin of antibiotic-resistant cells. For the maintenance of stably

transfected cell lines, the concentration of G418 was decreased to 400 µg/mL. Protein expression was confirmed by Western blot analysis (Figure S2.2b and S2.2c). All the cell lines expressing full-length RAGE exhibit an expected band at 55 kDa. Transgenic RAGE expression is higher than measured for wild-type cells without transgenic RAGE expression.

To establish RAGE-Diaph1$^{-/-}$ HEK293 cells lacking the expression of Diaph1, pSpCas9-Diaph1-sgRNA(GenScript) (sgRNA sequence: TGTTGTTGAGAGACACACGA) was transfected into RAGE cells using Lipofectamine 3000. Cells were selected with 0.4 µg/mL puromycin. To maintain the RAGE-Diaph1$^{-/-}$ HEK293 cell line, 0.2 µg/mL puromycin and 200 µg/mL G418 were used. There is a 7-fold reduction in Diaph1 expression (Figure S2.2b), and a 20-fold reduction in Diaph1 mRNA in RAGE-Diaph1$^{-/-}$ cells compared to the RAGE cell line (Figure S2.2c).

**Western blotting and RT-qPCR**

Wild-type HEK293 cells and cells expressing RAGE, RAGE$_{RQ/AA}$, or RAGE-Diaph1$^{-/-}$ were subcultured into a 6-well plate for 48 hrs. After the cells were rinsed with phosphate buffered saline (PBS) three times, cells were lysed by adding lysis buffer (50 mM Tris pH 7.5, 120 mM NaCl, 0.5% NP40) containing 1× Halt protease inhibitor cocktail (Invitrogen™). The protein concentration of cell lysates were quantified using a protein BCA assay kit (Invitrogen™). 15 µg protein was electrophoresed using a NuPAGE Novex 4-12% Bis-Tris protein gel (Novex™) followed by electro blotting to PVDF membrane (Invitrolon™, 0.45 µm pore size) for 4 hrs. The membrane was blocked with 5% bovine serum albumin for 1 hr at 37 °C, and then RAGE and Diaph1 expression were probed using anti-RAGE rabbit (17H19L10, Invitrogen™), anti-Diaph1 mouse (sc-373807, Santa Cruz Biotechnology), anti-vinculin goat (sc-7649, Santa Cruz Biotechnology), and anti-Actin

rabbit (sc-1616-R, Santa Cruz Biotechnology). The labeled secondary antibodies were Alexa Fluor 647 goat anti-rabbit (Life technologies), Alexa Fluor 488 donkey anti-goat (Life technologies), and Alex Fluor 488 goat anti-mouse (Life technologies). The fluorescence intensity was measured with a Typhoon FLA 95000 variable mode laser imager (GE Healthcare). The actin and vinculin protein bands were used as loading controls in the Western blot experiments.

mRNA was isolated using a Dynabeads mRNA DIRECT kit (Invitrogen$^{TM}$) following the manufacturer's instruction. For reverse transcription, 500 ng mRNA was converted to complementary DNA using a High Capacity RNA-to-cDNA Kit (Applied Biosystems). Quantitative real-time PCR analysis was performed using Applied Biosystems TaqMan Gene Expression assays (ACTB as housekeeping gene: Hs01060665_g1; Diaph1: Hs00946567_g1; AGER: Hs00542592_g1) on a Roche Light Cycler 480 system (Roche Applied Science). The comparative cycle threshold (CT) was used to determine relative mRNA expression of the genes as normalized by a ACTB housekeeping gene. The level of gene expression was determined by the $2^{-\Delta\Delta CT}$ method [2].

**Figures and tables for supporting information for Chapter 2**

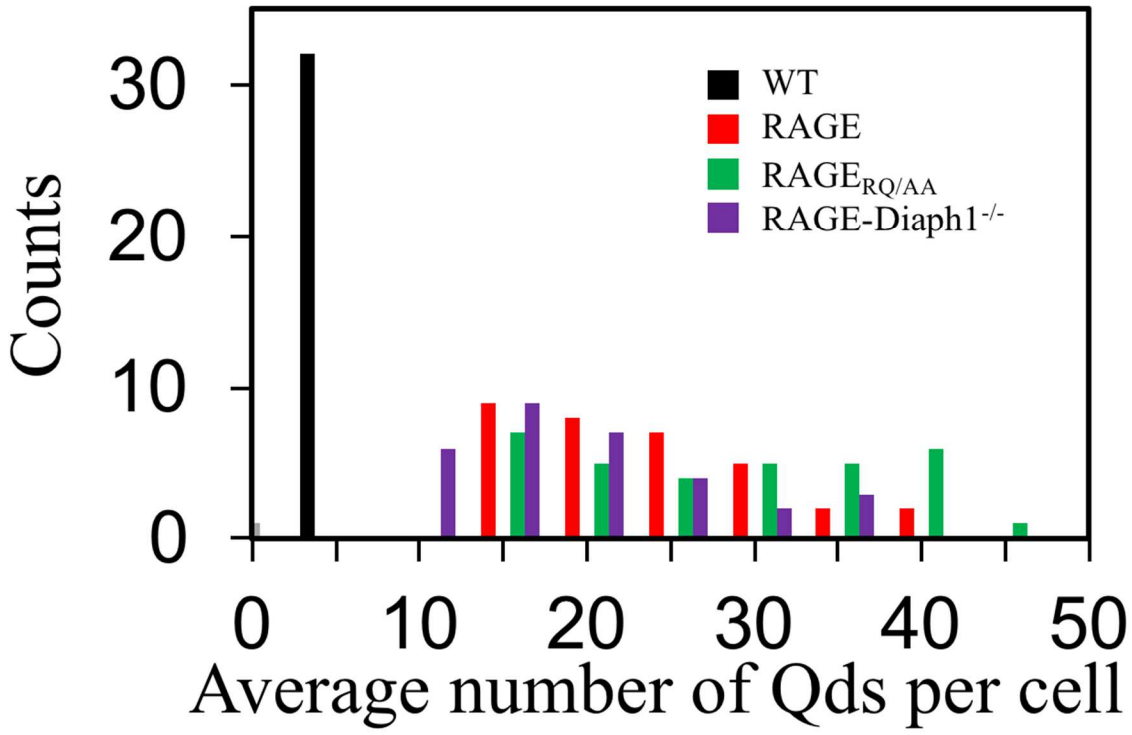


**Figure S2.1.** Quantification of the average number of quantum dots (Qds) in HEK 293 cells (n = 35). Histograms of the average number of Qds per cell for wild type cells (WT, wherein no RAGE is detected by Western blot) and RAGE expressing cells: $RAGE_{RQ/AA}$, and RAGE-Diaph1$^{-/-}$ with a reduced expression of Diaph1 (Bin size = 5).

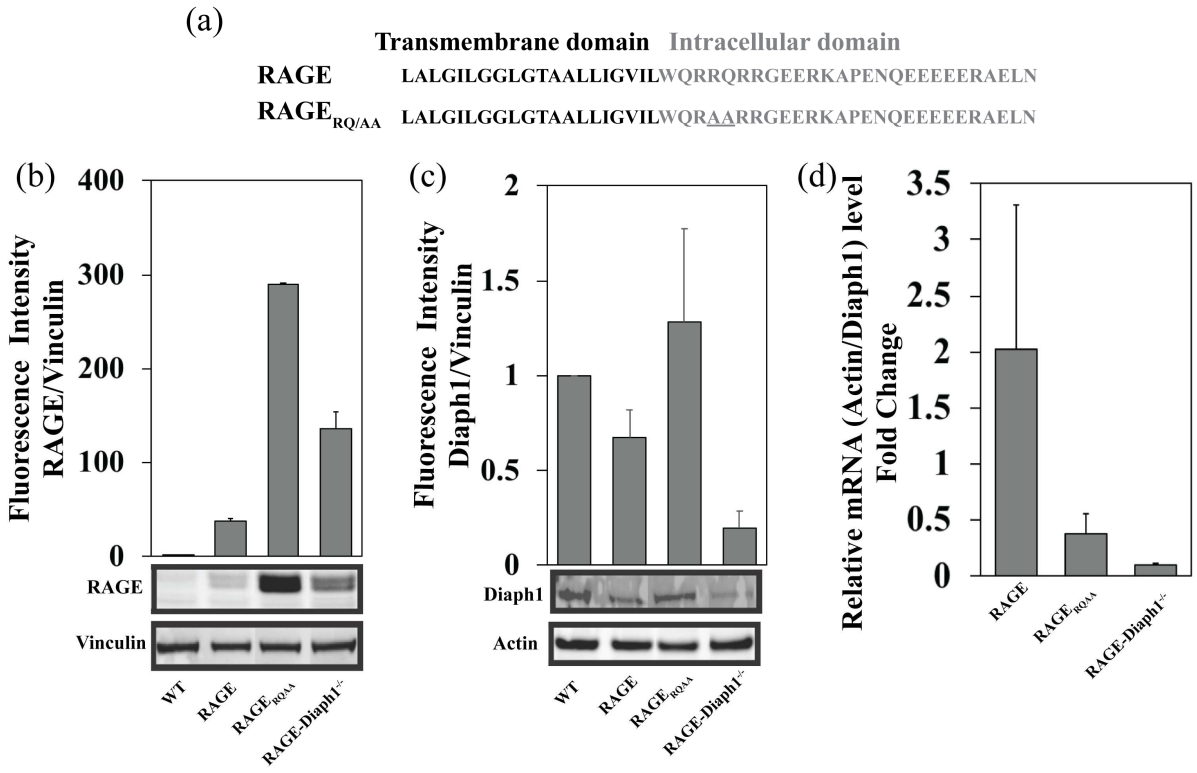


**Figure S2.2.** Quantification of protein and mRNA expression in HEK 293 cell lines. (a) Amino acid sequence of RAGE and $RAGE_{RQ/AA}$ in the transmembrane and intracellular domains. Western blot analysis of (b) RAGE protein expression and (c) Diaph1 protein expression. Diaph1 expression is not eliminated in the RAGE-Diaph1$^{-/-}$ cell line, which may be the result of incomplete selection of transfected cells. Fluorescence images of the PVDF membrane were detected with primary RAGE, vinculin, Diaph1, actin antibody and Alexa Fluor labeled secondary antibody. Average fluorescence intensities (n = 3) of the RAGE and Diaph1 bands were divided by the vinculin and actin bands, respectively. The Wild type (WT) HEK293 cell line was used to normalized the fluorescence intensity of the other cell lines. Since Western blotting does not provide an absolute concentration, it is unclear that any differences in RAGE expression measured by Western blotting have a significance in the membrane environment. (d) Average (n = 3) change in the mRNA level of Diaph1 determined by RT-qPCR. The relative gene expression was normalized by beta actin (ACBT) as the internal control, and analyzed using the $2^{-\Delta\Delta CT}$ method. ** represents p-value < 0.01; *** represent p-value < 0.001.

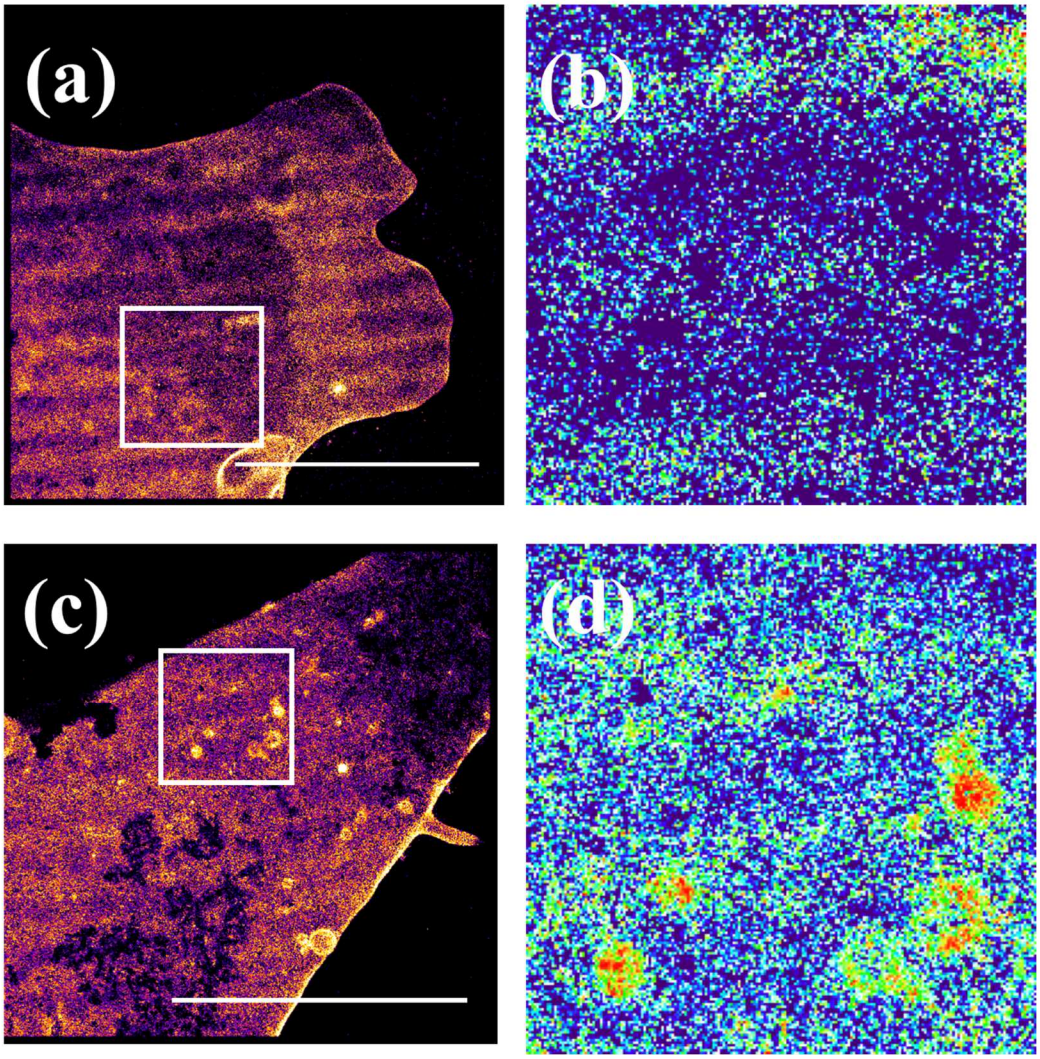


**Figure S2.3.** Reconstructed storm images showing the spatial organization in the plasma membrane of (a) $RAGE_{RQ/AA}$, and (c) RAGE-Diaph1$^{-/-}$. The 4 μm × 4 μm white box represents the region where cluster analysis was performed, and the results are shown in the heat map to the right of each image in (b) and (d). The color indicates the degree of clustering from low (dark blue) to high (red). The background (possibly from cellular autofluorescence) varies from cell to cell (i.e., image to image). Scale bar is 10 μm.

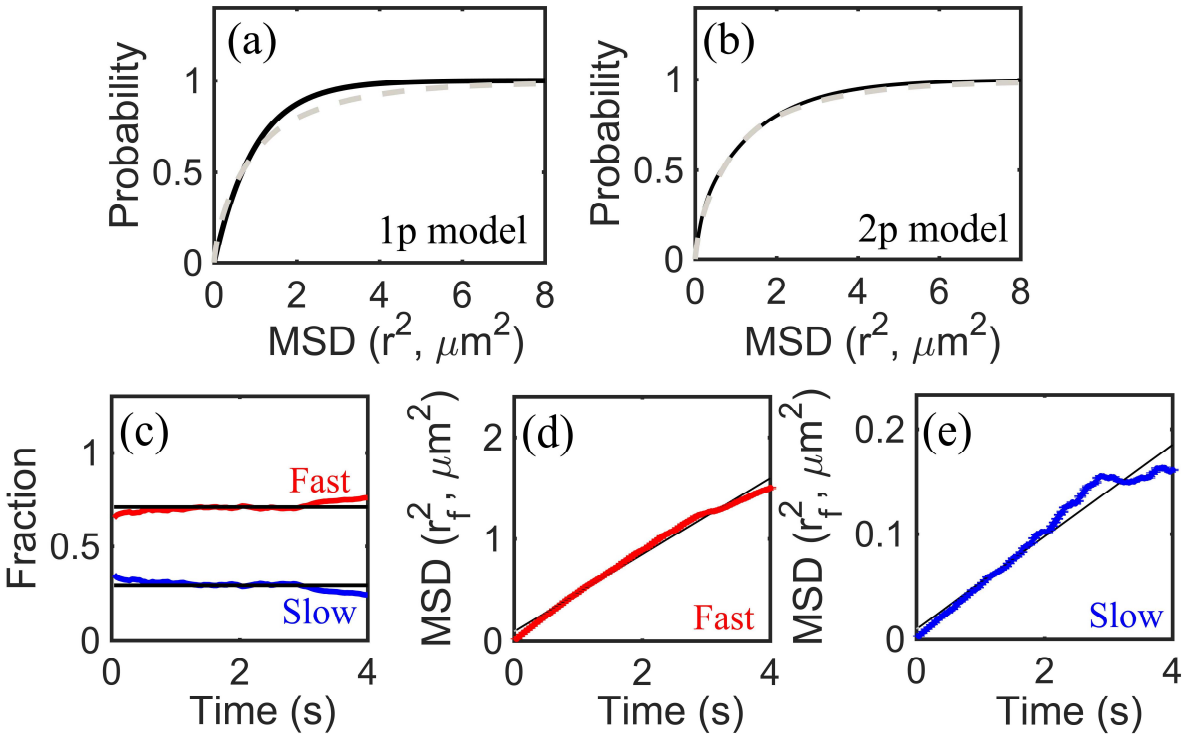


**Figure S2.4.** Analysis of $RAGE_{RQ/AA}$ diffusion properties obtained from all trajectories (n = 180) measured in HEK 293 cells. The average cumulative probability distribution (CPD, gray dashed line) of all trajectories with a 4 sec lag time versus squared step size (i.e., $r^2$). The fit using (a) a single population (i.e., 1p) and (b) two populations (i.e., 2p) models is shown as the solid black line. (c) Fractions of the fast (red) and slow (blue) populations calculated using the 2p model. The average MSD versus lag time plots for the (d) fast and (e) slow population. The black line in (d) and (e) represents the fit to the data, which is used to calculate the diffusion coefficient for each population.

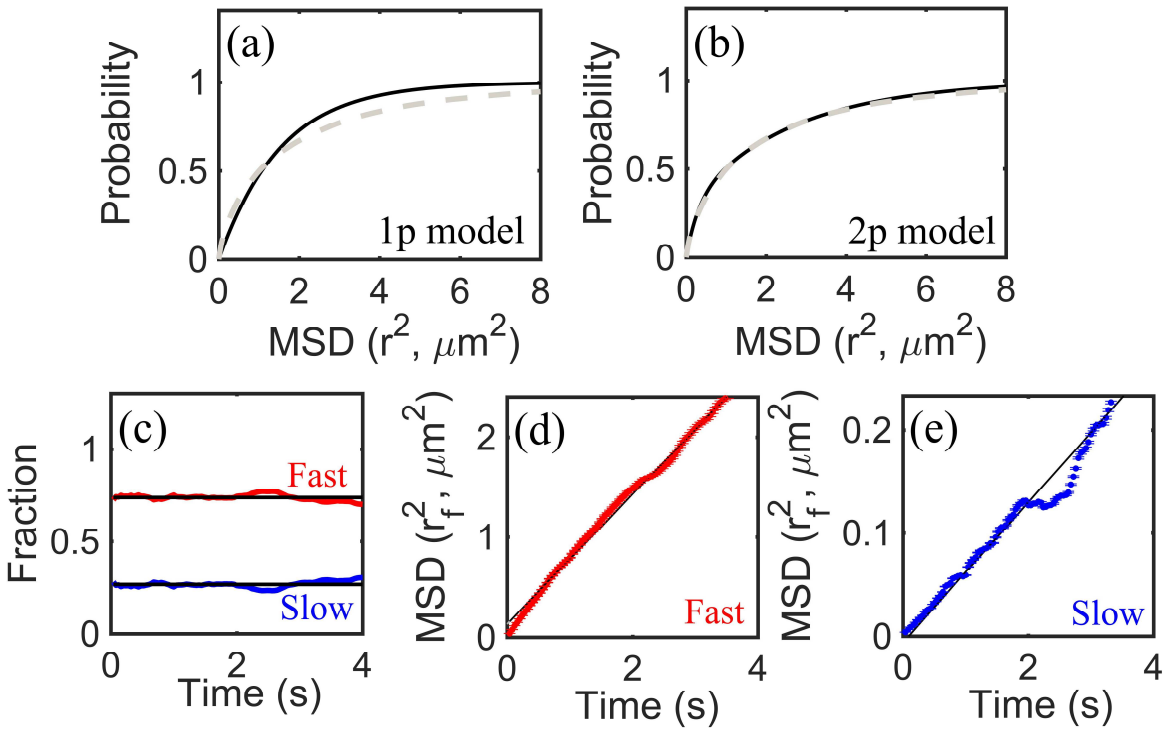


**Figure S2.5.** Analysis of RAGE-Diaph1-/- diffusion properties obtained from all trajectories (n = 131) measured in HEK293 cells. The average cumulative probability distribution (CPD, gray dashed line) of all trajectories with a 4 sec lag time versus squared step size (i.e., r2). The fit using (a) a single population (i.e., 1p) and (b) two populations (i.e., 2p) models is shown as the solid black line. (c) Fractions of the fast (red) and slow (blue) populations calculated using the 2p model. The average MSD versus lag time plots for the (d) fast and (e) slow population. The black line in (d) and (e) represents the fit to the data, which is used to calculate the diffusion coefficient for each population.

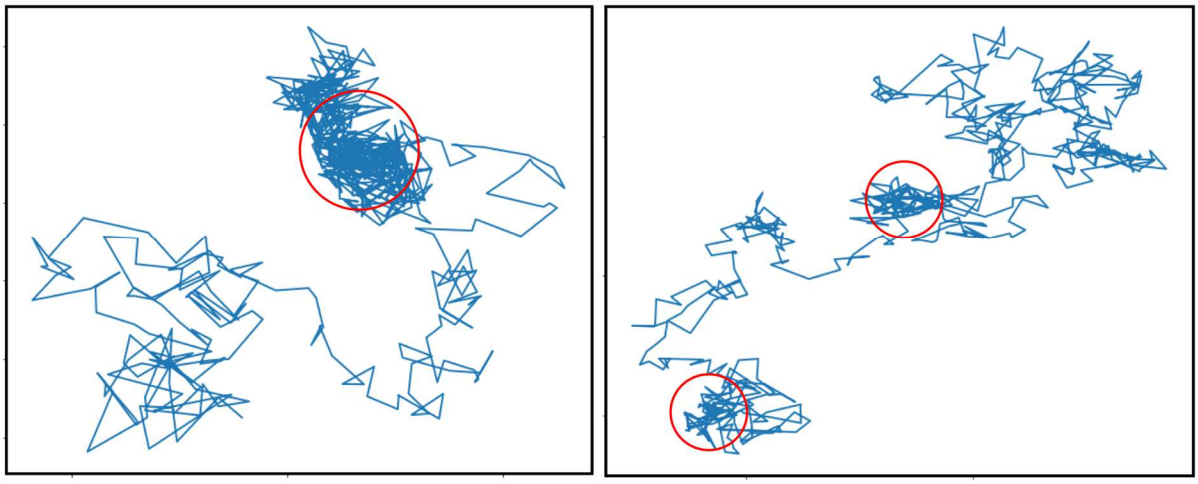

**Figure S2.6.** Two examples of RAGE single particle trajectories that exhibit transient events that represent diffusion within confined domains. All trajectories (blue line) were categorized as either Brownian motion or confined (i.e., non-random) motion based on the probability (L) of staying within a region of radius R (represented by the red circle). If the critical confinement index (Lc ) is greater than 3.16 and critical confinement time (tc) is greater than 1.95, values obtained from simulated Brownian trajectories for a range of diffusion coefficients as previously described [3], a trajectory is categorized as confined motion.

**References for supporting information for Chapter 2**

[1] A. Syed, Q. Zhu, E.A. Smith, Ligand binding affinity and changes in the lateral diffusion of receptor for advanced glycation endproducts (RAGE), *Biochim Biophys Acta*, 1858 (2016) 3141-3149.

[2] T.D. Schmittgen, K.J. Livak, Analyzing real-time PCR data by the comparative C-T method, *Nat Protoc*, 3 (2008) 1101-1108.

[3] S.A. Menchon, M.G. Martin, C.G. Dotti, APM_GUI: analyzing particle movement on the cell membrane and determining confinement, *Bmc Biophysics*, 5 (2012).

# CHAPTER 3. LIGAND BINDING AFFINITY AND CHANGES IN THE LATERAL DIFFUSION OF RECEPTOR FOR ADVANCED GLYCATION ENDPRODUCTS (RAGE)

Modified from a publication on the *BBA Biomembranes*

Aleem Syed[1], Qiaochu Zhu[1] and Emily A. Smith*

Department of Chemistry, Iowa State University, 1605 Gilman Hall, Ames, IA 50010

[1] These authors have contributed equally to the work.

## 3.1 Abstract

The effect of ligand on the lateral diffusion of receptor for advanced glycation endproducts (RAGE), a receptor involved in numerous pathological conditions, remains unknown. Single particle tracking experiments that use quantum dots specifically bound to hemagglutinin (HA)-tagged RAGE (HA-RAGE) are reported to elucidate the effect of ligand binding on HA-RAGE diffusion in GM07373 cell membranes. The ligand used in these studies is methylglyoxal modified-bovine serum albumin (MGO-BSA) containing advanced glycation end product modifications. The binding affinity between soluble RAGE and MGO-BSA increases by 1.8 to 9.7-fold as the percent primary amine modification increases from 24 to 74% and with increasing negative charge on the MGO-BSA. Ligand incubation affects the HA-RAGE diffusion coefficient, the radius of confined domains of diffusion, and duration in confined domains of diffusion. There is, however, no correlation between MGO-BSA ligand binding affinity and the extent of the changes in HA-RAGE lateral diffusion. The ligand induced changes to HA-RAGE lateral diffusion do not occur when cholesterol is depleted from the cell membrane, indicating the mechanism for ligand-induced changes to

HA-RAGE diffusion is cholesterol dependent. The results presented here serve as a first step in unraveling how ligand influences RAGE lateral diffusion.

### 3.2 Introduction

The receptor for advanced glycation endproducts (RAGE) is a transmembrane receptor that is involved in several pathological disorders [1-3]. It is a multi-ligand pattern-recognition receptor with a diverse array of chemically distinct ligands [4]. Although ligand induced RAGE signaling has been studied extensively in various pathological states, knowledge of the molecular diffusion of RAGE in the cell membrane is generally unknown. The lateral diffusion of membrane proteins plays a role in how receptors interface with other membrane proteins, extracellular ligands, and intracellular proteins, and more generally, how receptors function. The goal of the work reported herein is to understand the effect of ligand incubation on the lateral diffusion and signaling of RAGE in GM07373 bovine artery endothelial cell membranes.

RAGE consists of one variable (V) and two constant (C1 and C2) domains in the extracellular region, a single transmembrane domain and a short cytoplasmic tail. The RAGE extracellular ligand binding domains belong to the immunoglobulin superfamily. RAGE interacts with several ligands including advanced glycation endproducts (AGE), members of the S100/calgranulins family of proteins and amyloid-beta peptides [5-7]. AGE include non-enzymatic modifications of surface amino acid residues lysine, arginine and cysteine, which may lead to protein cross linking. The resulting AGE-modified proteins have a net increase in negative surface charge [8]. Although RAGE ligands are structurally different, all ligands are reported to contain negatively charged regions that are important for binding. Structural analysis of the RAGE extracellular domain with X-ray crystallography and nuclear magnetic

resonance spectroscopy corroborates the notion that negatively charged ligands interact with positively charged surfaces of the V and C1-type RAGE ectodomains [9, 10]. The binding between RAGE and its ligands has been measured by several techniques including surface plasmon resonance (SPR) and ELISA. For example, the dissociation constants measured by SPR with human RAGE were 360 nM and 1.3 μM for glceraldehyde-derived and glycoladehyde-derived AGE, respectively [11]. A SPR analysis of the S100B-soluble RAGE interaction revealed a moderate affinity with an 8.3 μM dissociation constant [12]. Methylglyoxal modified-bovine serum albumin (MGO-BSA, a model AGE similar to the one used herein), binds to the V domain of RAGE with an 800 nM dissociation constant as measured by ELISA [13].

We have recently reported properties of RAGE lateral diffusion as measured by fluorescence recovery photobleaching (FRAP) [14]. The lateral diffusion of RAGE and RAGE-dependent signaling were found to be connected to the dynamics of the actin cytoskeleton. In a FRAP experiment, the measured diffusion parameters represent an ensemble average of numerous receptors. However, receptor lateral diffusion is generally not synchronized across each receptor, and the heterogeneity of all possible diffusion behaviors is not measured by FRAP. For this purpose, it is necessary to probe the diffusion one receptor at a time. One such approach is single particle tracking (SPT), where the receptor is exogenously labeled with a fluorophore and the diffusion of labeled receptor is extracted by following the trajectory of the label [15]. SPT has been used to study the diffusion of a variety of receptors such as G protein-coupled receptors, epidermal growth factor receptor, and homomeric α3-containing glycine receptor [16-18]. For SPT, it is imperative that the signal from the fluorophore be bright and photostable to facilitate fast acquisition times over

long durations. Inorganic quantum dots (QDs) satisfy the requirements, and the size of the QD can be of similar magnitude to many receptors. Labeling specificity to the desired receptor is achieved by modifying the QD surface with a ligand or another similar strategy [19]. A recent review article summarizes the use of SPT to measure receptor diffusion [20].

Given the importance of electrostatic interactions in RAGE binding to ligand, increasing the negative charge of the ligand may influence binding and the functional consequences of binding to RAGE; this may include influencing the lateral diffusion of RAGE. To test this hypothesis, MGO-BSA with different extents of primary amine modification are prepared. The extent of modification is characterized by measuring free primary amine content and zeta potentials. Ligand binding between MGO-BSA and soluble RAGE (sRAGE, containing the RAGE extracellular domains V, C1 and C2) is measured *in vitro* using SPR. The effect of ligand on the lateral diffusion of HA-RAGE is measured with single particle tracking (SPT). The role of cholesterol in ligand-induced changes to HA-RAGE lateral diffusion is measured by depleting cellular cholesterol concentrations with methyl-β-cyclodextrin. Finally, ERK phosphorylation is studied in cells to identify possible correlations in HA-RAGE lateral diffusion, signaling, and ligand binding properties.

## 3.3 Materials and Methods

### Cell culture, protein expression and Western blotting

All microscopy and molecular biology experiments were performed using bovine artery GM07373 endothelial cells (Coriell Institute Biorepositories, Camden, NJ) maintained according to the procedure described previously [14]. GM07373 cells were transfected with purified recombinant plasmid using Lipofectamine 2000 and the manufacturer's instructions (Life Technology). Transfected GM07373 cells were selected using Geneticin sulfate (Santa

Cruz Biotechnology, Inc., Santa Cruz, CA). The transfected cells were established to express HA-RAGE protein stably before microscopy or molecular biology experiments. Details of the HA-RAGE expression plasmid, soluble RAGE expression and purification and Western blotting experiments are provided in the supplementary material.

**Preparation and characterization of methylglyoxal (MGO) modified-bovine serum albumin (BSA)**

BSA was modified with different concentrations of MGO to generate various MGO-BSA. 10 mM, 40 mM, 60 mM, 80 mM and 100 mM MGO was incubated with 50 mg/mL BSA in 0.1 M phosphate buffered saline (PBS) pH 7.4 at 37 °C for five days. On the fifth day, unreacted MGO was removed by dialysis in 0.1 M PBS. The ortho-phthaldialdehyde assay was performed to evaluate the extent of modification *via* quantifying the free primary amine content of BSA [21]. The fluorescence intensity was measured with a microplate reader (Synergy 2 Multi-Mode Reader, BioTek) at excitation and emission wavelengths of 340 nm and 435 nm, respectively. The resulting fluorescence intensities were translated into a percent modification using the signal measured from unmodified BSA (without MGO incubation) as a control.

**Zeta potential measurement**

The zeta potential and protein mobility of the prepared MGO-BSA were obtained using a Zetasizer Nano ZS (Malvern Instruments, Ltd) with laser Doppler velocimetry. MGO-BSA and BSA control were diluted five times in PBS solution at pH=7.4. Three replicates were measured for each sample at 25 °C and 200 continuous runs.

**Surface plasmon resonance (SPR)**

The binding affinity between MGO-BSA and sRAGE was measured using a home-built SPR instrument. The MGO-BSA was immobilized by physisorption on a 50-nm thick

gold film. 100 nM sRAGE in HEPES buffer (pH=7.5) was pumped into a flow cell at the flow rate of 0.8 ml/min for one minute, and then the SPR response was monitored for 20 min. After the 20 min association step, the HEPES buffer was flowed for 1 min at the flow rate of 0.8 ml/min, and then the response during the dissociation step was monitored for an additional 20 min. The kinetic parameters for the MGO-BSA/sRAGE interaction were obtained from the resulting sensorgrams as previously reported using the equations provided in the supplementary material [22].

**Quantum dot conjugation and sample preparation for single particle tracking (SPT)**

Quantum dots (QDs, ThermoFisher Scientific) conjugated with streptavidin with an approximate diameter of 15 to 20 nm were used as a fluorescent probe in SPT experiments. 5 µL of streptavidin coated QDs in 1 µM borate buffer were added to 21 µL of monoclonal HA-epitope tag antibody conjugated with biotin (ThermoFisher Scientific) in 74 µL of PBS buffer (pH=7.4) and incubated for 2 hours at room temperature. The resulting anti-HA labeled QDs (AHA-QDs) were stored in the refrigerator until use.

Cells were sub cultured onto 8-well Nunc™ Lab-Tek™ chambered glass slide for 24 hours. On the next day, spread cells were incubated with 3% (W/V) BSA in DMEM (BSA-DMEM) medium overnight before imaging experiments to minimize the nonspecific binding. Cells were either used without further treatment or treated with specific MGO-BSA (5 mg/mL in BSA-DMEM) for 1 h. In the case of sequential cholesterol depletion, cells were further treated with MβCD (5 mM in BSA-DMEM) before labeling with AHA-QDs. For SPT experiments, AHA-QDs were sonicated for 2 h to avoid aggregation of the QDs. The AHA-QDs were diluted to 100 pM in the imaging medium containing 0.1% (W/V) BSA. The low AHA-QD concentration reduces the possibility that two or more QDs are colocalized within the diffraction volume. Cells were incubated with the AHA-QDs for 15 minutes at 37

ºC in the incubator. Cells were then rinsed with imaging medium five times before mounting the sample onto the microscope.

The SPT experiments were performed using a Nikon Eclipse TE2000U microscope (Melville, NY, USA) operating in wide-field, epi-fluorescence mode with a 100× objective and mercury lamp illumination. Filter sets for excitation (425/45 nm) and emission (605/20 nm) were obtained from Omega Optical (XF304-1, Brattleboro, VT, USA). The microscope was housed inside a physiological chamber. All imaging experiments were performed at 36 ± 2 ºC. Fluorescence images were collected using a PhotonMAX 512 EMCCD camera (Princeton Instrument, Trenton, NJ, USA) with a 40 ms camera exposure time and a full-chip (512×512 pixels) field of view for a total of 40 s.

**QD binding specificity, localization, and tracking**

The AHA-QD binding specificity was measured using two cell lines: GM07373 cells that do not express HA-RAGE and GM07373 cells that express HA-RAGE. Nonspecific binding was reported as the average number of AHA-QDs in cells lacking HA-RAGE divided by the average number in cells expressing HA-RAGE. The ImageJ particle tracker 2D/3D plug-in implementing the algorithm developed by Sbalzarini and Koumoutsakos was used for detecting QDs, localization, and tracking [23, 24]. The intrinsic blinking property of the QDs was used to identify single particles and the extracted single particle trajectories that were at least 8 s in duration (i.e., in between blinking events) were further analyzed.

**SPT data analysis**

Extracted single particle trajectories were analyzed using APM_GUI (Analyzing Particle Movement with Graphical User Interface), which is a MATLAB-implemented application based on an established algorithm reported by Simson and co-workers [25, 26]. Diffusion coefficients measured for AHA-QDs on GM07373 cells were used as a threshold

to select mobile trajectories to account for the non-specific binding. All mobile trajectories were classified either as confined or as non-confined (Brownian) trajectories based on the probability of particle motion being Brownian in a given region. The probability level or the confinement index (L) was calculated for each trajectory to highlight the regions of confined behavior as described previously [26]. The simulated Brownian trajectories for a range of diffusion coefficients were used to estimate the critical confinement index ($L_c$) and critical confinement time ($t_c$). These two parameters were used as a threshold to separate Brownian motion from confined motion. In general, the greater the value of L, the greater the tendency for a trajectory to exhibit confined motion. For a given trajectory, a confined diffusion region is defined by the regions where L increases above $L_c$ for a duration of time longer than $t_c$. Based on the simulation data for Brownian trajectories, the trajectories with $L > 3.16$ for a duration $t_c > 1.95$ s had a 99.93 % likelihood to be in confined motion. For a trajectory classified as confined, the size of the confinement region, the duration of the confinement time, and the diffusion coefficients inside the confined zones and outside the confined regions were further analyzed. The plot of mean square displacement (MSD) vs time was used to calculate the characteristic diffusion coefficient of a given region [25]. RAGE is reported to oligomerize on the cell surface in the presence of ligand [27-29]. It is not possible to know if a tracked receptor is a monomer or part of an oligomer based on its diffusion coefficient. This is because the diffusion coefficient has a logarithmic dependence on inverse radius, and is thus not particularly sensitive to clustering.

## 3.4 Results and Discussion

### Characterization of MGO-BSA ligand and its interactions with RAGE

Five MGO-BSA samples were prepared by incubating BSA with 10 to 100 mM MGO. Two of the possible amino acid modifications that occur after MGO incubation are shown in Figure S3.1. The extent of primary amine modification as measured by the ortho-phthaldialdehyde assay increases linearly ($R^2 = 0.98$) when increasing concentrations of MGO are used for the *in vitro* modification of BSA (Figure 3.1A). The percent primary amine modification ranges from 24 to 74% compared to control BSA that is not incubated with MGO. BSA that has not been incubated with MGO has a net positive surface charge, but all MGO-BSA samples have a net negative surface charge that increases as the MGO concentration used for the modification of BSA increases (Figure 3.1B).

RAGE ligands mainly bind to the extracellular V and C1 domains [9, 10], so a soluble variant for RAGE (sRAGE) is commonly used as an antigen for binding affinity studies. Surface plasmon resonance measurements of the dissociation constant ($K_d$) between each MGO-BSA sample and sRAGE are shown in Figure S3.2. The $K_d$ values obtained from the SPR curves are shown in Figure 3.1C. With increasing percent primary amine modification, the affinity of MGO-BSA for sRAGE increases (i.e., the solution concentration of MGO-BSA required to occupy half of the available binding sites on sRAGE decreases). These affinities are of the same order of magnitude as previously reported for similar RAGE ligands [13]. Combining the results of the affinity and MGO-BSA surface charge measurements, the affinity between sRAGE and MGO-BSA is linearly dependent ($R^2 = 0.94$) on the net MGO-BSA negative surface charge, which is consistent with an interaction to a positively charged binding pocket on the V-domain of sRAGE.

**Extracellular HA epitope tag enables the specific labeling of QDs to RAGE**

Single particle tracking experiments require the specific binding between a nanoparticle and a receptor. In these studies the nanoparticles are fluorescent quantum dots (QDs). A ligand can be directly coated on the surface of the QDs [30, 31], however, up to 88% nonspecific binding is observed when ligand (AGE or S100A8/A9)-coated QDs are incubated with cells that do not express RAGE (data not shown). A possible reason for the observed nonspecific binding may be due to the affinity of RAGE ligands for other membrane proteins [8]. As an alternative specific labeling route, the 9 amino acid (YPYDVPDYA) hemagglutinin (HA) tag was added to the RAGE extracellular domain at a position three amino acids away from the N-terminus of the signal peptide. The cellular signaling in HA-RAGE is similar to RAGE lacking the HA tag as measured by phosphorylation of ERK (p-ERK). There is a two-fold increase in p-ERK in GM07373 cells expressing HA-RAGE compared to GM07373 cells that do not express detectable amounts of RAGE (Figure S3.3). This increase is consistent with the two-fold increase in p-ERK in GM07373 cells expressing RAGE lacking the HA tag, as reported previously [14]. In addition, a control experiment showed no change in p-ERK when HA-RAGE expressing cells were first exposed to HA antibody, to check for a blocked ligand binding site, followed by incubation with MGO-BSA with 41% primary amine modification (Figure S3.4).

Anti-HA-coated QDs (AHA-QDs) are generated by incubating streptavidin-coated QDs with biotin-labeled anti-HA to specifically label HA-RAGE. The specific binding of AHA-QDs for HA-RAGE is measured using cells that are incubated with 100 pM AHA-QDs as shown in Figure S3.5. The number of AHA-QDs per cell is counted for at least 34 cells expressing HA-RAGE or lacking HA-RAGE. There is 4.8% nonspecific AHA-QD binding, indicating that a majority of the AHA-QDs observed in the HA-RAGE expressing cells are

specifically bound to HA-RAGE. A goal of this work is to measure the diffusion properties of HA-RAGE as measured by the trajectories of AHA-QDs. The nonspecifically bound AHA-QDs on the cell membrane are immobile and do not diffuse. To prevent biasing the HA-RAGE diffusion measurements, the immobile AHA-QDs are excluded from the analysis since immobile trajectories could arise from either nonspecific binding or immobile HA-RAGE. Excluding the immobile AHA-QDs from the analysis does prohibit measuring the fraction of immobile HA-RAGE.

**Diffusion properties for the Brownian trajectories of HA-RAGE in the presence and absence of MGO-BSA ligand**

Fluorescence microscopy is used to collect at least 400 trajectories of AHA-QDs from at least 10 cells to measure the diffusion of HA-RAGE in the presence or absence of MGO-BSA. Trajectories are classified as exhibiting either Brownian or confined diffusion. If the trajectory has a minimum of one confined domain (where the confinement index (L) is higher than the critical confinement value for longer than the critical time as described in the experimental section) then the trajectory is classified as confined. In the absence of ligand, 31% of HA-RAGE exhibit Brownian diffusion and 69% exhibit confined diffusion, indicating a majority of HA-RAGE measured by SPT exhibit confined diffusion at least once in ~20 seconds (i.e., the average length of a trajectory as shown in Table 3.1). When the cells are incubated with MGO-BSA, a 3 to 7% increase in the Brownian population is measured when the MGO-BSA percent primary amine modification is at least 41%.

The average diffusion coefficient for the Brownian trajectories of HA-RAGE in the absence of ligand is 0.085 $\mu m^2/s$. The histogram of diffusion coefficients (Figure 3.2) shows a bimodal population with maximum diffusion coefficients of 0.0006 and 0.065 $\mu m^2/s$. When the cells are exposed to 24% MGO-BSA, the average diffusion coefficient drops to 0.039

$\mu m^2/s$ (Table 3.1). The distribution of diffusion coefficients remains bimodal but with a higher percentage of the slower population (Figure 3.2). Between 24% MGO-BSA and 62% MGO-BSA treatment, there is an increase in the average diffusion coefficient and a decrease in the population of HA-RAGE in the slower diffusion coefficient range. Interestingly, compared to the 62% MGO-BSA treatments, the average diffusion coefficient decreases after 74% MGO-BSA treatment, and there is a recurrence of the bimodal diffusion coefficient distribution. With increasing percent primary amine modification, the viscosity of the ligand solution increases, which is indicative of protein cross linking. It is possible that the decrease in the diffusion coefficient in going from the 62% to the 74% MGO-BSA sample is a result of extensive protein cross linking. The *in vitro* sRAGE binding studies (i.e., the SPR studies) may be less sensitive to the degree of protein cross linking, possibly because the sRAGE is immobilized in a range of orientations on the sensor surface that may have different binding capacities, while RAGE in the membrane is expected to have fewer degrees of freedom. Thus the affinity measured by SPR may not be representative of the binding affinity of full length RAGE in the cell membrane if extensive protein cross linking is present. It is also possible that ligand binding to another receptor (as stated above AGE binds to other receptors) may indirectly impact RAGE diffusion.

**Diffusion properties for the fraction of HA-RAGE with at least one confined domain in the presence and absence of MGO-BSA ligand**

Two regions are identified for each trajectory classified as exhibiting a confined domain based on the measured confinement index (L). First, regions inside the confined regions where L is higher than the critical confinement value for longer than the critical time. Second, since the time HA-RAGE is in confined domains (Table 3.2) is less than the average trajectory time, parts of the trajectory represent diffusion outside confined domains.

Outside of the confined domains, Brownian diffusion properties are expected. Table 3.2 and Figure 3.3 confirm that the diffusion coefficients measured outside the confined domains of diffusion are within expected experimental uncertainties to the values measured for the trajectories exhibiting pure Brownian diffusion shown in Table 3.1 and Figure 3.2, including a maximum average diffusion coefficient (0.085 $\mu m^2/s$) measured after treatment with 62% MGO-BSA. When HA-RAGE is in a confined domain and in the absence of ligand, the average diffusion coefficient is 7-fold slower compared to HA-RAGE exhibiting Brownian diffusion. For HA-RAGE in confined domains in the presence of MGO-BSA, the same trends are measured in the average diffusion coefficient and the histogram of diffusion coefficients as measured for HA-RAGE exhibiting Brownian diffusion, although the magnitude of the average diffusion coefficient is 4 to 6-fold slower within the confined domains (Table 3.2 and Figure 3.4).

The average confinement radius and time in confined domains measured for HA-RAGE in the absence of ligand were 0.199 μm and 3.89 seconds, respectively (Table 3.2). The confinement radius decreases after treatment with 24% MGO-BSA, and the confinement radius is the largest after 62% MGO-BSA treatment (Figure 3.5, Table 3.2).

Overall the confinement radius shows the same trend as the average diffusion coefficient with increasing MGO-BSA percent primary amine modification. The time HA-RAGE remains in confined domains remains approximately 4 seconds after cellular incubation with MGO-BSA. While the size of the domains of confined diffusion varies with MGO-BSA incubation, the time HA-RAGE spends within these domains is relatively independent of ligand incubation.

**p-ERK and HA-RAGE expression are independent of the percent primary amine modification on MGO-BSA**

Phosphorylation of ERK (p-ERK) and Akt (p-Akt) have been used to measure RAGE signaling [14, 29]. After incubation with MGO-BSA, there is a 2 to 2.4-fold increase in p-ERK compared to p-ERK measured in the absence of MGO-BSA (Figure 3.6A and 3.6B). There is no statistically significant difference in p-ERK phosphorylation for cells incubated with varying MGO-BSA percent primary amine modifications. A similar trend was measured for cells lacking HA-RAGE expression (Figure S3.3). Given the similar response in cells that express HA-RAGE and cells lacking HA-RAGE expression, it is possible that a non-RAGE-dependent mechanism is responsible for some or all of the increase in p-ERK after incubation with MGO-BSA. While it cannot be concluded that MGO-BSA incubation results in a RAGE-dependent increase in p-ERK, the experimental design ensures the changes in the diffusion properties discussed above are specific to RAGE, whether or not they are the result of a direct interaction between MGO-BSA and RAGE or an indirect interaction with other membrane components. In contrast to the increasing p-ERK phosphorylation after MGO-BSA incubation, no statistically significant difference in p-Akt is measured is cells expressing or lacking HA-RAGE (Figure S3.6).

There is a 15 to 28% decrease in HA-RAGE expression after incubating cells with MGO-BSA (Figure 3.6C and 3.6D). As with p-ERK, the reduced HA-RAGE expression is statistically the same regardless of the percent primary amine modification on MGO-BSA. Previously, RAGE expression was shown to be down regulated in monocytes upon incubation with AGE prepared by glyceraldehyde modification [32]. The glyceraldehyde-prepared AGE reported in this previous study best matches the AGE used in the studies

reported herein. In some experimental conditions, RAGE expression has been shown to be upregulated by incubation with ligand [33, 34].

**Insight into the nature of the confined domains of diffusion: Cholesterol depletion eliminates the ligand-induced changes to HA-RAGE diffusion**

Previously RAGE has been reported to be part of cholesterol rich membrane domains [35, 36]. However, cholesterol depletion did not affect the lateral diffusion properties of RAGE as observed with FRAP [14]. As measured by SPT, HA-RAGE diffusion is 2 to 4× slower for Brownian and confined diffusion when cholesterol is extracted from the cell membrane (Table 3, 4). In addition the radius of confined diffusion decreases from 0.199 μm to 0.160 μm after cholesterol extraction. These changes are similar to the changes measured after 24% MGO-BSA incubation (Table 3.1, 3.2).

The effect of cholesterol depletion on ligand-induced changes in HA-RAGE lateral diffusion is explored by depleting cholesterol from untreated and 62% MGO-BSA-treated cells. Considering all diffusion properties for Brownian and confined diffusion, the changes in HA-RAGE diffusion that are measured after 62% MGO-BSA treatment are not measured when cholesterol is extracted from the membrane (Table 3.3, 3.4 and Figure S3.7, S3.8, S3.9 and S3.10). After treatment with 62% MGO-BSA and cholesterol extraction, the HA-RAGE diffusion parameters are similar to the values measured after cholesterol extraction without ligand incubation. The 62% MGO-BSA-induced changes in HA-RAGE diffusion are cholesterol dependent, and are not measured when cholesterol concentrations and/or cholesterol-dependent structures in the membrane are altered. It is possible that the effect of cholesterol depletion on RAGE diffusion is dependent upon the level of primary amine modifications, and is worthy of further study.

### 3.5 Conclusions

MGO-BSA binding affinity to sRAGE was observed to be dependent on the percent primary amine modification and the net negative surface charge on the ligand. MGO-BSA incubation affected HA-RAGE lateral diffusion, however, there was no direct correlation measured between ligand binding affinity, net negative surface charge on the ligand and HA-RAGE diffusion coefficient, radius of confinement or duration of confinement. This may be the result of increasing levels of protein cross linking with increasing primary amine modification. Cholesterol depletion was found to ameliorate the 62% MGO-BSA ligand induced changes on HA-RAGE lateral diffusion, indicating a direct or indirect role for cholesterol in MGO-BSA-induced changes to HA-RAGE diffusion. Other factors such as ligand valancy and receptor clustering, as well as, other membrane changes that may result from the MGO-BSA ligand are possible avenues for further study.

### 3.6 References

[1] G.R. Barile, A.M. Schmidt, RAGE and its ligands in retinal disease, *Curr Mol Med*, 7 (2007) 758-765.

[2] C.D. Logsdon, M.K. Fuentes, E.H. Huang, T. Arumugam, RAGE and RAGE ligands in cancer, *Curr Mol Med*, 7 (2007) 777-789.

[3] S.D. Yan, X. Chen, J. Fu, M. Chen, H. Zhu, A. Roher, T. Slattery, L. Zhao, M. Nagashima, J. Morser, A. Migheli, P. Nawroth, D. Stern, A.M. Schmidt, RAGE and amyloid-beta peptide neurotoxicity in Alzheimer's disease, *Nature*, 382 (1996) 685-691.

[4] G. Fritz, RAGE: a single receptor fits multiple ligands, *Trends Biochem Sci*, 36 (2011) 625-632.

[5] S.D. Yan, A. Bierhaus, P.P. Nawroth, D.M. Stern, RAGE and Alzheimer's disease: a progression factor for amyloid-beta-induced cellular perturbation?, *J Alzheimers Dis*, 16 (2009) 833-843.

[6] A.M. Schmidt, M. Vianna, M. Gerlach, J. Brett, J. Ryan, J. Kao, C. Esposito, H. Hegarty, W. Hurley, M. Clauss, et al., Isolation and characterization of two binding proteins for advanced glycosylation end products from bovine lung which are present on the endothelial cell surface, *J Biol Chem*, 267 (1992) 14987-14997.

[7] E. Leclerc, G. Fritz, S.W. Vetter, C.W. Heizmann, Binding of S100 proteins to RAGE: an update, *Biochim Biophys Acta*, 1793 (2009) 993-1007.

[8] A. Goldin, J.A. Beckman, A.M. Schmidt, M.A. Creager, Advanced glycation end products: sparking the development of diabetic vascular injury, *Circulation*, 114 (2006) 597-605.

[9] H. Park, F.G. Adsit, J.C. Boyington, The 1.5 A crystal structure of human receptor for advanced glycation endproducts (RAGE) ectodomains reveals unique features determining ligand binding, *J Biol Chem*, 285 (2010) 40762-40770.

[10] M. Koch, S. Chitayat, B.M. Dattilo, A. Schiefner, J. Diez, W.J. Chazin, G. Fritz, Structural basis for ligand recognition and activation of RAGE, *Structure*, 18 (2010) 1342-1352.

[11] Y. Yamamoto, H. Yonekura, T. Watanabe, S. Sakurai, H. Li, A. Harashima, K.M. Myint, M. Osawa, A. Takeuchi, M. Takeuchi, H. Yamamoto, Short-chain aldehyde-derived ligands for RAGE and their actions on endothelial cells, *Diabetes Research and Clinical Practice*, 77 (2007) S30-S40.

[12] T. Ostendorp, E. Leclerc, A. Galichet, M. Koch, N. Demling, B. Weigle, C.W. Heizmann, P.M. Kroneck, G. Fritz, Structural and functional insights into RAGE activation by multimeric S100B, *EMBO J*, 26 (2007) 3868-3878.

[13] J. Xue, R. Ray, D. Singer, D. Bohme, D.S. Burz, V. Rai, R. Hoffmann, A. Shekhtman, The receptor for advanced glycation end products (RAGE) specifically recognizes methylglyoxal-derived AGEs, *Biochemistry*, 53 (2014) 3327-3335.

[14] A. Syed, Q. Zhu, E. Smith, Lateral Diffusion and Signaling of Receptor for Advanced Glycation End-products (RAGE): A Receptor Involved in Chronic Inflammation, *Eur Biophys J*, Submitted (2016).

[15] M.J. Saxton, Single-particle tracking: the distribution of diffusion coefficients, *Biophys J*, 72 (1997) 1744-1753.

[16] F. Daumas, N. Destainville, C. Millot, A. Lopez, D. Dean, L. Salome, Confined diffusion without fences of a G-protein-coupled receptor as revealed by single particle tracking, *Biophysical Journal*, 84 (2003) 356-366.

[17] I. Chung, R. Akita, R. Vandlen, D. Toomre, J. Schlessinger, I. Mellman, Spatial control of EGF receptor activation by reversible dimerization on living cells, *Nature*, 464 (2010) 783-U163.

[18] K. Notelaers, S. Rocha, R. Paesen, N. Smisdom, B. De Clercq, J.C. Meier, J.M. Rigo, J. Hofkens, M. Ameloot, Analysis of alpha 3 GlyR single particle tracking in the cell membrane, *Biochimica Et Biophysica Acta-Molecular Cell Research*, 1843 (2014) 544-553.

[19] H. Bannai, S. Levi, C. Schweizer, M. Dahan, A. Triller, Imaging the lateral diffusion of membrane molecules with quantum dots, *Nat Protoc*, 1 (2006) 2628-2634.

[20] L. Cognet, C. Leduc, B. Lounis, Advances in live-cell single-particle tracking and dynamic super-resolution imaging, *Curr Opin Chem Biol*, 20 (2014) 78-85.

[21] J.V. Valencia, S.C. Weldon, D. Quinn, G.H. Kiers, J. DeGroot, J.M. TeKoppele, T.E. Hughes, Advanced glycation end product ligands for the receptor for advanced glycation end products: biochemical characterization and formation kinetics, *Anal Biochem*, 324 (2004) 68-78.

[22] D.J. O'Shannessy, M. Brigham-Burke, K.K. Soneson, P. Hensley, I. Brooks, Determination of rate and equilibrium binding constants for macromolecular interactions using surface plasmon resonance: use of nonlinear least squares analysis methods, *Anal Biochem*, 212 (1993) 457-468.

[23] I.F. Sbalzarini, P. Koumoutsakos, Feature point tracking and trajectory analysis for video imaging in cell biology, *J Struct Biol*, 151 (2005) 182-195.

[24] D. Mainali, E.A. Smith, Select cytoplasmic and membrane proteins increase the percentage of immobile integrins but do not affect the average diffusion coefficient of mobile integrins, *Anal Bioanal Chem*, 405 (2013) 8561-8568.

[25] S.A. Menchon, M.G. Martin, C.G. Dotti, APM_GUI: analyzing particle movement on the cell membrane and determining confinement, *BMC Biophys*, 5 (2012) 4.

[26] R. Simson, E.D. Sheets, K. Jacobson, Detection of temporary lateral confinement of membrane proteins using single-particle tracking analysis, *Biophys J*, 69 (1995) 989-993.

[27] J. Xie, S. Reverdatto, A. Frolov, R. Hoffmann, D.S. Burz, A. Shekhtman, Structural basis for pattern recognition by the receptor for advanced glycation end products (RAGE), *J Biol Chem*, 283 (2008) 27255-27269.

[28] L. Yatime, G.R. Andersen, Structural insights into the oligomerization mode of the human receptor for advanced glycation end-products, *Febs J*, 280 (2013) 6556-6568.

[29] H. Zong, A. Madden, M. Ward, M.H. Mooney, C.T. Elliott, A.W. Stitt, Homodimerization Is Essential for the Receptor for Advanced Glycation End Products (RAGE)-mediated Signal Transduction, *J. Biol. Chem.*, 285 (2010) 23137-23146.

[30] X. Michalet, F.F. Pinaud, L.A. Bentolila, J.M. Tsay, S. Doose, J.J. Li, G. Sundaresan, A.M. Wu, S.S. Gambhir, S. Weiss, Quantum dots for live cells, in vivo imaging, and diagnostics, *Science*, 307 (2005) 538-544.

[31] D. Mainali, E.A. Smith, The effect of ligand affinity on integrins' lateral diffusion in cultured cells, *Eur Biophys J*, 42 (2013) 281-290.

[32] J. Miura, Y. Uchigata, Y. Yamamoto, M. Takeuchi, S. Sakurai, T. Watanabe, H. Yonekura, S.-i. Yamagishi, Z. Makita, A. Sato, Y. Omori, H. Yamamoto, Y. Iwamoto, AGE down-regulation of monocyte RAGE expression and its association with diabetic complications in type 1 diabetes, *Journal of Diabetes and its Complications*, 18 (2004) 53-59.

[33] L. Yu, Y. Zhao, S. Xu, F. Ding, C. Jin, G. Fu, S. Weng, Advanced Glycation End Product (AGE)-AGE Receptor (RAGE) System Upregulated Connexin43 Expression in Rat Cardiomyocytes via PKC and Erk MAPK Pathways, *International Journal of Molecular Sciences*, 14 (2013) 2242-2257.

[34] N. Tanaka, H. Yonekura, S.i. Yamagishi, H. Fujimori, Y. Yamamoto, H. Yamamoto, The Receptor for Advanced Glycation End Products Is Induced by the Glycation Products Themselves and Tumor Necrosis Factor- through Nuclear Factor- B, and by 17 -Estradiol through Sp-1 in Human Vascular Endothelial Cells, *J. Biol. Chem.*, 275 (2000) 25781-25790.

[35] O. Sbai, T.S. Devi, M.A. Melone, F. Feron, M. Khrestchatisky, L.P. Singh, L. Perrone, RAGE-TXNIP axis is required for S100B-promoted Schwann cell migration, fibronectin expression and cytokine secretion, *J Cell Sci*, 123 (2010) 4332-4339.

[36] M.P. Lisanti, P.E. Scherer, J. Vidugiriene, Z. Tang, A. Hermanowski-Vosatka, Y.H. Tu, R.F. Cook, M. Sargiacomo, Characterization of caveolin-rich membrane domains isolated from an endothelial-rich source: implications for human disease, *J Cell Biol*, 126 (1994) 111-126.

## 3.7 Figures and Tables

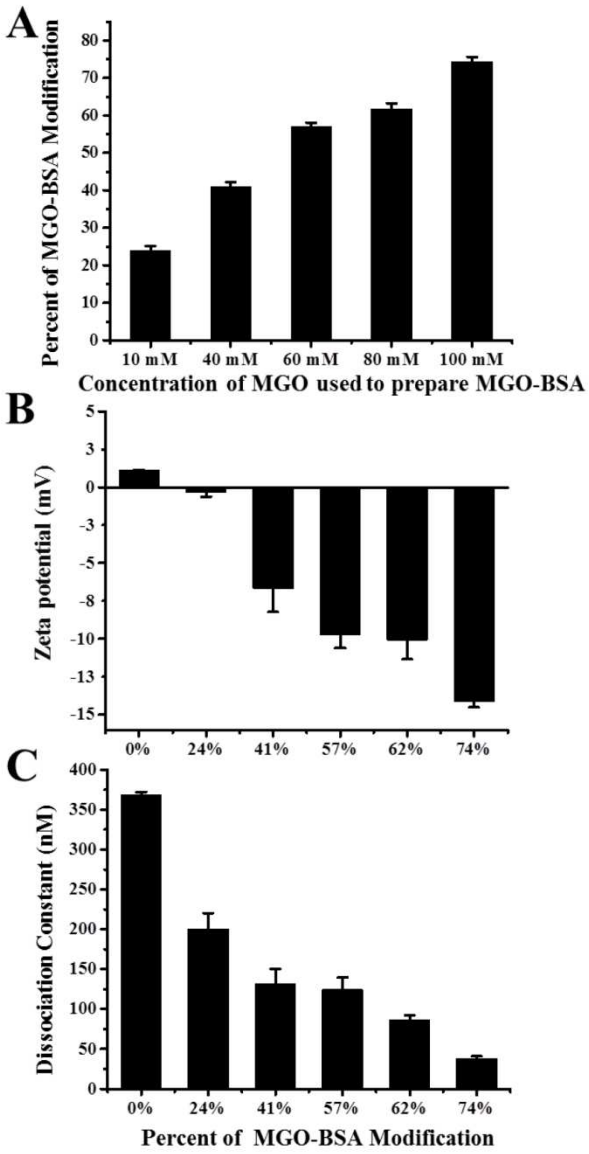


**Figure 3.1.** Characterization of methylglyoxal modified-bovine serum albumin (MGO-BSA). (A) Percent modification of free primary amines in BSA as measured by an ortho-phthaldialdehyde assay after modification with the indicated concentration of MGO; (B) Measured Zeta potential for MGO-BSA with the indicated percent primary amine modification; (C) Dissociation constant as measured by SPR for MGO-BSA with the indicated percent primary amine modification and sRAGE.

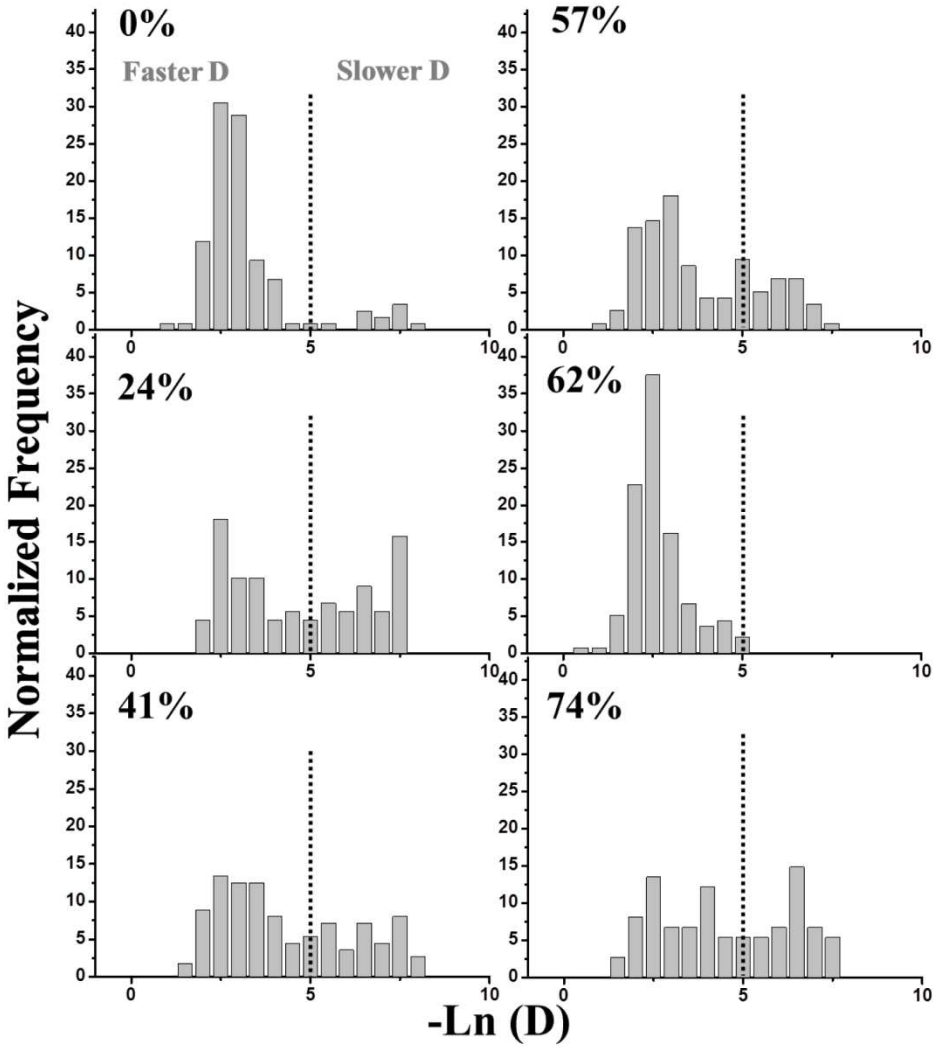


**Figure 3.2.** Histograms of diffusion coefficients for the Brownian trajectories of HA-RAGE in the GM07373 cell membrane treated with MGO-BSA having the indicated percent primary amine modification. The diffusion coefficient is plotted as the negative natural logarithm; slower diffusion coefficients appear on the right side of the graph. The dotted line is shown for clarity in comparing the changes in the distribution.

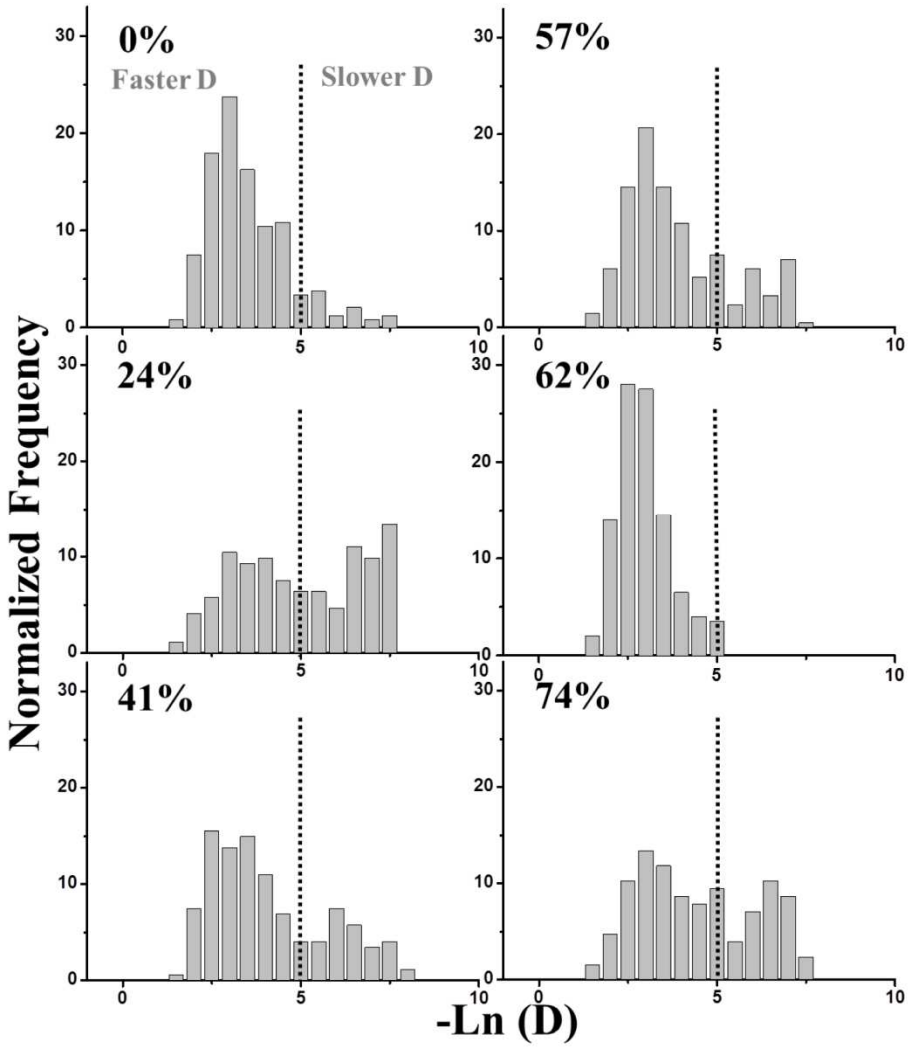


**Figure 3.3.** Histograms of diffusion coefficients for the confined trajectories (outside domains of confined diffusion) of HA-RAGE in the GM07373 cell membrane treated with MGO-BSA having the indicated percent primary amine modification. The diffusion coefficient is plotted as the negative natural logarithm. The dotted line is shown for clarity in comparing the changes in the distribution.

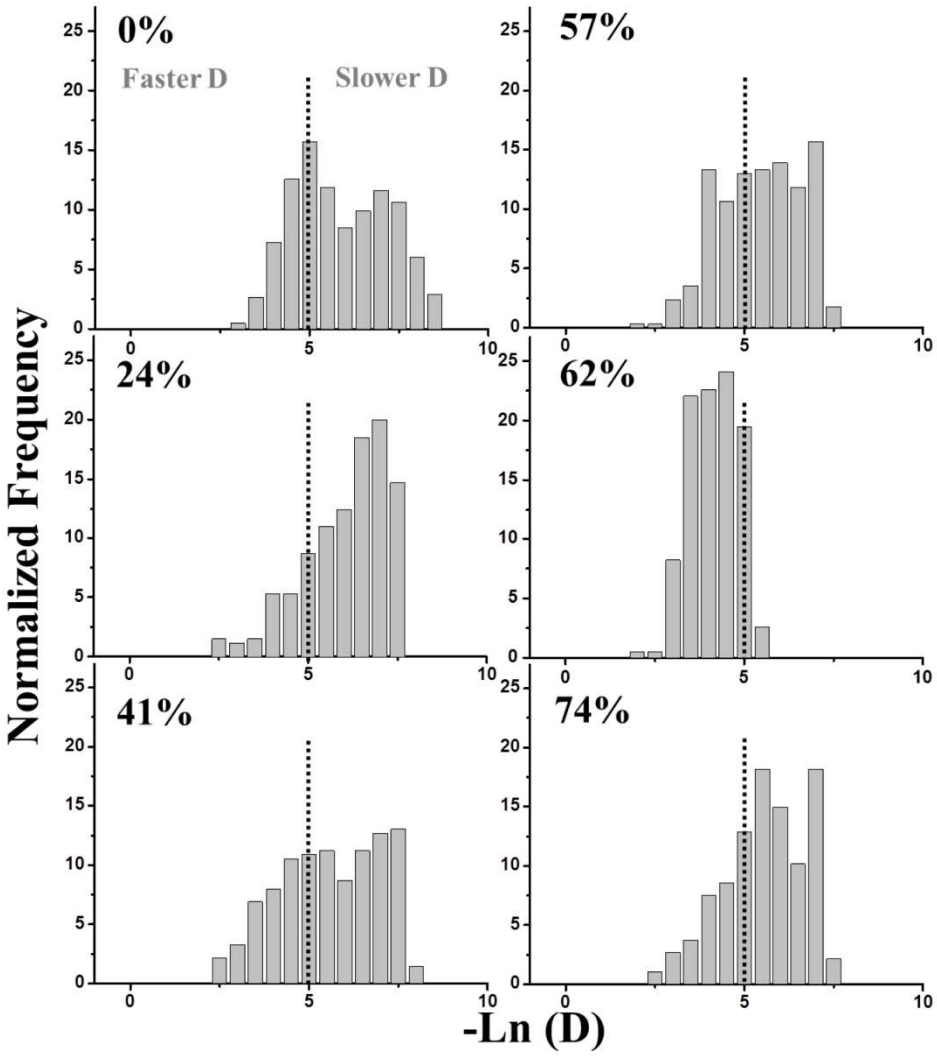


**Figure 3.4.** Histograms of diffusion coefficients for the confined trajectories (inside domains of confined diffusion) of HA-RAGE in GM07373 cell membrane treated with MGO-BSA having the indicated percent primary amine modification. The diffusion coefficient is plotted as the negative natural logarithm. The dotted line is shown for clarity in comparing the changes in the distribution.

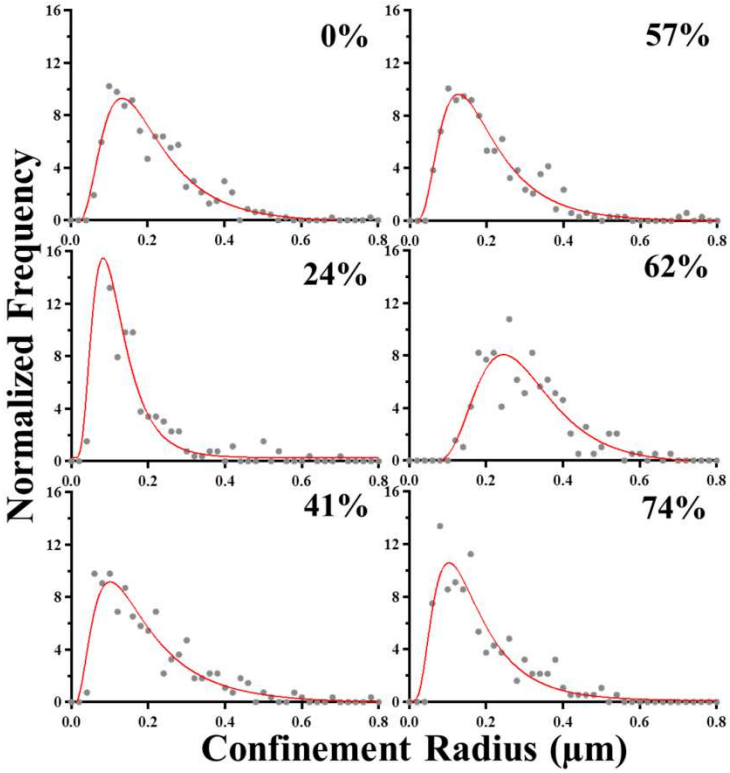


**Figure 3.5.** Distribution of confinement radius for the confined trajectories (inside domains of confined diffusion) of HA-RAGE in the GM07373 cell membrane treated with MGO-BSA having the indicated percent primary amine modification. The corresponding fits (red solid line) are obtained by fitting the distribution to a log-normal function.

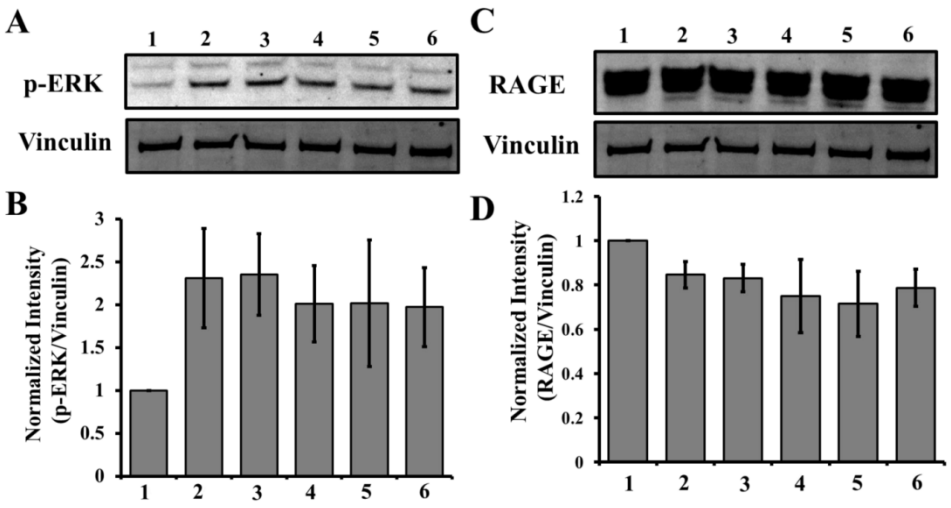


**Figure 3.6.** Western blot analysis of phosphorylation of ERK (p-ERK) and HA-RAGE expression in the GM07373 cell lysate with: (Lane 1) no treatment, or 5 mg/mL MGO-BSA treatment with the following percent primary amine modification: (Lane 2) 24%, (Lane 3) 41%, (Lane 4) 57%, (Lane 5) 62%, or (Lane 6) 74%. Fluorescence images of the PVDF membrane probed with: (A) p-ERK antibody or vinculin antibody, and (C) RAGE antibody or vinculin antibody. Average (n = 5) fluorescence intensities of the: (B) 42 kDa band of p-ERK divided by the vinculin band and (D) RAGE band divided by the vinculin band.

**Table 3.1.** Average diffusion parameters for the **Brownian trajectories** of HA-RAGE in the GM07373 cell membrane treated with MGO-BSA with the indicated percent primary amine modification.

| | **% of Brownian trajectories** | **D ($\mu m^2/s$)** | **Average length of the trajectory (s)** |
|---|---|---|---|
| No treatment | 31% | 0.085 | 20 ± 10 |
| 24% MGO-BSA treatment | 31% | **0.039 ($p < 0.01$)** | 19 ± 9 |
| 41% MGO-BSA treatment | 36% | **0.052 ($p < 0.01$)** | 19 ± 9 |
| 57% MGO-BSA treatment | 34% | **0.069 ($p < 0.01$)** | 20 ± 10 |
| 62% MGO-BSA treatment | 39% | **0.115 ($p < 0.01$)** | 20 ± 9 |
| 74% MGO-BSA treatment | 36% | **0.050 ($p < 0.01$)** | 30 ± 10 |

Diffusion coefficients with a p-value below 0.05 are highlighted in bold to show statistically significant differences compared to the cells that were not treated. The percentage of Brownian trajectories is obtained from counting, so no uncertainty is provided.

**Table 3.2.** Average diffusion parameters for the **confined trajectories** of HA-RAGE in the GM07373 cell membrane treated with MGO-BSA with the indicated percent primary amine modification.

| | **D ($\mu m^2/s$) (Outside confined domains)** | **D ($\mu m^2/s$) (Inside confined domains)** | **Radius ($\mu m$)** | **Confinement time (s)** | **Average length of the trajectory (s)** |
|---|---|---|---|---|---|
| No treatment | 0.060 | 0.012 | 0.199 | 3.89 | 32 ± 9 |
| 24% MGO-BSA treatment | **0.031 (p < 0.01)** | **0.007 (p < 0.01)** | **0.138 (p < 0.01)** | **4.09 (p < 0.01)** | 31 ± 9 |
| 41% MGO-BSA treatment | **0.050 (p < 0.01)** | 0.013 (p=0.09) | **0.192 (p < 0.01)** | 3.90 (p=0.07) | 30 ± 10 |
| 57% MGO-BSA treatment | **0.053 (p < 0.01)** | 0.011 (p=0.09) | 0.195 (p=0.06) | 3.99 (p=0.2) | 30 ± 10 |
| 62% MGO-BSA treatment | **0.085 (p < 0.01)** | **0.026 (p < 0.01)** | **0.294 (p < 0.01)** | 3.46 (p=0.19) | 31 ± 9 |
| 74% MGO-BSA treatment | **0.042 (p < 0.01)** | **0.010 (p=0.01)** | **0.178 (p=0.02)** | **3.97 (p < 0.01)** | 20 ± 10 |

Entries with a p-value below 0.05 are highlighted in bold to show statistically significant differences compared to the cells that were not treated.

**Table 3.3.** Average diffusion parameters for the Brownian trajectories for HA-RAGE in the GM07373 cell membrane for the indicated cellular treatments.

| | **% of Brownian trajectories** | **D ($\mu m^2/s$)** | **Average length of the trajectory (s)** |
|---|---|---|---|
| No treatment | 31% | 0.085 | 20 ± 10 |
| 62% MGO-BSA ligand | 36% | **0.115 ($p < 0.01$)** | 20 ± 9 |
| 5 mM MβCD to extract cholesterol | 33% | **0.036 ($p < 0.01$)** | 19 ± 9 |
| 62% MGO-BSA and 5mM MβCD | 34% | **0.041 ($p < 0.01$)** | 18 ± 9 |

Diffusion coefficients with a p-value below 0.05 are highlighted in bold to show statistically significant differences compared to the cells that were not treated. The percentage of Brownian trajectories is obtained from counting, so no uncertainty is provided.

**Table 3.4.** Average diffusion parameters for the confined trajectories for HA-RAGE in the GM07373 cell membrane for the indicated cellular treatments.

| | **D ($\mu m^2/s$) (Outside confined domains)** | **D ($\mu m^2/s$) (Inside confined domains)** | **Radius ($\mu m$)** | **Confinement time (s)** | **Average length of the trajectory (s)** |
|---|---|---|---|---|---|
| No treatment | 0.06 | 0.012 | 0.199 | 3.89 | 32 ± 9 |
| 62% MGO-BSA ligand | **0.085 ($p < 0.01$)** | **0.026 ($p < 0.01$)** | **0.294 ($p < 0.01$)** | 3.46 (p=0.19) | 31 ± 9 |
| 5 mM MβCD to extract cholesterol | **0.035 ($p < 0.01$)** | **0.003 ($p < 0.01$)** | **0.160 ($p < 0.01$)** | 3.94 (p=0.55) | 30 ± 10 |
| 62% MGO-BSA and 5mM MβCD | **0.038 ($p < 0.01$)** | **0.008 ($p < 0.01$)** | **0.164 ($p < 0.01$)** | 3.92 (p=0.33) | 30 ± 10 |

Entries with a p-value below 0.05 are highlighted in bold to show statistically significant differences compared to the cells that were not treated.

## 3.8 Supporting Information

### HA-RAGE plasmid, expression and purification

Full-length human RAGE coding pcDNA3 vector (pcDNA3.RAGE) was a generous gift from Prof. Ann Marie Schmidt (New York School of Medicine) [1]. All oligonucleotides for generating recombinant proteins were obtained from Integrated DNA Technologies (Coralville, IA). The DNA sequence coding for human influenza hemagglutinin (HA) tag (YPYDVPDYA) was inserted in the N-terminal of RAGE plasmid using the following oligonucleotides 5'-TACCCGTACGACGTGCCGGACTACGCCATCACAGCCCGGATTGGC-3' and 5'-GGCGTAGTCCGGCACGTCGTAGTTTTGAGCACCTACTACTGCCC-3' to generate pcDNA3.HA-RAGE plasmid as reported previously [2]. The recombinant plasmid was first transformed into DH5α *E. Coli* cells for expression and purification and transformed cells were selected on Luria broth agar (US biological, Salem, MA) plates containing 50 μg/mL Carbenicillin (Sigma-Aldrich, St. Louis, MO).

### Expression and purification of soluble RAGE

Soluble RAGE (sRAGE) is an endogenous splice variant of full length RAGE lacking the transmembrane and intracellular domains. His-tagged sRAGE transformed *E. Coli* strain *Origami™ B (DE3)* was a generous gift from Dr. Walter Chazin (Vanderbilt University). The cells were grown at 37 °C until the optical density at 600 nm was approximately 0.8 AU. Then sRAGE's expression was induced with 0.5 mM isopropyl β-D-1-thiogalactopyranoside. After 6 hours at room temperature, cells were harvested and the resulting cell pellet was resuspended in buffer A (20mM Tris-HCL, 300 mM NaCl, 20 mM imidazole at pH 8.0) with 5 mg/mL lysozyme. His-tagged sRAGE from the cell lysate was purified with nickel nitrilotriacetic acid (Ni-NTA) agarose beads (Qiagen) using the manufacturer's instructions.

The Ni-NTA column was washed with buffer A, and elution fractions were collected in buffer B (20 mM Tris-HCL, 300 mM NaCl, 150 mM imidazole at pH 8.0). The fractions containing sRAGE were dialyzed with HEPES buffer (15 mM HEPES, 150 mM NaCl at pH 7.5) for 24 hours. Finally, the sRAGE's concentration was quantified with the bicinchoninic acid assay.

**Kinetic equations for interaction between MGO-BSA and sRAGE in SPR experiment**

Taking into account the mass transfer in the flow channel, the interaction can be described by following shceme. The sensorgrams (Figure S3.2) were fitted by following equations.

$$[A]_{bulk} \underset{k_{tr}}{\overset{k_{tr}}{\rightleftharpoons}} [A]_s + [B] \underset{k_{off}}{\overset{k_{on}}{\rightleftharpoons}} [AB]$$

$$\frac{d[AB]}{dt} = k_{on}[A]_s[B] - k_{off}[AB]$$

$$\frac{d[A]_s}{dt} = k_{tr}[A]_{bulk} - k_{tr}[A]_s - k_{on}[A]_s[B] + k_{off}[AB]$$

$$\frac{d[A]_{bulk}}{dt} = -(k_{tr}[A]_{bulk} - k_{tr}[A]_s)$$

Where $[A]_{bulk}$ is the solution concentration of sRAGE flowed into the flow cell. $[A]_s$ is the concentration of sRAGE due to the mass transfer near to the surface. [B] is the concentration of MGO-BSA. $k_{tr}$ is the mass transfer rate constant. $k_{on}$ and $k_{off}$ are the association and dissociation rate constant, respectively. The dissociation constant is defined as $K_d = k_{off}/k_{on}$.

**Western blot analysis**

GM07373 or HA-RAGE expressing GM07373 cells were sub-cultured in 25 $cm^2$ culture flasks for 24 hours. On the following day, cells were incubated in 3% BSA in DMEM media overnight. Cells were either used without further treatment or treated with specific 5

mg/mL MGO modified-BSA (MGO-BSA) in DMEM with 3% (w/v) BSA for 1 hour. For sequential cholesterol depletion, cells were further incubated with 5 mM MβCD in in DMEM with 3% (w/v) BSA for 30 minutes. Cells were rinsed with phosphate buffered saline (PBS) prior to cell lysis. Cell lysis was performed with 300 µL of cold RIPA buffer (150 mM sodium chloride, 1.0% NP-40 detergent, 0.5% sodium deoxycholate, 0.1% SDS, 50 mM Tris, pH 8.0) with Halt™ protease inhibitor cocktail (1×, Thermo Scientific, Rockford, IL). After the initial lysis treatment, cells were passed through a 21 gauge needle to ensure complete cell lysis. The protein mixture (20 µL of the sample, 7 µL of gel loading buffer and 3 µL of sample reducing agent) was first separated on a NuPAGE® Novex® 4-12% Bis-Tris protein gel (Life Technology, Eugene, OR) and then electro blotted onto Immun-Blot® LF PVDF membrane (Bio-Rad, Hercules, CA) as described previously [3, 4]. The primary antibodies used for probing the PVDF membrane were: anti-RAGE rabbit (H-300, Santa Cruz Biotechnology), anti-vinculin goat (sc-7649, Santa Cruz Biotechnology), anti-p-ERK rabbit (Tyr 204, sc-101761, Santa Cruz Biotechnology), anti-p-Akt rabbit (Ser 473, sc-101761, Santa Cruz Biotechnology). Fluorescence from the labeled secondary antibody was measured on a Typhoon FLA 9500 variable mode laser scanner (GE Healthcare, Waukesha, WI). The vinculin protein band was used as a loading control in all Western blot experiments. The resulting fluorescence band intensities were quantified with ImageJ.

**Figures and tables for supporting information for Chapter 3**

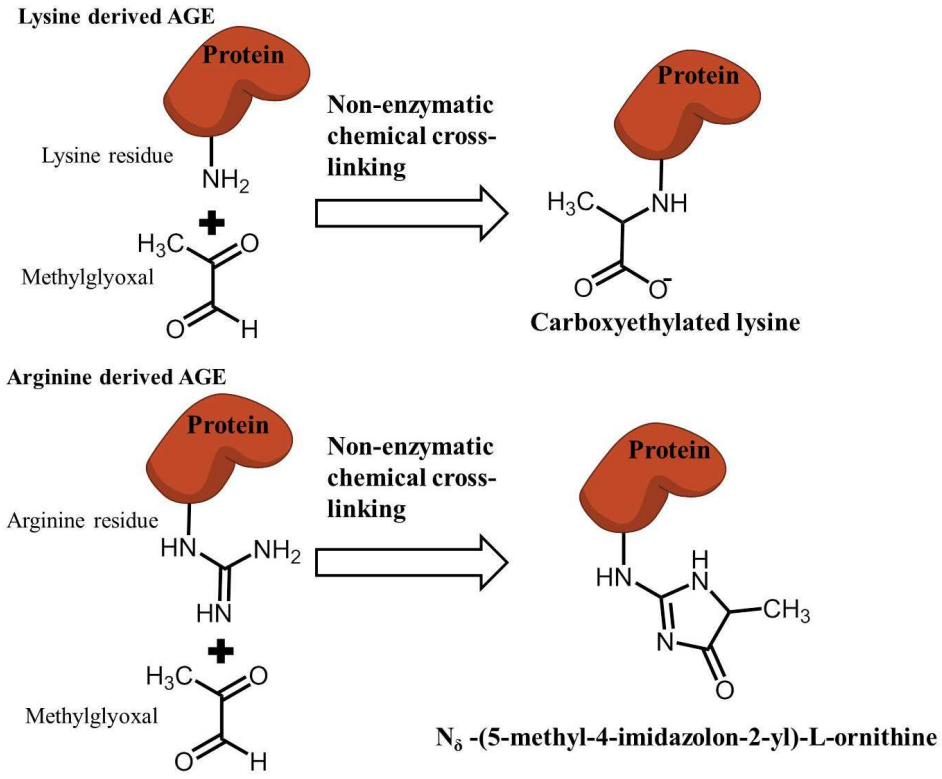


**Figure S3.1.** Two of the chemical modifications on lysine and arginine residues after incubation with methylglyoxal. A more complete list of protein modifications that can occur after incubation with methylglyoxal can be found in a review by Vistoli et al [5].

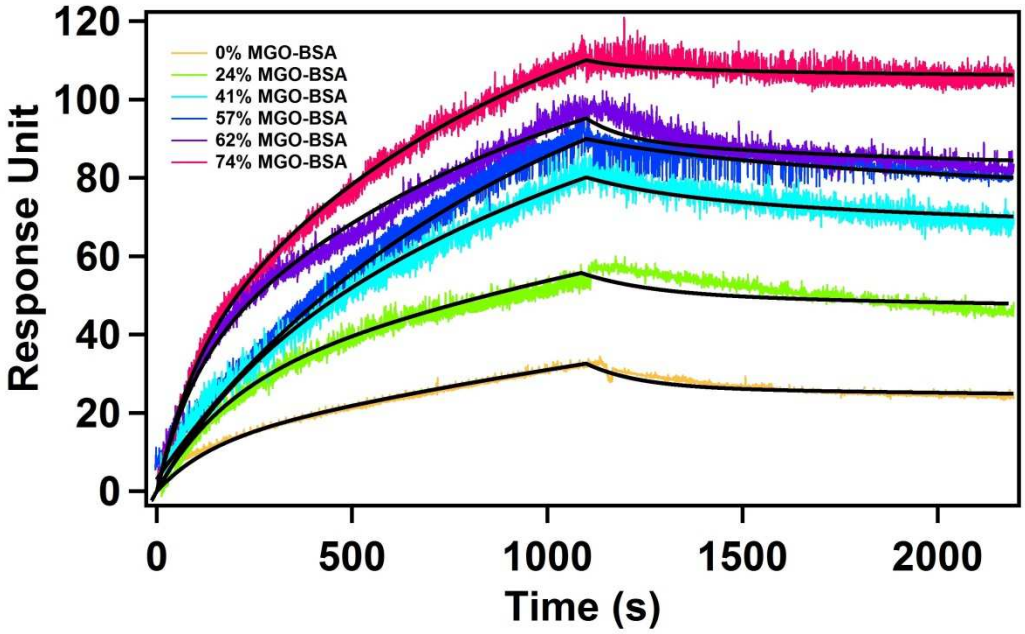


**Figure S3.2.** Measured surface plasmon resonance (SPR) response over time for binding between MGO-BSA with the indicated percent primary amine modification and sRAGE. The corresponding fits to equations 1 to 3 are shown as solid black lines.

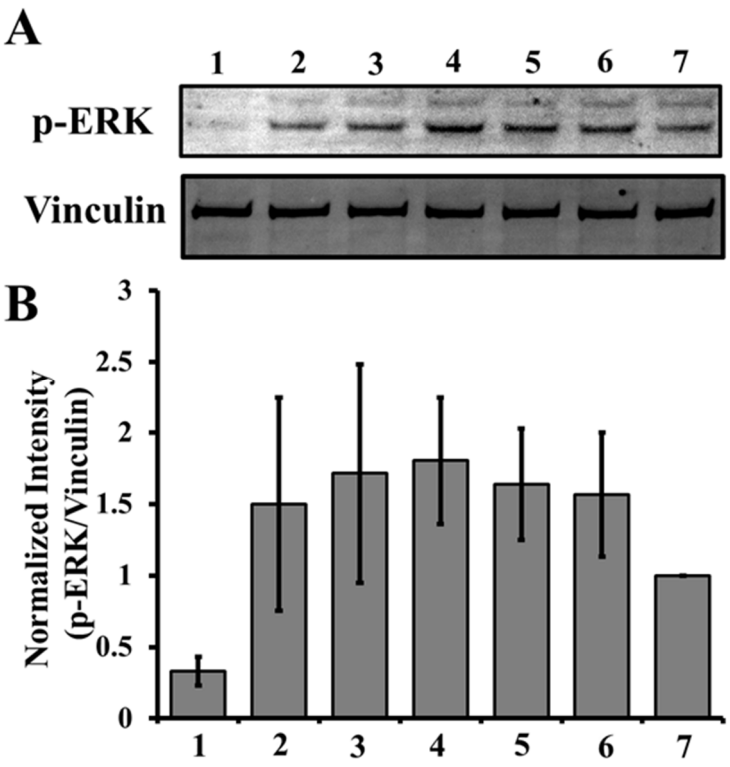


**Figure S3.3.** Western blot analysis of the GM07373 cell lysate (no detectable RAGE expression) with: (Lane 1) no treatment, or 5 mg/mL MGO-BSA treatment with the following percent primary amine modification: (Lane 2) 24%, (Lane 3) 41%, (Lane 4) 57%, (Lane 5) 62%, or (Lane 6) 74%. (Lane 7) No treatment HA-RAGE expressing GM07373 cell lysate shows higher p-ERK intensities compared to cells that do not express RAGE (Lane 1). (A) Fluorescence images of the PVDF membrane probed with p-ERK antibody or vinculin antibody. (B) Average (n = 5) normalized fluorescence intensities of the 42 kDa band of p-ERK divided by the vinculin band.

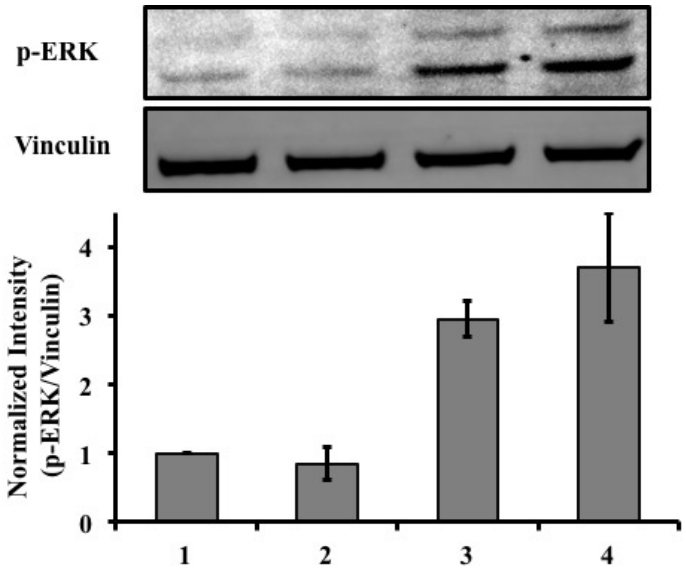


**Figure S3.4.** Western blot analysis of phosphorylation of ERK (p-ERK) in the HA-RAGE expression GM07373 cell lysate with: (Lane 1) no treatment, (Lane 2) HA antibody treatment, (Lane 3) 5 mg/mL MGO-BSA treatment with 41% primary amine modification, (Lane 4) HA antibody treatment prior to 5 mg/mL MGO-BSA treatment with 41% primary amine modification.

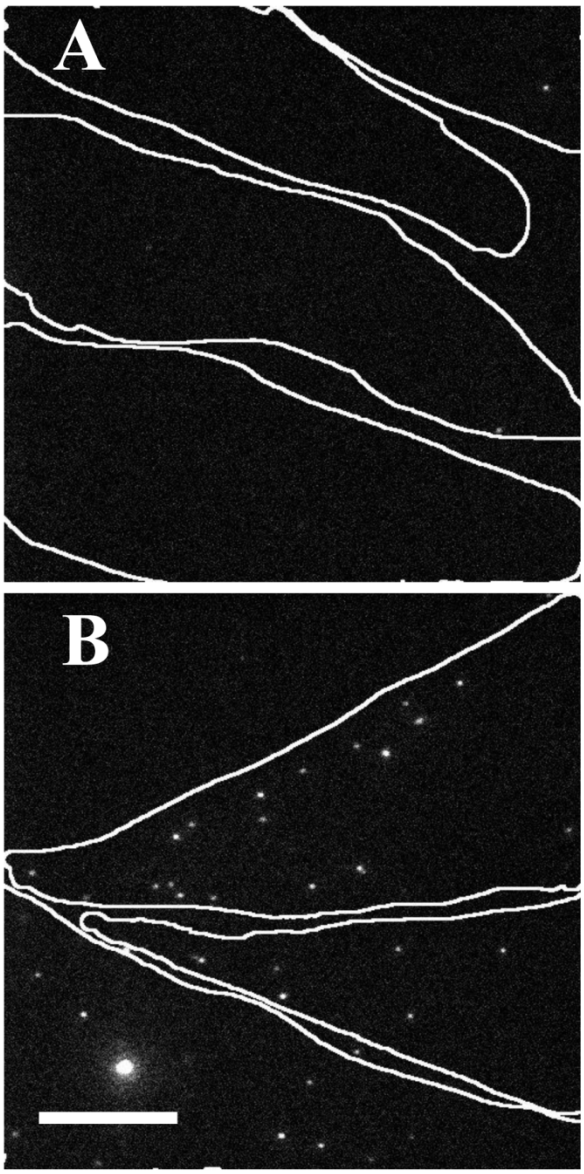


**Figure S3.5.** Representative fluorescence images after incubation of 100 pM AHA-QDs (in 0.1 % w/v BSA-imaging medium for 15 minutes at 37 ºC) with: (A) GM07373 and (B) HA-RAGE expressing GM07373 cells. The cell boundaries are outlined in white. The scale bar in the lower left corner of the image B is the same for both images: 20 µm.

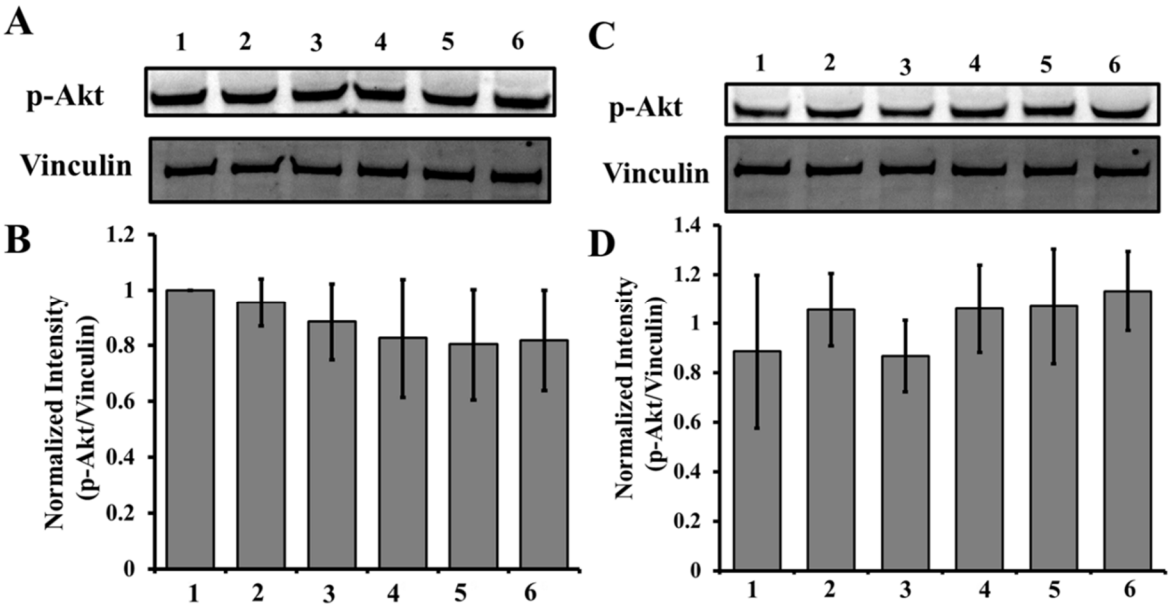


**Figure S3.6.** Western blot analysis of the (A, B) HA-RAGE expressing GM07373 or (C, D) GM07373 cell lysate with: (Lane 1) no treatment, or 5 mg/mL MGO-BSA treatment with the following percent primary amine modification: (Lane 2) 24%, (Lane 3) 41%, (Lane 4) 57%, (Lane 5) 62%, or (Lane 6) 74%. (A, C) Fluorescence images of the PVDF membrane probed with p-Akt antibody or vinculin antibody. (B, D) Average (n = 5) normalized fluorescence intensities of the 42 kDa band of p-Akt divided by the vinculin band.

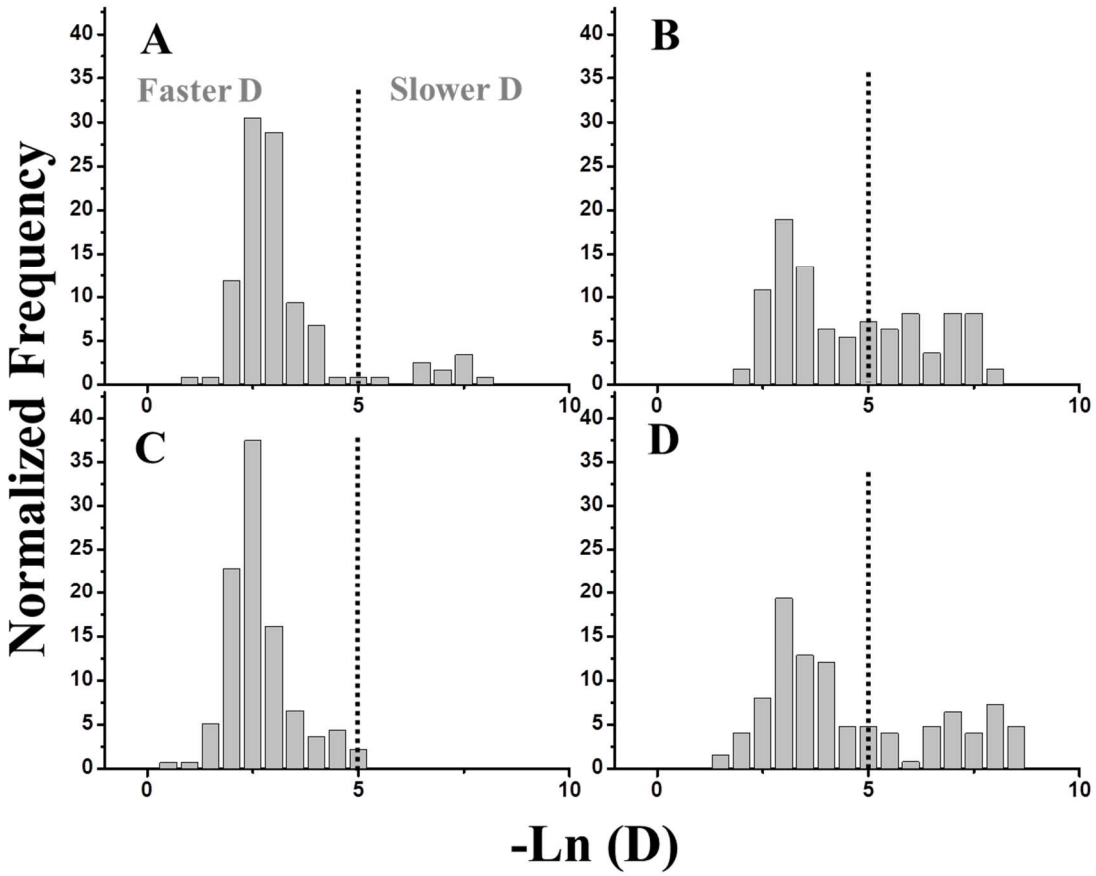


**Figure S3.7.** Histograms of diffusion coefficients for the Brownian trajectories of HA-RAGE in the GM07373 cell membrane treated with: (A) No treatment; (B) 5 mM MβCD to extract cholesterol from the membrane; (C) 62% MGO-BSA and (D) 62% MGO-BSA and 5 mM MβCD. The diffusion coefficient is plotted as the negative natural logarithm; slower diffusion coefficients appear on the right side of the graph. The dotted line is shown for clarity in comparing the changes in the distribution.

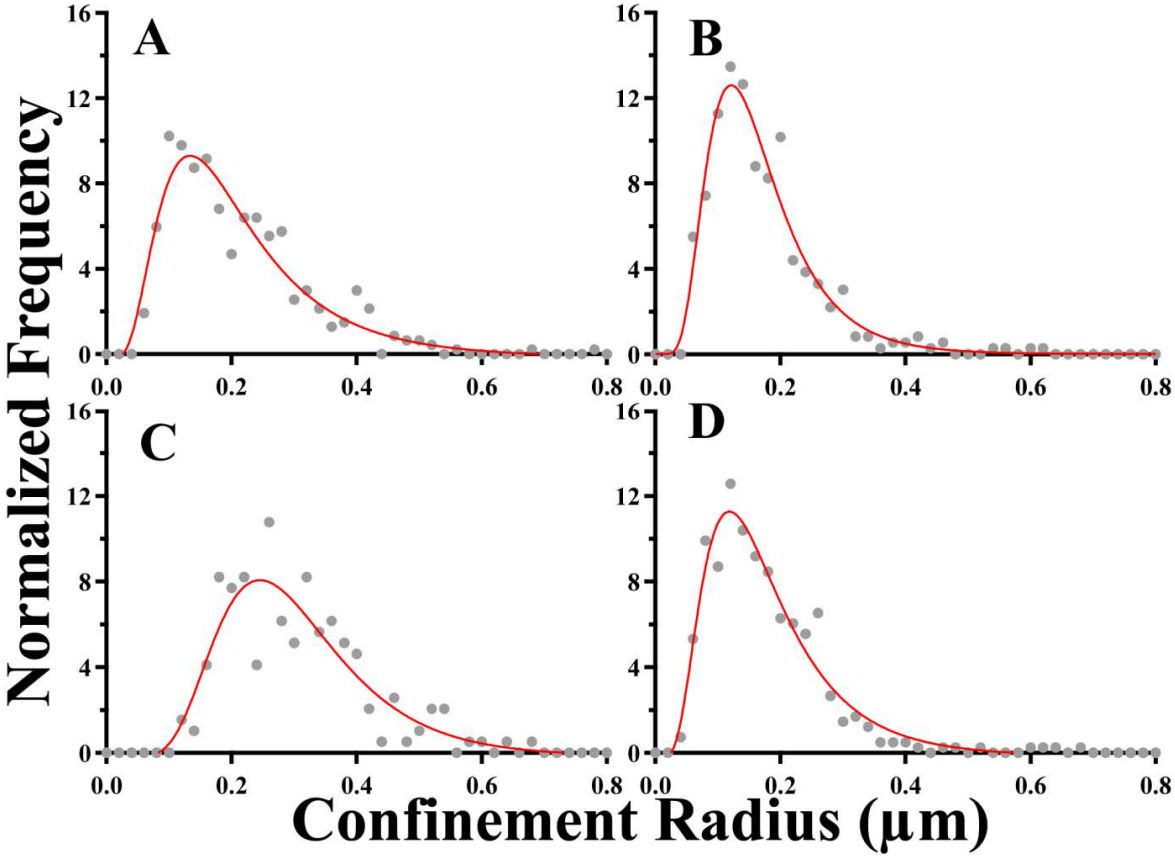


**Figure S3.8.** Distribution of confinement radius for the confined trajectories (inside domains of confined diffusion) of HA-RAGE in the GM07373 cell membrane treated with: (A) No treatment; (B) 5 mM MβCD to extract cholesterol from the membrane; (C) 62% MGO-BSA and (D) 62% MGO-BSA and 5 mM MβCD. The corresponding fits (red solid line) are obtained by fitting the distribution to a log-normal function.

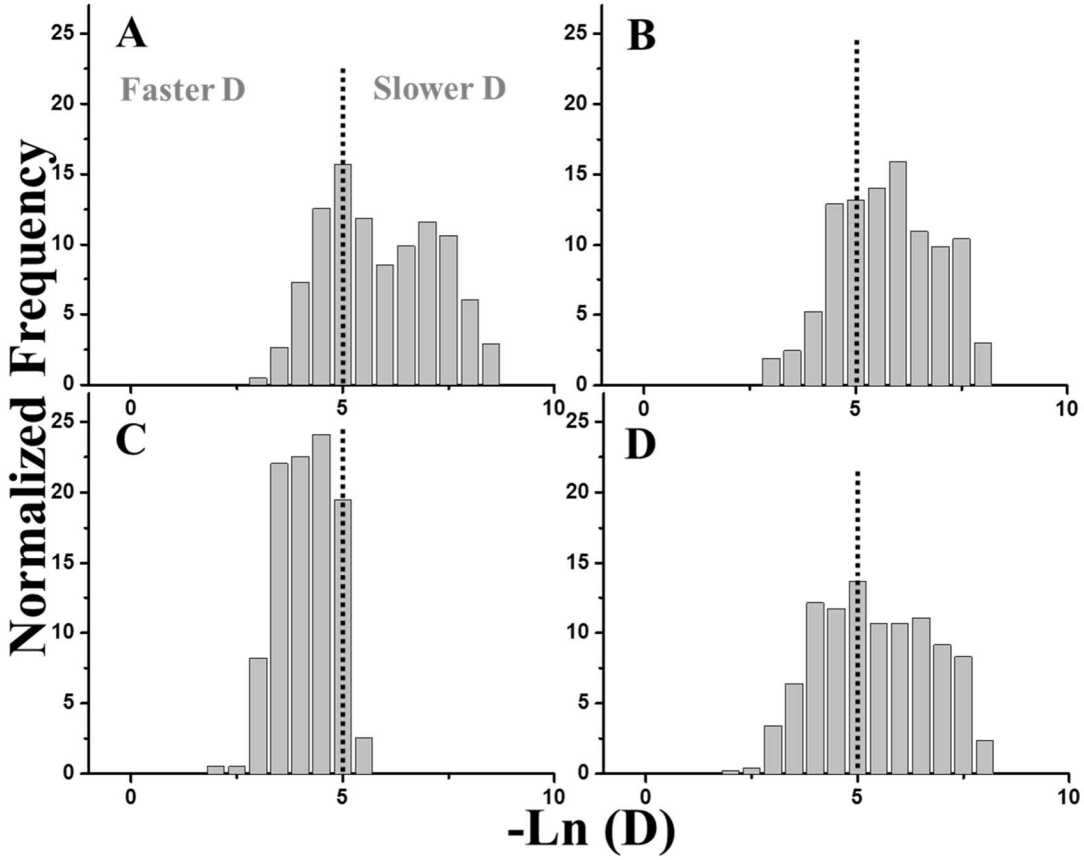


**Figure S3.9.** Histograms of diffusion coefficients for the confined trajectories (inside domains of confined diffusion) of HA-RAGE in the GM07373 cell membrane treated with: (A) No treatment; (B) 5 mM MβCD to extract cholesterol from the membrane; (C) 62% MGO-BSA and (D) 62% MGO-BSA and 5 mM MβCD. The diffusion coefficient is plotted as the negative natural logarithm. The dotted line is shown for clarity in comparing the changes in the distribution.

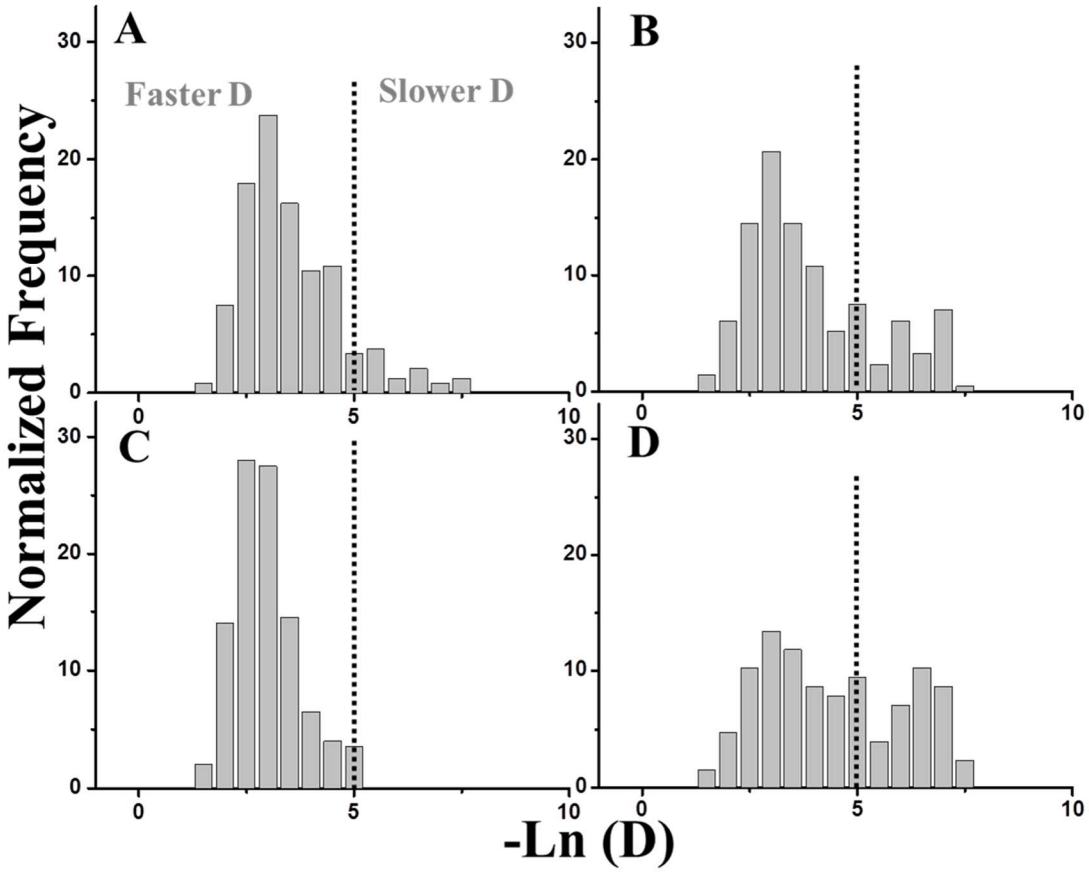


**Figure S3.10.** Histograms of diffusion coefficients for the confined trajectories (outside domains of confined diffusion) of HA-RAGE in the GM07373 cell membrane treated with: (A) No treatment; (B) 5 mM MβCD to extract cholesterol from the membrane; (C) 62% MGO-BSA and (D) 62% MGO-BSA and 5 mM MβCD. The diffusion coefficient is plotted as the negative natural logarithm. The dotted line is shown for clarity in comparing the changes in the distribution.

**References for supporting information for Chapter 3**

[1] M. Neeper, A.M. Schmidt, J. Brett, S.D. Yan, F. Wang, Y.C. Pan, K. Elliston, D. Stern, A. Shaw, Cloning and expression of a cell surface receptor for advanced glycosylation end products of proteins, *J Biol Chem*, 267 (1992) 14998-15004.

[2] A. Syed, Q. Zhu, E. Smith, Lateral Diffusion and Signaling of Receptor for Advanced Glycation End-products (RAGE): A Receptor Involved in Chronic Inflammation, *Eur Biophys J*, Submitted (2016).

[3] H. Towbin, T. Staehelin, J. Gordon, Electrophoretic transfer of proteins from polyacrylamide gels to nitrocellulose sheets: procedure and some applications, *Proc Natl Acad Sci U S A*, 76 (1979) 4350-4354.

[4] P.T. Matsudaira, Strategies for obtaining partial amuni acid sequence data. In a practical guide to protein and peptide purification for microsequencing, in, Academic Press, New York, 1989, pp. 29-30.

[5] G. Vistoli, D. De Maddis, A. Cipak, N. Zarkovic, M. Carini, G. Aldini, Advanced glycoxidation and lipoxidation end products (AGEs and ALEs): an overview of their mechanisms of formation, *Free Radic Res*, 47 Suppl 1 (2013) 3-27.

# CHAPTER 4. LATERAL DIFFUSION AND SIGNALING OF RECEPTOR FOR ADVANCED GLYCATION END-PRODUCTS (RAGE): A RECEPTOR INVOLVED IN CHRONIC INFLAMMATION

Modified from a publication on the *European Biophysics Journal*

Aleem Syed[1], Qiaochu Zhu[1] and Emily A. Smith*

Department of Chemistry, Iowa State University, 1605 Gilman Hall, Ames, IA 50010

[1] These authors have contributed equally to the work.

## 4.1 Abstract

Membrane diffusion is one of the key mechanisms in the cellular function of receptors. The signaling of receptor for advanced glycation end-products (RAGE) has been extensively studied in the context of several pathological conditions, however, very little is known about RAGE diffusion. To fill this gap, RAGE lateral diffusion is probed in native, cholesterol depleted and cytoskeleton altered cellular conditions. In native GM07373 cellular conditions, RAGE has a 90% mobile fraction and an average diffusion coefficient of 0.3 $\mu m^2/s$. When depolymerization of the actin cytoskeleton is inhibited with the small molecule Jasplakinolide (Jsp), the RAGE mobile fraction and diffusion coefficient decrease by 22% and 37%, respectively. In contrast, depolymerizing the filamentous actin cytoskeleton using the small molecule cytochalasin D (CD) does not alter the RAGE diffusion properties. There is a 70% and 50% decrease in phosphorylation of extracellular signal-regulated kinase (p-ERK) when the actin cytoskeleton is disrupted by CD or Jsp in RAGE expressing GM07373 cells. Disrupting the actin cytoskeleton in GM07373 cells that do not express detectable amounts of RAGE results in no change in p-ERK. Cholesterol depletion results in no statistically significant change in the diffusion properties of RAGE or p-ERK. This work

presents a strong link between the actin cytoskeleton and RAGE diffusion and downstream signaling, and serves to further our understanding of the factors influencing RAGE lateral diffusion.

## 4.2 Introduction

Lateral diffusion of membrane proteins is often interrelated with their cellular signaling and functions in the cell membrane [1-3]. The receptor for advanced glycation endproducts (RAGE) is a transmembrane protein that belongs to the immunoglobulin (Ig) superfamily. Many RAGE ligands have been identified, including advanced glycation endproducts (AGEs), S100 proteins, high mobility group box 1 (HMGB1), and amyloid-β fibrils [4-8]. RAGE and its signaling are associated with many disease states, including some types of cancer, retinal disease, cardiovascular disease, Alzheimer's disease, respiratory disorders, chronic inflammation and diabetic complications [9-15]. RAGE is reported to activate various signaling cascades, including mitogen-activated protein kinases (MAPKs), Rac/Cdc42 and Janus kinases (JAK)/signal transducers and activators of transcription (STATs) and NF-κB [16-21]. Through these signaling pathways, RAGE influences cell survival, motility and the inflammatory response. Even though RAGE signaling has been studied extensively in different disease states, very little is reported regarding RAGE diffusion in the cell membrane. The goal of the current study is to investigate the lateral diffusion and cellular signaling of RAGE in the endothelial cell membrane and to study the effects of cholesterol depletion and alterations to the actin cytoskeleton on these properties.

Cholesterol and the actin cytoskeleton play an important role in the organization of the cell membrane. Functional domains in the cell membrane, known as lipid rafts or lipid nanodomains, contain about 3 to 5-fold excess cholesterol compared to neighboring regions

of bilayer [22-25]. These functional domains act as platforms for localizing and signaling of many membrane proteins. Altering membrane cholesterol levels has been reported to affect the organization and signaling of a number of receptors [22, 26-30]. The actin cytoskeleton serves as a structural element that can affect the functionality of membrane proteins, including their oligomerization and transmembrane signaling [31].

Both cholesterol and the actin cytoskeleton have been reported to play a key role in RAGE functions. For example Reddy *et al.* showed cholesterol depletion inhibited the S100-induced effects involving RAGE in vascular smooth muscle cells and that intact caveolae are necessary for RAGE signaling [32]. RAGE has also been reported to be part of functional cholesterol-enriched domains in neural endothelial cells [33, 34]. Xiong *et al.* showed that the actin cytoskeleton played a pivotal role in RAGE-mediated plasma membrane plasticity in a human umbilical vein endothelial cell line [35]. They found that RAGE over expression reorganizes filamentous actin (F-actin) by increasing β-catenin levels, resulting in inhibition of membrane sealing. Although it is evident that cholesterol and the actin cytoskeleton affect some RAGE functions, possible roles in affecting RAGE lateral diffusion remain unknown.

In this study, we have genetically fused monomeric red fluorescent protein (mRFP) to the C-terminus of RAGE and measured its lateral diffusion using fluorescence recovery after photobleaching (FRAP) in GM07373 endothelial cells. In FRAP, a small area on the cell membrane is photobleached with a focused laser beam and the fluorescence recovery from the diffusion of neighboring fluorescent molecules into the photobleached spot is recorded over time. Several models have been constructed to extract diffusion parameters such as the immobile population, diffusion coefficient and time-dependency of the diffusion [36, 37]. RAGE diffusion at native, cholesterol depleted and altered actin cytoskeleton conditions have

been studied. Methyl-β-cyclodextrin (MβCD) was used to deplete cellular cholesterol. The actin cytoskeleton was altered using cytoskeletal drugs cytochalasin D (CD) and Jasplakinolide (Jsp). Finally, signaling was measured by quantifying the phosphorylation of extracellular-signal-regulated kinase (p-ERK) at native and altered cellular conditions.

## 4.3 Materials and Methods

### Cell culture

All experiments were performed using bovine artery GM07373 endothelial cells (Coriell Institute Biorepositories, Camden, NJ). GM07373 cells were grown in complete growth medium consisting of Dulbecco's modified Eagle's medium (DMEM) (Sigma-Aldrich, St. Louis, MO), 10% fetal bovine serum (FBS) (Irvine Scientific, Santa Ana, CA) and 12.5 mM Streptomycin and 36.5 mM Penicillin (Fisher Scientific, Pittsburgh, PA) in a water-jacketed $CO_2$ incubator (Thermo Scientific, Waltham, MA). Cells were sub-cultured using 0.25% (w/v) trypsin-EDTA (Life Technology, Carlsbad, CA) solution every two days. All transfected GM07373 cells were established to express respective recombinant proteins stably before any microscopy or molecular biology experiments were performed. Plasmid and transfection details are in the supplementary information.

### Western blotting

GM07373 cells expressing RAGE (GM07373-RAGE) or RAGE-mRFP (GM07373-RAGE-mRFP) were cultured to 100% confluence and rinsed with ice cold phosphate buffered saline (PBS). Cells were lysed with RIPA buffer (150 mM sodium chloride, 1.0% NP-40 detergent, 0.5% sodium deoxycholate, 0.1% SDS, 50 mM Tris, pH 8.0) with Halt™ protease inhibitor cocktail (1×, Thermo Scientific, Rockford, IL). After the initial lysis treatment, cells were passed through a 21 gauge needle to ensure complete cell lysis. The

protein mixture was first separated on the NuPAGE® Novex® 4-12% Bis-Tris protein gel (Life Technology, Eugene, OR) and then electro blotted onto Immun-Blot® LF PVDF membrane (Bio-Rad, Hercules, CA) as described previously [38, 39]. The PVDF membrane was probed following the manufacturer's protocol (Bio-Rad). Antibodies used for probing were: anti-RAGE rabbit (H-300, Santa Cruz Biotechnology), anti-RFP rabbit (Life Technology), anti-Vinculin goat (sc-7649, Santa Cruz Biotechnology), anti-Actin rabbit (sc-1616-R, Santa Cruz Biotechnology), anti-p-ERK rabbit (Tyr 204, sc-101761, Santa Cruz Biotechnology), anti-total-ERK 1/2 mouse (sc-514302, Santa Cruz Biotechnology). The labeled secondary antibodies were Alexa Fluor 647 goat anti-rabbit (Life technologies), Alexa Fluor 488 donkey anti-goat (Life technologies), Alexa Fluor 488 goat anti-mouse (Life technologies). Fluorescence was measured on a Typhoon FLA 9500 variable mode laser scanner (GE Healthcare, Waukesha, WI). The total-ERK and vinculin protein bands were used as a loading control in Western blot experiments. The fluorescence intensities were calculated from the 42 kDa band of p-ERK divided by the 42 kDa band of total-ERK or the 42 kDa band of actin divided by the 130 kDa band of vinculin. The 42 kDa band of ERK was used since it has a stronger intensity than the 44 kDa ERK band. All experiments were performed in triplicate unless otherwise noted in figure legends. Reported p values were calculated using the Student's t-test with a two-tailed homoscedastic distribution. Protein sequences were analyzed by mass spectrometry as reported in the supplemental information.

**FRAP sample preparation**

Sterile glass bottom culture dishes were made by attaching a cover glass (22mm × 22mm, No. 1.5, Corning Inc., Corning, NY) to the bottom of a polystyrene petri dish (35mm × 10mm, Fisher Scinetific) containing a pre-drilled 3/4 inch diameter hole as described previously [40]. GM07373-RAGE or GM07373-RAGE-mRFP cells were sub-cultured onto

the culture dishes two days before the experiment. Cells were either used without further treatment or treated at 37 ºC with MβCD (Sigma-Aldrich, 5mM, in serum free DMEM for 30 minutes) to deplete the cholesterol or with CD (Sigma-Aldrich, 10 µM, in serum free DMEM for 60 minutes) or with Jsp (Santa Cruz Biotechnology, 3µM, in serum free DMEM for 30 minutes) to alter the actin cytoskeleton as previously reported [29, 41, 42] before the FRAP experiments.

**FRAP Microscopy**

All FRAP experiments were performed on a Nikon Eclipse TE2000U inverted microscope (Nikon, Melville, NY) which was equipped with an oil-immersion objective (100×, Apo TIRF, 1.49 numerical aperture). The microscope was housed in a home built $0.9\times0.6\times0.5$ $m^3$ Plexiglas box containing a heat source to maintain a 36 ± 2 ºC at the sample throughout the experiment. Fluorescence was excited with a mercury lamp (X-cite 120 PC, EXFO Photonic Solutions Inc., Mississauga, Ontario, Canada) operating at 25% of the power and an excitation filter (HQ545/30x, Chroma Technology Corp., Bellows Falls, VT). The resulting fluorescence emission was collected through an emission filter (HQ620/60x, Chroma Technology Corp.). For photobleaching a region of the cell membrane, a 488-nm laser was directed to the sample with a dichroic mirror (Q495lp, Chroma Technology Corp.). The laser power and photobleaching spot diameter at the sample were 10 mW and 4.0 µm, respectively. A LabView program (National Instruments, Austin, TX) was developed to control a shutter (Thorlabs, Jessup, MD) in the laser path. The photobleaching time was 2 msec. Fluorescence images were recorded using a PhotonMAX 512B EMCCD camera (Princeton Instruments, Trenton, NJ) and Winview (Photometric, Tucson, AZ) image acquisition software. Ten pre-photobleach and 100 post-photobleach images were collected with a time resolution of 410 ms per image. Dark-state formation in mRFP is expected to

have a negligible impact on the FRAP data collected on this timescale. Data collection was completed within 1 h after adding imaging medium (pH=7.2, 155 mM NaCl, 5 mM KCl, 2 mM $CaCl_2$, 1 mM $MgCl_2$, 2 mM $NaH_2PO_4$, 10 mM HEPES and 10 mM Glucose) to the cells.

**FRAP analysis**

The fluorescence images collected pre-photobleach and post-photobleach were analyzed with ImageJ (version 1.48, National Institute of Health) software. The fluorescence intensity from three regions of interest (ROIs) was extracted for each image in the series of 110 images. The ROIs were classified as the photobleached region (an area on the plasma membrane illuminated by the laser spot), the non-photobleached region (an area on the plasma membrane away from the photobleached region), and the background (an area where there was no cell present in the field of view). Fluorescence recovery curves were constructed with a three-step process: (i) the background intensity was subtracted from fluorescence intensities in the photobleached ROI, the resulting curves were normalized with the fluorescence intensities from (ii) the non-photobleached ROI and (iii) the average pre-photobleached intensity from the subsequently photobleached region to account for the lamp intensity fluctuations as well as photobleaching during the image acquisition period as described by Phair *et al.* [43]. Fluorescence recovery curves were analyzed and the results were averaged over 24 to 53 cells for each data set. The number of cells measured was lower for Jsp, CD and MβCD data sets. These treatments result in a smaller average spread cell diameter, which reduces the number of cells that can be analyzed by FRAP compared to the untreated cells. Mobile fractions (*MF*) were calculated using following equation,

$$MF = \frac{F_\infty - F_0}{F^0 - F_0} \times 100 \qquad (1)$$

Where $F_0$ is the intensity immediately after photobleaching, $F^0$ is the pre-photobleaching intensity and $F_\infty$ is the final intensity (i.e., in image 110), where all fluorescence intensities refer to the values from the fluorescence recovery curves. Each fluorescence recovery curve was further fit with below equation using IGOR Pro V 6.32A (WaveMetrics Inc., Lake Oswego, OR) to measure the time dependency of the fluorescence recovery as well as diffusion coefficients [36].

$$F(t) = \frac{F_0 + F_\infty \left(\frac{t}{\tau}\right)^{\alpha}}{1 + \left(\frac{t}{\tau}\right)^{\alpha}} \quad (2)$$

Where $F(t)$ is the fluorescence intensity at time $t$, $\alpha$ is the time exponent and $\tau$ is time for 50% fluorescence recovery. Diffusion coefficients were calculated using below equation.

$$D = \frac{\omega^2}{4\tau^{\alpha} t^{\alpha-1}} \quad (3)$$

Where $D(t)$ is the diffusion coefficient at time $t$ and $\omega$ is the radius of the photobleached spot. The statistical significance of all reported data sets was calculated using first the F-test at the 95% confidence level and then the homoscedastic/heteroscedastic (as determined from the F-test) Student's t-test with a two-tailed distribution. The resulting p values that indicate statistical differences are reported in Figure 4.7; statistical differences at the 95% confidence level (i.e., p values below 0.05) are considered significant. Diffusion parameters are presented as box-and-whisker plots. For box-and-whisker plots, the boundary of the box shows the twenty-fifth and seventy-fifth quartiles. A line and a triangle within the box indicate the median and the mean, respectively. Whiskers above and below the boxes are 1.5 times the interquartile range.

**Actin cytoskeleton staining**

Cells were sub-cultured onto glass-bottom petri dishes and allowed to spread in the incubator for two days before the experiment. Cells were treated as described above with 5 mM MβCD, 10 μM CD, or 3 μM Jsp before the actin cytoskeleton was stained for fluorescence imaging. The staining protocol was described previously [44]. Briefly, cells were fixed with 4% (w/v) paraformaldehyde in PBS for 10 minutes. Triton X-100 (0.1% (v/v) in PBS) was used for cell membrane permeabilization. Blocking was performed using bovine serum albumin (1% (w/v) in PBS) for 5 minutes. Cells were further incubated with Atto 647N conjugated phalloidin (Sigma-Aldrich) to stain the F-actin overnight at 4 °C. Stained cells were rinsed with imaging medium before imaging using the Nikon Eclipse TE2000U inverted microscope described above. The actin cytoskeleton was further quantified to measure the alignment in the actin fibers in 21 to 41 cells. Alignment was calculated using an ImageJ plugin, FibrilTool, as described previously [45].

## 4.4 Results and Discussion

**Characterization of RAGE and RAGE-mRFP Expression**

The primary goal of this study is to probe the lateral diffusion of RAGE in the GM07373 cell membrane in order to characterize the role of the actin cytoskeletal and cholesterol in altering RAGE diffusion. To achieve this goal, plasmids were transfected into GM07373 cells to stably express full-length RAGE or RAGE-mRFP. RAGE or RAGE-mRFP expression was confirmed by Western blot analysis of cell lysates as shown in Figure 4.1. A protein band corresponding to RAGE at ~55 kDa (band 1, Figure 4.1) was observed in the GM07373-RAGE cell lysate (lane b, Figure 4.1) but not in the GM07373 cell lysate (lane a, Figure 4.1). Surprisingly, the GM07373-RAGE-mRFP cell lysate (lane c, Figure 4.1)

showed three bands in the 60 to 80 kDa molecular weight range after probing the membrane with the RAGE primary antibody. Bands 1 to 4 were positive for RAGE peptides as measured by mass spectrometry. After the PVDF membrane was probed with a polyclonal mRFP antibody, only a single band was observed from the GM07373-RAGE-mRFP cell lysate (band 5, Figure 4.1) near the molecular weight of band 3. It was confirmed by fluorescence imaging of the PVDF membrane that fluorescence was measured only at the location of band 5, thus RAGE-containing bands 2 and 4 do not contribute to the fluorescence microscopy results reported below.

Phosphorylation of extracellular-signal-regulated kinase (p-ERK) was used as a marker for downstream RAGE signaling [46, 47]. There was no statistically significant difference in p-ERK levels in cells expressing RAGE or RAGE-mRFP (Figure 4.2), indicating that the mRFP tag on RAGE did not alter p-ERK signaling in GM07373 cells.

**RAGE-mRFP diffusion in the native GM07373 cell membrane**

FRAP experiments on GM07373 cells expressing RAGE-mRFP were performed and the average recovery curve from 24-53 cells is shown in Online Resource 1 (Figure S4.1). Each replicate curve was individually fit to the time-dependent diffusion model with an immobile fraction (i.e., all parameters $\alpha$, $F_0$, $F_\infty$ and $\tau$ in equation 2 were allowed to vary) as described by Federer *et al.* [36]. The time exponent ($\alpha$) from the fit parameters provides information on the nature of the mode of diffusion. An $\alpha$ value of 1 indicates time-independent Brownian diffusion, whereas a value less than 1 indicates time-dependent diffusion. The average $\alpha$ value measured for RAGE-mRFP was 0.9 (Figure 4.7). The average mobile fraction was 90% and the average diffusion coefficient was 0.3 $\mu m^2/s$ for RAGE-mRFP at native cellular conditions. While FRAP provides a measure of the average diffusion properties of RAGE-mRFP, it is known that RAGE diffusion is heterogeneous [48]. For

example, when the diffusion coefficient is measured one receptor at a time across 100 receptors, the diffusion coefficient varies by over 4 orders of magnitude. The heterogeneity in RAGE diffusion is not detectable with the ensemble FRAP method. On the other hand, FRAP measurements yield the fraction of mobile RAGE, which has not been possible to measure with other analysis techniques [48].

**Alterations to the F-actin cytoskeleton alter RAGE-mRFP diffusion properties measured by FRAP**

To study the possible effect of the actin cytoskeleton on RAGE lateral diffusion, the actin cytoskeleton was altered with two drugs, CD and Jsp. CD depolymerizes the filamentous actin cytoskeleton and prevents repolymerization by binding to actin monomers [49]. Jsp binds with filamentous actin and inhibits depolymerization [50]. Atto 647N conjugated phalloidin was used to measure the effect of CD and Jsp on the actin cytoskeleton in GM07373-RAGE cells as shown in Figure 4.3. In the native GM07373 cells, the actin cytoskeleton staining generated partially aligned fibers with a well-defined cell boundary as shown in Figure 4.3a. After the CD treatment, the actin structure was significantly altered and no clear cell boundary was observed (Figure 4.3c). Jsp binds to the actin cytoskeleton in competition with the Atto 647N conjugated phalloidin [51]. Hence, Atto 647N phalloidin actin cytoskeleton staining was diminished for Jsp treated cells (Figure 4.3d). There was no change in the actin expression as measured from Western blot analysis of the cell lysate treated with CD or Jsp (Figure 4.4).

RAGE-mRFP diffusion parameters were measured for CD or Jsp treated cells. The RAGE-mRFP mobile fraction and diffusion coefficient were decreased by 22% and 37%, respectively, when the actin cytoskeleton was altered with Jsp (Figure 4.7). In contrast, CD treatment does not alter the RAGE diffusion properties. Jsp and CD have opposite effects on

the polymerization of the actin cytoskeleton. Jsp hinders depolymerization, whereas CD depolymerizes the actin filaments. Jsp results in less mobile and slower RAGE, suggesting an actin cytoskeleton fixed in a polymerized state slows RAGE diffusion and reduces the mobile fraction. Surprisingly, CD treatment to depolymerize the actin cytoskeleton does not statistically increase RAGE mobility as measured by FRAP; although it is noteworthy that prior to altering the actin cytoskeleton RAGE diffusion is already relatively unhindered with a large mobile fraction and nearly Brownian behavior as indicated by the $\alpha$ value.

To understand if RAGE diffusion properties are linked to downstream signaling, phosphorylation of ERK (p-ERK) was measured in both GM07373 and GM07373-RAGE cells after CD and Jsp treatment. p-ERK was decreased by 70% and 50% in GM07373-RAGE cells when the actin cytoskeleton was disrupted with CD and JSP, respectively (Figure 4.5a and 4.5b). There was no statistically significant change in p-ERK observed in GM07373 cells lacking detectable RAGE expression after CD or Jsp treatment (Figure 4.5c and 4.5d). This indicates that the downstream signaling of RAGE is altered when the actin cytoskeleton is disrupted, regardless of the effects disrupting the actin cytoskeleton has on RAGE diffusion.

To investigate the effect of cholesterol on the lateral diffusion of RAGE-mRFP, cholesterol was depleted using MβCD. The total free cholesterol was depleted by 45% and no statistically significant change in the endogenous cholesterol ester was observed when cells were incubated with 5 mM MβCD as measured by Amplex® Red cholesterol quantification assay (Figure 4.6a). The diffusion parameters statistically unchanged for RAGE-mRFP (Figure 4.7). There was also no change in p-ERK measured after cholesterol depletion from both GM07373-RAGE cells and GM07373 (Figure 4.6b and 4.6d). These

conclusions are valid in the absence of RAGE ligand. In the presence of ligand, RAGE signaling may be dependent on cholesterol as previously reported [32].

It has been previously reported that a change in membrane cholesterol not only affects the cell membrane structure but also has a global effect, including reorganization of the actin structure [52]. This appears to be valid in GM07373-RAGE cells (Figure 4.3a and 4.3b). A significant 40% decrease in the actin fiber alignment was measured after cholesterol depletion in both the GM07373-RAGE and GM07373 cell lines. No change in the actin expression was observed with cholesterol depletion (Figure 4.6). These observations indicate that cholesterol depletion affects the actin cytoskeleton organization, but the cholesterol-depletion-induced changes to the actin cytoskeleton alignment are not associated with changes in RAGE diffusion properties.

In summary, RAGE-mRFP diffuses in the cell membrane with a large mobile fraction at native GM07373 cellular conditions. The depolymerization of the actin cytoskeleton plays a role in how RAGE diffuses in the membrane, and more generally, the actin cytoskeleton polymerization dynamics alter the downstream signaling of RAGE. Even though there is a significant change in the actin cytoskeleton alignment as revealed by phalloidin staining, cholesterol depletion has no effect on RAGE lateral diffusion as measured by FRAP or signaling as measured by p-ERK. The combined data point to an important role for actin depolymerization in the diffusion properties of RAGE and a link between the actin cytoskeleton and RAGE-mediated p-ERK signaling.

**Acknowledgements**

This work was supported by the National Science Foundation (CHE- 1412084). The authors thank Joel Nott of the protein facility at Iowa State University for help with mass

spectrometry, and Dipak Mainali and Chamari Wijesoorya for their assistance with cell culture.

## 4.5 References

[1] D. Axelrod, Lateral motion of membrane proteins and biological function, *Journal of Membrane Biology*, 75 (1983) 10.

[2] P. Ronchi, S. Colombo, M. Francolini, N. Borgese, Transmembrane domain-dependent partitioning of membrane proteins within the endoplasmic reticulum, *J Cell Biol*, 181 (2008) 105-118.

[3] S. Ganguly, T.J. Pucadyil, A. Chattopadhyay, Actin cytoskeleton-dependent dynamics of the human serotonin1A receptor correlates with receptor signaling, *Biophys J*, 95 (2008) 451-463.

[4] A. Taguchi, D.C. Blood, G. del Toro, A. Canet, D.C. Lee, W. Qu, N. Tanji, Y. Lu, E. Lalla, C. Fu, M.A. Hofmann, T. Kislinger, M. Ingram, A. Lu, H. Tanaka, O. Hori, S. Ogawa, D.M. Stern, A.M. Schmidt, Blockade of RAGE-amphoterin signalling suppresses tumour growth and metastases, *Nature*, 405 (2000) 354-360.

[5] A.M. Schmidt, M. Vianna, M. Gerlach, J. Brett, J. Ryan, J. Kao, C. Esposito, H. Hegarty, W. Hurley, M. Clauss, et al., Isolation and characterization of two binding proteins for advanced glycosylation end products from bovine lung which are present on the endothelial cell surface, *J Biol Chem*, 267 (1992) 14987-14997.

[6] E. Leclerc, G. Fritz, S.W. Vetter, C.W. Heizmann, Binding of S100 proteins to RAGE: an update, *Biochim Biophys Acta*, 1793 (2009) 993-1007.

[7] S.D. Yan, X. Chen, J. Fu, M. Chen, H. Zhu, A. Roher, T. Slattery, L. Zhao, M. Nagashima, J. Morser, A. Migheli, P. Nawroth, D. Stern, A.M. Schmidt, RAGE and amyloid-beta peptide neurotoxicity in Alzheimer's disease, *Nature*, 382 (1996) 685-691.

[8] M. Koch, S. Chitayat, B.M. Dattilo, A. Schiefner, J. Diez, W.J. Chazin, G. Fritz, Structural basis for ligand recognition and activation of RAGE, *Structure*, 18 (2010) 1342-1352.

[9] C.D. Logsdon, M.K. Fuentes, E.H. Huang, T. Arumugam, RAGE and RAGE ligands in cancer, *Curr Mol Med*, 7 (2007) 777-789.

[10] G.R. Barile, A.M. Schmidt, RAGE and its ligands in retinal disease, *Curr Mol Med*, 7 (2007) 758-765.

[11] G. Basta, Receptor for advanced glycation endproducts and atherosclerosis: From basic mechanisms to clinical implications, *Atherosclerosis*, 196 (2008) 9-21.

[12] S.D. Yan, A. Bierhaus, P.P. Nawroth, D.M. Stern, RAGE and Alzheimer's disease: a progression factor for amyloid-beta-induced cellular perturbation?, *J Alzheimers Dis*, 16 (2009) 833-843.

[13] R. Briot, J.A. Frank, T. Uchida, J.W. Lee, C.S. Calfee, M.A. Matthay, Elevated levels of the receptor for advanced glycation end products, a marker of alveolar epithelial type I cell injury, predict impaired alveolar fluid clearance in isolated perfused human lungs, *Chest*, 135 (2009) 269-275.

[14] M.A. Hofmann, S. Drury, C. Fu, W. Qu, A. Taguchi, Y. Lu, C. Avila, N. Kambham, A. Bierhaus, P. Nawroth, M.F. Neurath, T. Slattery, D. Beach, J. McClary, M. Nagashima, J. Morser, D. Stern, A.M. Schmidt, RAGE mediates a novel proinflammatory axis: a central cell surface receptor for S100/calgranulin polypeptides, *Cell*, 97 (1999) 889-901.

[15] A. Bierhaus, P.P. Nawroth, Multiple levels of regulation determine the role of the receptor for AGE (RAGE) as common soil in inflammation, immune responses and diabetes mellitus and its complications, *Diabetologia*, 52 (2009) 2251-2263.

[16] H.M. Lander, J.M. Tauras, J.S. Ogiste, O. Hori, R.A. Moss, A.M. Schmidt, Activation of the receptor for advanced glycation end products triggers a p21(ras)-dependent mitogen-activated protein kinase pathway regulated by oxidant stress, *J Biol Chem*, 272 (1997) 17810-17814.

[17] H.J. Huttunen, C. Fages, H. Rauvala, Receptor for advanced glycation end products (RAGE)-mediated neurite outgrowth and activation of NF-kappaB require the cytoplasmic domain of the receptor but different downstream signaling pathways, *J Biol Chem*, 274 (1999) 19919-19924.

[18] A. Hermani, B. De Servi, S. Medunjanin, P.A. Tessier, D. Mayer, S100A8 and S100A9 activate MAP kinase and NF-kappaB signaling pathways and trigger translocation of RAGE in human prostate cancer cells, *Exp Cell Res*, 312 (2006) 184-197.

[19] C.H. Yeh, L. Sturgis, J. Haidacher, X.N. Zhang, S.J. Sherwood, R.J. Bjercke, O. Juhasz, M.T. Crow, R.G. Tilton, L. Denner, Requirement for p38 and p44/p42 mitogen-activated protein kinases in RAGE-mediated nuclear factor-kappaB transcriptional activation and cytokine secretion, *Diabetes*, 50 (2001) 1495-1504.

[20] L. Wang, S. Li, F.B. Jungalwala, Receptor for advanced glycation end products (RAGE) mediates neuronal differentiation and neurite outgrowth, *J Neurosci Res*, 86 (2008) 1254-1266.

[21] S. Ghavami, I. Rashedi, B.M. Dattilo, M. Eshraghi, W.J. Chazin, M. Hashemi, S. Wesselborg, C. Kerkhoff, M. Los, S100A8/A9 at low concentration promotes tumor cell growth via RAGE ligation and MAP kinase-dependent pathway, *J Leukoc Biol*, 83 (2008) 1484-1492.

[22] L.J. Pike, Lipid rafts: bringing order to chaos, *J Lipid Res*, 44 (2003) 655-667.

[23] D. Lingwood, K. Simons, Lipid rafts as a membrane-organizing principle, *Science*, 327 (2010) 46-50.

[24] K. Simons, M.J. Gerl, Revitalizing membrane rafts: new tools and insights, *Nat Rev Mol Cell Biol*, 11 (2010) 688-699.

[25] J. Ando, M. Kinoshita, J. Cui, H. Yamakoshi, K. Dodo, K. Fujita, M. Murata, M. Sodeoka, Sphingomyelin distribution in lipid rafts of artificial monolayer membranes visualized by Raman microscopy, *Proc Natl Acad Sci U S A*, 112 (2015) 4558-4563.

[26] E.M. Adkins, D.J. Samuvel, J.U. Fog, J. Eriksen, L.D. Jayanthi, C.B. Vaegter, S. Ramamoorthy, U. Gether, Membrane mobility and microdomain association of the dopamine transporter studied with fluorescence correlation spectroscopy and fluorescence recovery after photobleaching, *Biochemistry*, 46 (2007) 10484-10497.

[27] N. Bag, S. Huang, T. Wohland, Plasma Membrane Organization of Epidermal Growth Factor Receptor in Resting and Ligand-Bound States, *Biophys J*, 109 (2015) 1925-1936.

[28] D.A. Brown, E. London, Functions of lipid rafts in biological membranes, *Annu Rev Cell Dev Biol*, 14 (1998) 111-136.

[29] N. Arora, A. Syed, S. Sander, E.A. Smith, Single particle tracking with sterol modulation reveals the cholesterol-mediated diffusion properties of integrin receptors, *Phys Biol*, 11 (2014) 066001.

[30] T.J. Pucadyil, A. Chattopadhyay, Role of cholesterol in the function and organization of G-protein coupled receptors, *Prog Lipid Res*, 45 (2006) 295-333.

[31] A. Kusumi, K.G. Suzuki, R.S. Kasai, K. Ritchie, T.K. Fujiwara, Hierarchical mesoscale domain organization of the plasma membrane, *Trends Biochem Sci*, 36 (2011) 604-615.

[32] M.A. Reddy, S.L. Li, S. Sahar, Y.S. Kim, Z.G. Xu, L. Lanting, R. Natarajan, Key role of Src kinase in S100B-induced activation of the receptor for advanced glycation end products in vascular smooth muscle cells, *J Biol Chem*, 281 (2006) 13685-13693.

[33] M.P. Lisanti, P.E. Scherer, J. Vidugiriene, Z. Tang, A. Hermanowski-Vosatka, Y.H. Tu, R.F. Cook, M. Sargiacomo, Characterization of caveolin-rich membrane domains isolated from an endothelial-rich source: implications for human disease, *J Cell Biol*, 126 (1994) 111-126.

[34] O. Sbai, T.S. Devi, M.A. Melone, F. Feron, M. Khrestchatisky, L.P. Singh, L. Perrone, RAGE-TXNIP axis is required for S100B-promoted Schwann cell migration, fibronectin expression and cytokine secretion, *J Cell Sci*, 123 (2010) 4332-4339.

[35] F. Xiong, S. Leonov, A.C. Howard, S. Xiong, B. Zhang, L. Mei, P. McNeil, S. Simon, W.C. Xiong, Receptor for advanced glycation end products (RAGE) prevents endothelial cell membrane resealing and regulates F-actin remodeling in a beta-catenin-dependent manner, *J Biol Chem*, 286 (2011) 35061-35070.

[36] T.J. Feder, I. Brust-Mascher, J.P. Slattery, B. Baird, W.W. Webb, Constrained diffusion or immobile fraction on cell surfaces: a new interpretation, *Biophys J*, 70 (1996) 2767-2773.

[37] E.J. van Zoelen, L.G. Tertoolen, S.W. de Laat, Simple computer method for evaluation of lateral diffusion coefficients from fluorescence photobleaching recovery kinetics, *Biophys J*, 42 (1983) 103-108.

[38] H. Towbin, T. Staehelin, J. Gordon, Electrophoretic transfer of proteins from polyacrylamide gels to nitrocellulose sheets: procedure and some applications, *Proc Natl Acad Sci U S A*, 76 (1979) 4350-4354.

[39] P.T. Matsudaira, Strategies for obtaining partial amuni acid sequence data. In a practical guide to protein and peptide purification for microsequencing, in, Academic Press, New York, 1989, pp. 29-30.

[40] D.W. Buster, J. Nye, J.E. Klebba, G.C. Rogers, Preparation of Drosophila S2 cells for light microscopy, *J Vis Exp*, (2010).

[41] U.E. Schwab, C.M. Ribeiro, H. Neubauer, R.C. Boucher, Role of actin filament network in Burkholderia multivorans invasion in well-differentiated human airway epithelia, *Infect Immun*, 71 (2003) 6607-6609.

[42] M.K. Shaw, L.G. Tilney, Induction of an acrosomal process in Toxoplasma gondii: visualization of actin filaments in a protozoan parasite, *Proc Natl Acad Sci U S A*, 96 (1999) 9095-9099.

[43] R.D. Phair, S.A. Gorski, T. Misteli, Measurement of dynamic protein binding to chromatin in vivo, using photobleaching microscopy, *Methods Enzymol*, 375 (2004) 393-414.

[44] A. Syed, M.D. Lesoine, U. Bhattacharjee, J.W. Petrich, E.A. Smith, The number of accumulated photons and the quality of stimulated emission depletion lifetime images, *Photochem Photobiol*, 90 (2014) 767-772.

[45] A. Boudaoud, A. Burian, D. Borowska-Wykret, M. Uyttewaal, R. Wrzalik, D. Kwiatkowska, O. Hamant, FibrilTool, an ImageJ plug-in to quantify fibrillar structures in raw microscopy images, *Nat Protoc*, 9 (2014) 457-463.

[46] H.J. Huttunen, J. Kuja-Panula, H. Rauvala, Receptor for advanced glycation end products (RAGE) signaling induces CREB-dependent chromogranin expression during neuronal differentiation, *J Biol Chem*, 277 (2002) 38635-38646.

[47] H. Zong, A. Madden, M. Ward, M.H. Mooney, C.T. Elliott, A.W. Stitt, Homodimerization is essential for the receptor for advanced glycation end products (RAGE)-mediated signal transduction, *J Biol Chem*, 285 (2010) 23137-23146.

[48] A. Syed, Q. Zhu, E.A. Smith, Ligand binding affinity and changes in the lateral diffusion of receptor for advanced glycation endproducts (RAGE), *Biochim Biophys Acta*, 1858 (2016) 3141-3149.

[49] J.F. Casella, M.D. Flanagan, S. Lin, Cytochalasin D inhibits actin polymerization and induces depolymerization of actin filaments formed during platelet shape change, *Nature*, 293 (1981) 302-305.

[50] I. Spector, F. Braet, N.R. Shochet, M.R. Bubb, New anti-actin drugs in the study of the organization and function of the actin cytoskeleton, *Microsc Res Tech*, 47 (1999) 18-37.

[51] M.R. Bubb, I. Spector, B.B. Beyer, K.M. Fosen, Effects of jasplakinolide on the kinetics of actin polymerization. An explanation for certain in vivo observations, *J Biol Chem*, 275 (2000) 5163-5170.

[52] J. Kwik, S. Boyle, D. Fooksman, L. Margolis, M.P. Sheetz, M. Edidin, Membrane cholesterol, lateral mobility, and the phosphatidylinositol 4,5-bisphosphate-dependent organization of cell actin, *Proceedings of the National Academy of Sciences*, 100 (2003) 13964-13969.

## 4.6 Figures and Tables

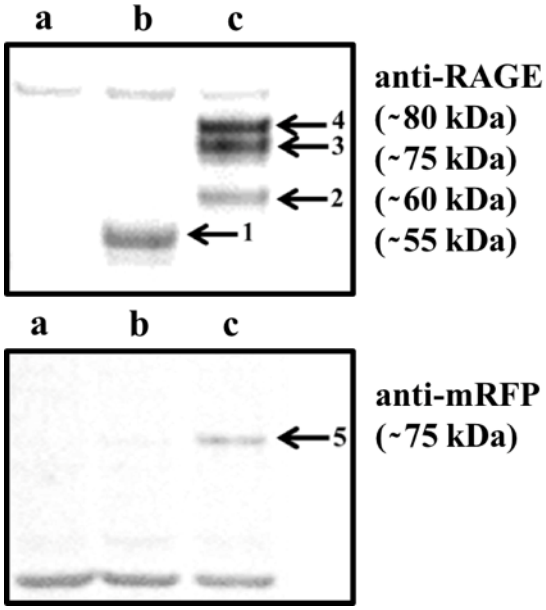


**Figure 4.1.** Western blot analysis of (a) GM07373 cell lysate, (b) GM07373-RAGE cell lysate, and (c) GM07373-RAGE-mRFP cell lysate. (Top) fluorescence image of the PVDF membrane probed with anti-RAGE antibody; (bottom) fluorescence image of the PVDF membrane probed with anti-mRFP antibody. Unlabeled bands (three upper bands in the top image and three lower bands in the bottom image) are present in all lanes and likely represent non-specific interactions of antibodies.

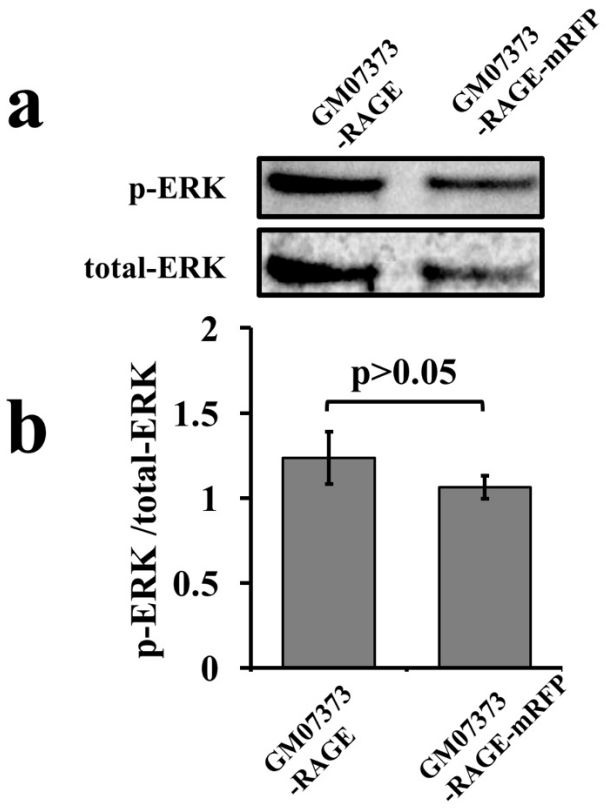


**Figure 4.2.** Western blot analysis of phosphorylation of ERK and total-ERK expression in the GM07373-RAGE cell lysate and GM07373-RAGE-mRFP cell lysate. (a) Fluorescence image of the PVDF membrane probed with anti-p-ERK or anti-total-ERK antibody. (b) Average (n = 3) fluorescence intensities of the 42 kDa band of p-ERK divided by the 42 kDa total-ERK band. Error bars represent one standard deviation.

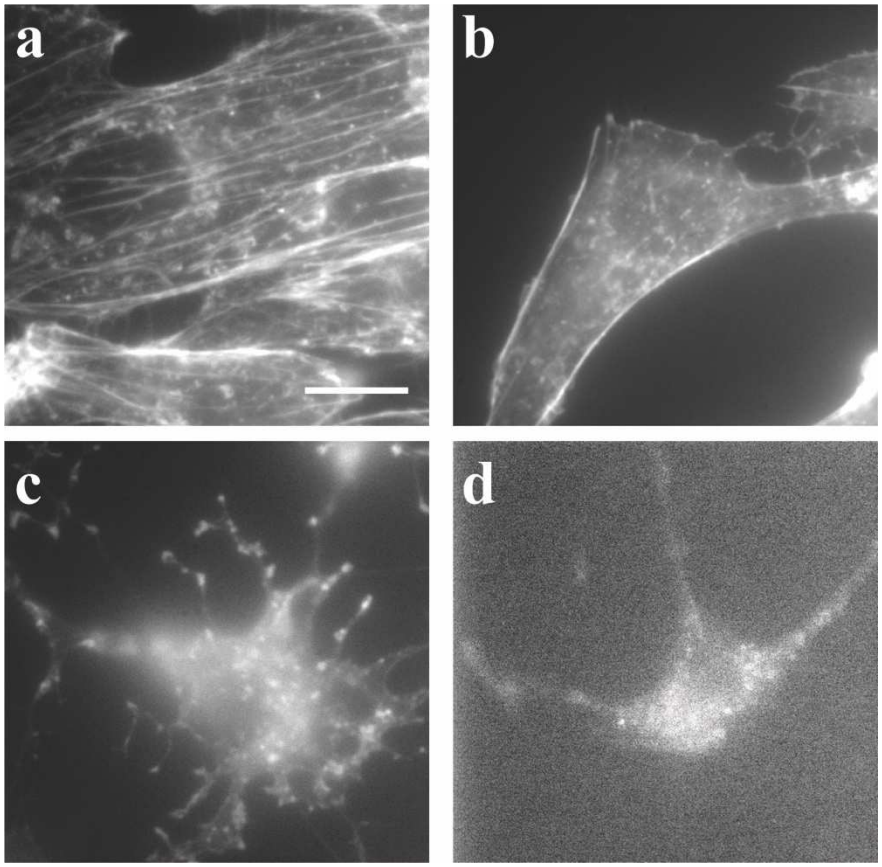


**Figure 4.3.** Fluorescence images of GM07373-RAGE cells with the actin cytoskeleton stained with Atto 647N conjugated phalloidin. (a) No treatment, (b) 5 mM methyl-β-cyclodextrin treatment, (c) 10 µM cytochalasin-D treatment, or (d) 3 µM Jasplakinolide treatment. The intensity scales are: (a) and (b) 1700 to 7000 intensity units, (c) 1500 to 3000 intensity units, and (d) 1500 to 1700 intensity units. The scale bar is 20 µm and is the same for all images.

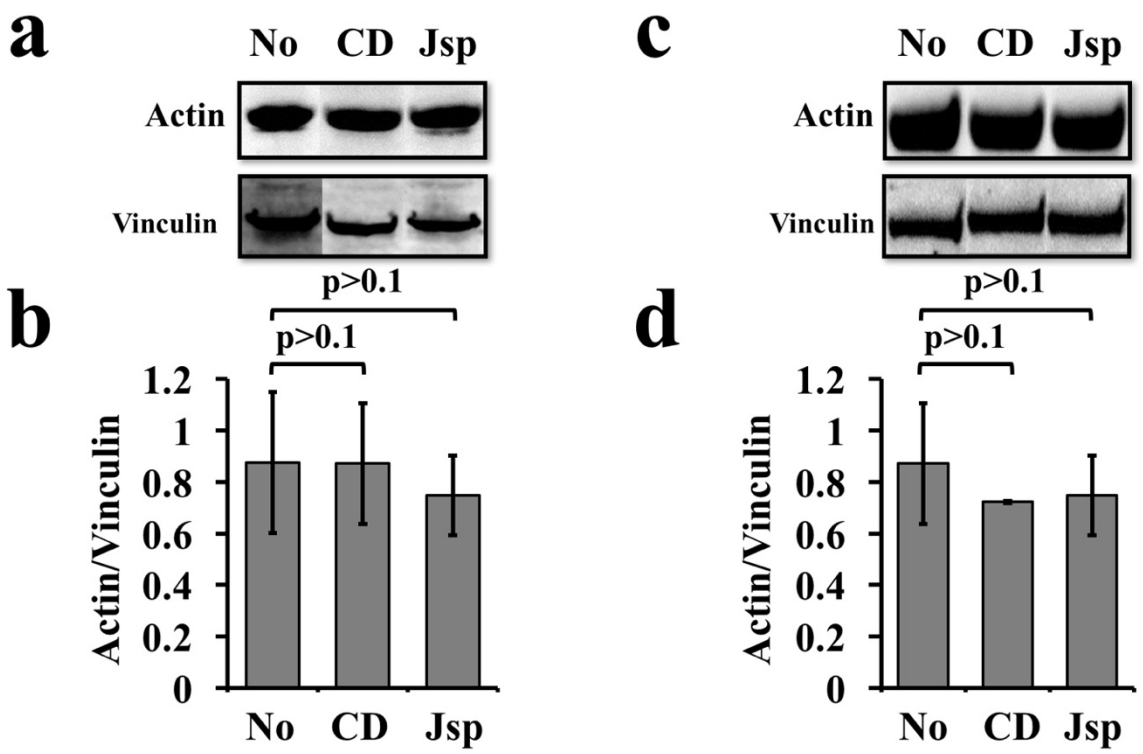


**Figure 4.4** Western blot analysis of actin expression in the (a, b) GM07373-RAGE and (c, d) GM07373 cell lysate with no treatment (No), 10 μM cytochalasin D (CD) treatment, or 3 μM Jasplakinolide (Jsp) treatment. (a, c) Fluorescence image of the PVDF membrane probed with anti-actin or anti-vinculin antibody. (b, d) Average (n = 3) fluorescence intensities of the actin band divided by the vinculin band. Error bars represent one standard deviation.

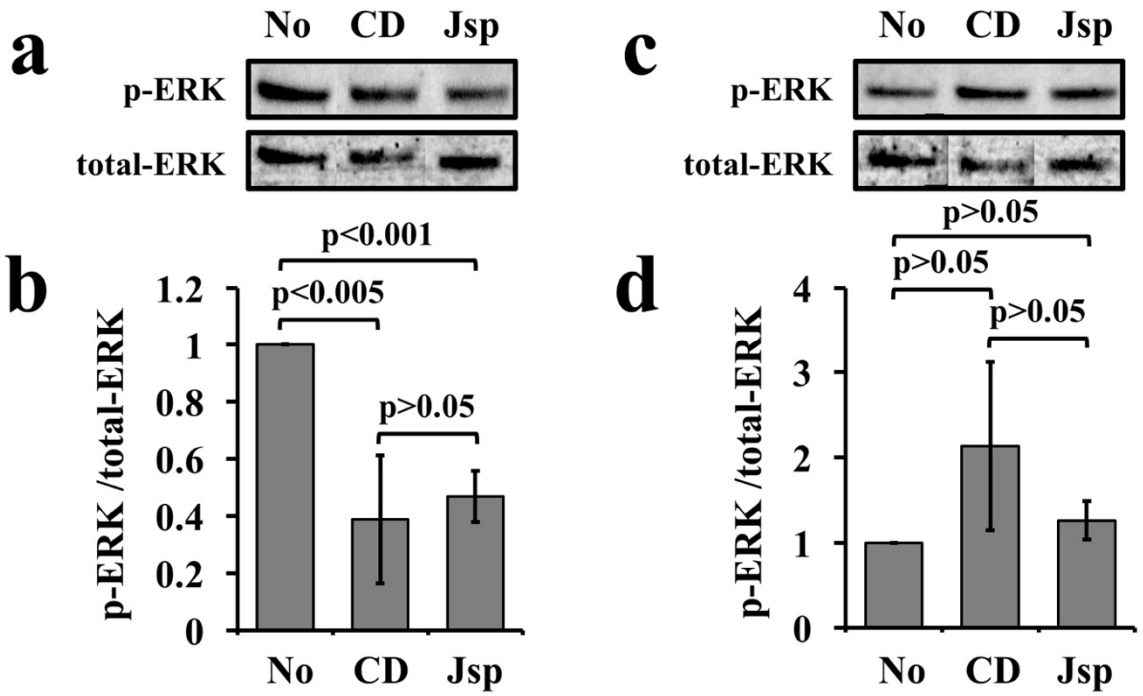


**Figure 4.5.** Western blot analysis of phosphorylation of ERK and total-ERK expression in the (a, b) GM07373-RAGE and (c, d) GM07373 cell lysate with no treatment (No), 10 µM cytochalasin D (CD) treatment, or 3 µM Jasplakinolide (Jsp) treatment. (a, c) Fluorescence image of the PVDF membrane probed with anti-p-ERK or anti-total-ERK antibody. (b, d) Average (n = 3) fluorescence intensities of the 42 kDa band of p-ERK divided by the 42 kDa total-ERK band. The band intensities were normalized to the no treatment band. Error bars represent one standard deviation.

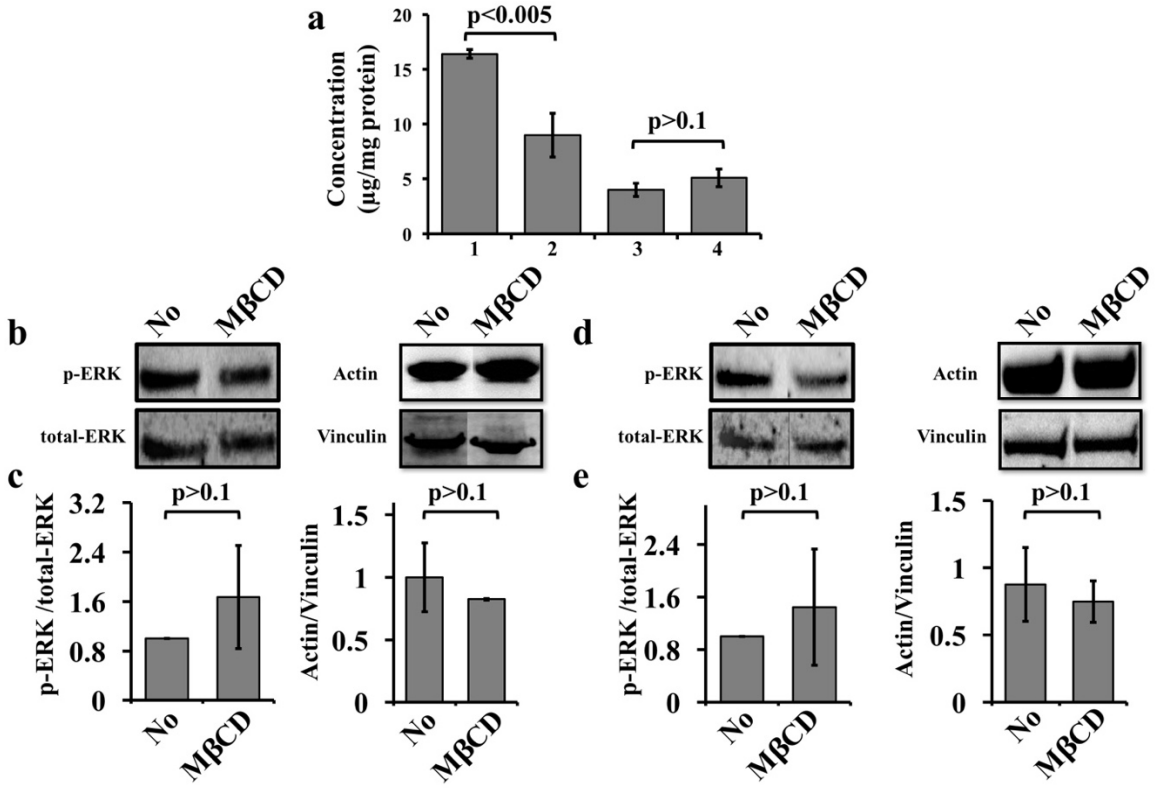


**Figure 4.6.** (a) Cholesterol quantification with Amplex® Red assay. Average (n = 2) free cholesterol (1 and 2) and cholesterol ester (3 and 4) concentration as measured from GM07373-RAGE cell lysate at native cellular conditions (1 and 3) and 5 mM methyl-β-cyclodextrin (MβCD) treated (2 and 4). Effect of MβCD treatment on (b, c) GM07373-RAGE cells and (d, e) GM07373 cells. (b, d) Fluorescence image of the PVDF membrane probed with anti-p-ERK, anti-total-ERK, anti-actin or anti-vinculin antibody. (c, e) Average (n=4) fluorescence intensities of the 42 kDa band of p-ERK divided by the 42 kDa total-ERK band (left); Average (n=2) fluorescence intensities of the actin band divided by the vinculin band (right). Error bars represent one standard deviation.

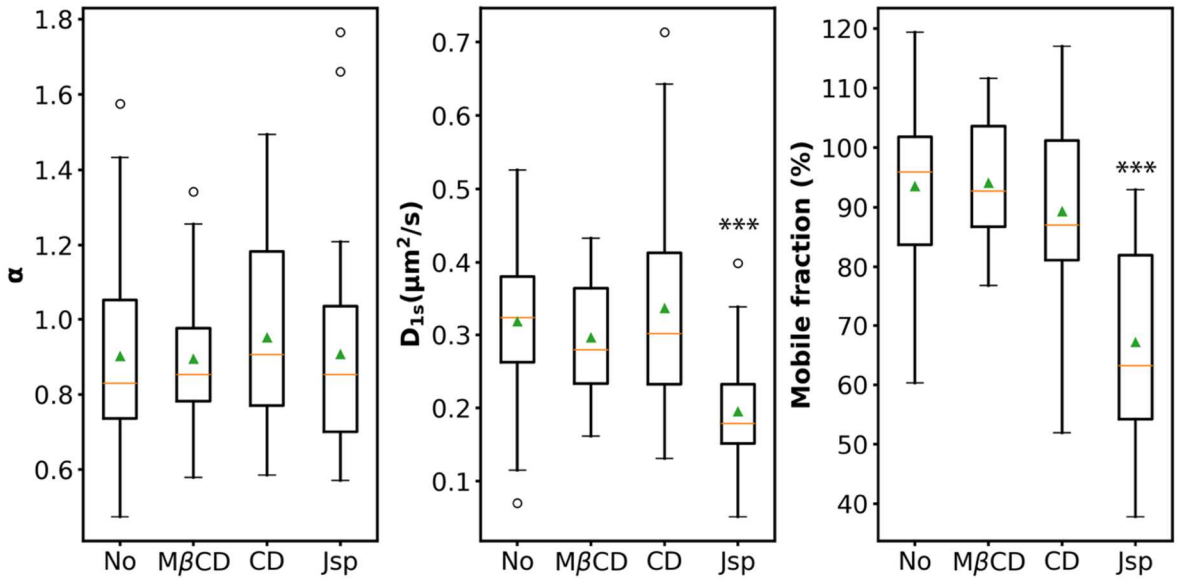


**Figure 4.7.** Box-and-whisker plots (n = 24 to 53) of RAGE-mRFP diffusion parameters in the GM07373 cell membrane obtained by FRAP after no treatment (No), 5 mM methyl-β-cyclodextrin (MβCD) treatment, 10 μM cytochalasin D (CD) treatment, or 3 μM Jasplakinolide (Jsp) treatment. The median and mean are represented as a horizontal line and triangle, respectively. The box limits are 50% (25–75%), the whiskers indicates 1.5 times the interquartile range, and the outliers are shown as open circles. *** indicates a statistically different from no treatment at the $p<0.001$ level.

## 4.7 Supporting Information

### Plasmids and transfection

Full-length human RAGE coding pcDNA3 vector (pcDNA3.RAGE) was a generous gift from Prof. Ann Marie Schmidt (New York School of Medicine, [1]. pcDNA3.mRFP plasmid was purchased from Addgene (#13032, Cambridge, MA). All oligonucleotides were obtained from Integrated DNA Technologies (Coralville, IA). To generate mRFP fused RAGE (pcDNA3.RAGE-mRFP), the RAGE sequence of pcDNA3.RAGE was amplified by polymerase chain reaction (PCR) using 5'-CCGGAATTCATGGCAGCCGGAACAGCAGTT-3' and 5'-CCGCTCGAGAGGCCCTCCAGTACTACTCTC-3' primers. The amplified RAGE region was sub-cloned into EcoRI/XhoI restriction sites of the pcDNA3.mRFP vector. The DNA sequence coding for human influenza hemagglutinin (HA) tag (YPYDVPDYA) was inserted in the N-terminal of RAGE and RAGE-mRFP plasmids using the following oligonucleotides 5'-TACCCGTACGACGTGCCGGACTACGCCATCACAGCCCGGATTGGC-3' and 5'-GGCG- TAGTCCGGCACGTCGTAGTTTTGAGCACCTACTACTGCCC-3' to generate pcDNA3.HA-RAGE or pcDNA3.HA-RAGE-mRFP plasmids. The recombinant plasmids were first transformed into DH5α *E. Coli* cells and transformed cells were selected on Luria broth agar (US biological, Salem, MA) plates containing 50 µg/mL Carbenicillin (Sigma-Aldrich, St. Louis, MO). GM07373 cells were transfected with purified recombinant plasmids obtained from DH5α cells using Lipofectamine 2000 using the manufacturer's instructions (Life Technology). Transfected GM07373 cells were selected using Geneticine sulfate (Santa Cruz Biotechnology, Inc., Santa Cruz, CA) in the complete growth medium.

**Immunoprecipitation and LC-MS/MS analysis of RAGE and RAGE-mRFP**

RAGE and RAGE-mRFP were purified using an N-terminal HA tag. Cell lysates from HA-RAGE or HA-RAGE-mRFP expressing GM07373 cells were incubated overnight at 4 ºC with anti-HA antibody conjugated agarose beads (Thermo Scientific). Agarose beads were washed with phosphate buffered saline (PBS) five times to remove the non-specifically bound components from the crude cell lysate. Bound HA-RAGE or HA-RAGE-mRFP was eluted by incubating the beads at 70 ºC for 10 minutes with sodium dodecyl sulfate sample buffer (5% SDS, 5% Glycerol, 125 mM Tris-HCl (pH=6.8) and 0.01% Bromophenol Blue) with a reducing agent (5 mM Dithiothreitol). After centrifuging the beads (14,000 rpm, 3 minutes), supernatant from the elution step was directly added to a pre-cast protein gel for separation by electrophoresis. Coomassie stained protein bands corresponding to HA-RAGE or HA-RAGE-mRFP were excised from the gel and were digested with trypsin on an automated ProGest (Digilab, Marlborough, MA) protein digestion station. Digested fragments were loaded onto the Q-Exactive tandem mass spectrometer (Thermo Scientific) for LC-MS/MS analysis. The measured peptide fragments were searched with both SEQUEST and Mascot to identify sequence matches.

**Figures and tables for supporting information for Chapter 2**

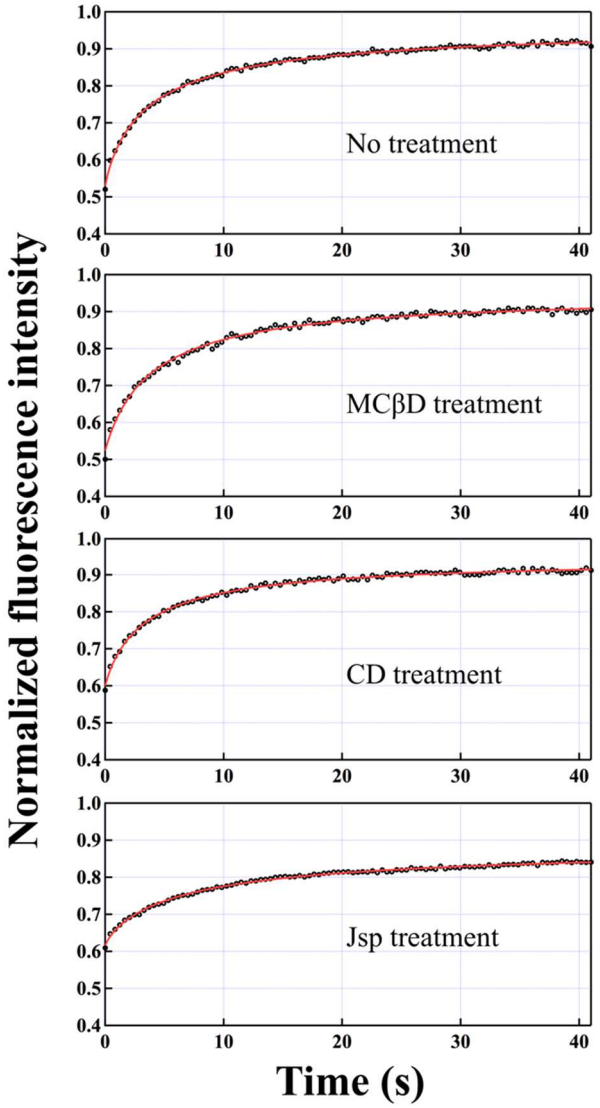


**Figure S4.1.** Average (n = 24 to 53) fluorescence recovery after photobleaching curves from RAGE-mRFP diffusion measurements in GM07373-RAGE-mRFP cells. The data are fit to equation 2 as outlined in the Materials and Methods (red line). CD: cytochalasin D; MβCD: Methyl-β-cyclodextrin; Jsp: Jasplakinolide.

**References for supporting information for Chapter 4**

[1] M. Neeper, A.M. Schmidt, J. Brett, S.D. Yan, F. Wang, Y.C. Pan, K. Elliston, D. Stern, A. Shaw, Cloning and expression of a cell surface receptor for advanced glycosylation end products of proteins, *J Biol Chem*, 267 (1992) 14998-15004.

# CHAPTER 5. GENRAL CONCLUSIONS AND FUTURE WORK

A major goal of the work presented in this dissertation was to study the receptor for advanced glycation endproducts (RAGE) diffusion and clustering using different fluorescence imaging techniques. The lateral diffusion and clustering properties of receptors play a role in how receptors interact with extracellular ligands, intracellular proteins, other intracellular components. More importantly, these properties affect how receptors function.

In Chapter 2, it was shown that Diaphanous 1 (Diaph1) affected the RAGE clusters and RAGE's diffusion measured by stochastic optical reconstruction microscopy and single particle tracking in HEK293 cells, respectively. A reduction in the expression of Diaph1 or a mutation in the interaction site to RAGE reduced the size and number of RAGE clusters. Altering a known site of interaction between RAGE and Diaph1 led to a decreased RAGE diffusion in both the fast and slow populations. In contrast, reducing the expression of Diaph1 increased RAGE diffusion in a manner that was proposed to involve actin polymerization.

In Chapter 3, the extracellular ligands of RAGE binding affinity were observed to affect RAGE diffusion and signal transduction via single particle tracking. The ligand methylglyoxal modified-bovine serum albumin (MGO-BSA) was prepared and characterized. MGO-BSA binding to a soluble variant of RAGE was dependent on the percentage of primary amine modification and the net negative surface charge. Although MGO-BSA ligand binding affinity affected RAGE lateral diffusion, there was no direct correlation between MGO-BSA ligand binding affinity and RAGE diffusion. However, the ligand stimulated RAGE diffusion was dependent on the level of cholesterol in cells.

In Chapter 4, RAGE lateral diffusion was probed in native, cholesterol depleted and cytoskeleton altered cellular conditions by fluorescence recovery after photobleaching (FRAP) in GM07373 endothelial cells. It was shown that the RAGE mobile fraction, diffusion coefficient and phosphorylation of extracellular signal-regulated kinase (p-ERK) decreased when depolymerization of the actin cytoskeleton was inhibited with the small molecule Jasplakinolide. However, there is no statistically significant change in diffusion properties of RAGE or p-ERK after cholesterol depletion.

Future work will be required to understand the molecular mechanism of RAGE diffusion and clustering upon chemically-defined RAGE ligands. This chemically-defined ligands conjugated with appropriated fluorophores could be applied to SPT or STORM. The effect of other receptors on RAGE diffusion could be measured. For example, there is recently emerging evidence that Toll-like 4 receptors (TLR4) and RAGE exhibit receptor "cross talk" through binding a subset of shared ligands and also through shared signal transduction pathways, which involve several kinases that phosphorylate their respective protein substrates. The interaction between RAGE and TLR4 could be measured by fluorescence resonance energy transfer. A dual-color SPT or a dual-color STORM should be developed for determining nanoscale organization and diffusion of RAGE and TLR4.